

Wide Speed Range Operation of Concentrated Winding Interior Permanent Magnet Synchronous
Machines

by

Mohammad Sedigh Toulabi

A thesis submitted in partial fulfillment of the requirements for the degree of

Doctor of Philosophy

In

Energy Systems

Department of Electrical and Computer Engineering
University of Alberta

© Mohammad Sedigh Toulabi, 2016

Abstract

The design, simulation and experimental evaluation of an Interior Permanent Magnet Synchronous Motor (IPMSM) are investigated. The motor is designed to be capable of operation from either a concentrated single inverter supply or in an “Open-Winding” configuration using two converters.

In order to investigate the relationships between geometry, circuit parameters and desirable performance, a parametric design of experiments study based on the changes to the motor geometry is conducted. Two Dimensional Finite Element Method (2D-FEM) is used to simulate the impact of geometric design changes on motor operation.

In order to increase the voltage applied to each phase of the machine and extend the operating region, an IPMSM is modeled in an open winding structure fed by two isolated Voltage Source Converters using a dual inverter drive structure. Each converter is controlled to supply only either real power or reactive power.

The motor performance is experimentally evaluated in single inverter and dual inverter drives. With a single inverter drive, a wide speed range (6.66 time base speed) is observed, with peak efficiency above 90%, both of which are close to the expectations from simulation analysis. To ensure a reliable performance for the open winding IPMSM using a dual inverter drive, a new control technique is proposed and verified.

Two significant contributions are made. The first is to evaluate the motor geometry changes and their impact on the IPMSM’s performance, especially for wide speed range open winding applications. The second is to develop a new control method for the dual inverter open winding IPMSM in order to extend the operating region, improve the power capability and efficiency.

To

My Wife & My Parents

Shahrzad & Heshmat and Fatemeh

Acknowledgments

It is with immense gratitude that I acknowledge the support and guidance of my supervisor, Prof. Andy Knight who taught me how to think and solve a problem from beginning to end. I will never forget his invaluable supervision and constructive comments in all the steps of my research.

I also wish to express my thanks to Prof. John Salmon for financially supporting me in the first three years of my PhD program, and without whose assistance I would never have reached this point of educational progress.

I would like to extend a special thank you to Prof. Nigel Schofield from McMaster University and other examining committee members including Prof. Venkata Dinavahi, Dr. Jeremy Sit and Dr. Ashwin Iyer for taking the time to review this thesis.

The machine shop personnel, two experienced technicians; Mr. Garwin Hancock, Mr. Rob Thomson, and my friend Mr. Ronald Rebeiro for their help in preparing my test rig during my visit to the University of Calgary.

The University of Alberta and the University of Calgary for giving me the invaluable opportunity to use the necessary facilities for conducting my research.

Last but not least, my deepest appreciation goes to my family to my beloved wife, Shahrzad, for her patience during my difficult days. Undoubtedly, without her support and encouragement, finishing my PhD program could not have been possible. And to my dear parents, Heshmat and Fatemeh who devoted their entire lives , their time and their youth to help me from my first day at elementary school to the end of my PhD.

Contents

CHAPTER 1

INTRODUCTION	1
--------------------	---

CHAPTER 2

THEORY OF OPERATION AND CONTROL	4
2.1 Field Weakening (FW) Operation	7
2.2 Concentrated and Distributed Windings	12
2.3 Losses	15
2.4 Voltage Source Converter fed PMSM	17
2.5 Open Winding AC Machines	18
2.6 Summary	21

CHAPTER 3

ELECTRIC MACHINES ANALYSIS AND DESIGN	22
3.1 Initial Machine Specifications	22
3.1.1 PMSM Slot-Pole Combination Selection	22
3.1.1.1 Winding Factor Assessment	23
3.1.1.2 MMF Assessment in PMSMS	25
3.1.2 Initial Dimensions for the Investigated IPMSM	27
3.2 Impact of Rotor Geometry Changes on Performance of the IPMSM to Find the Initial Design	31
3.2.1 Impact of γ Changes with no Constraint on the Magnet's Flux Density	32
3.2.2 Impact of Clearance Changes	33
3.2.3 Impact of Magnet Pitch Changes	36

3.2.4	Initial Design Summary	37
3.3	Design Refinement	38
3.4	Final Design	42
3.5	Loss and Efficiency Analysis	45
3.5.1	Harmonic Iron Losses	48
3.6	Summary	50
CHAPTER 4		
DUAL INVERTER ANALYSIS		52
4.1	Drive Simulation	58
4.2	Finite Element Analysis of Open Winding Operation	63
4.2.1	Open Winding IPMSM'S Loss Analysis and Efficiency Assessment	66
4.3	Summary	69
CHAPTER 5		
EXPERIMENTAL VERIFICATION		72
5.1	Machine Construction	72
5.2	Test Rig	76
5.3	Single Inverter Testing	79
5.3.1	Back-EMF Waveform	79
5.3.2	Inductance Evaluation	80
5.3.3	Current Profiles for the Tested Machine	82
5.3.4	Field Weakening and Maximum Speed of the Tested Machine	83
5.3.5	Losses and Efficiency	85
5.4	Dual Inverter Test Rig	89
5.5	New Floating Bridge Control Technique	91

5.5.1	Experimental Investigations	98	
5.6	Summary	104	
CHAPTER 6			
CONCLUSIONS			106
6.1	Conclusions and Contributions	106	
6.2	Suggestions	108	
REFERENCES			110

Figures

Fig 2.1	PM Electric machines classification	4
Fig 2.2	Physical structures for a) SPMSM b) IPMSM	5
Fig 2.3	12 slot-8 pole V-shaped magnet IPMSM	5
Fig 2.4	Motor d- and q-axes and MMF vector	6
Fig 2.5	PMSM's a) Voltage vector diagram in d-q frame b) Current ellipses and current circle	8
Fig 2.6	Curves showing Field Weakening (FW) region, a) Power versus speed and b) Torque versus speed	11
Fig 2.7	Typical stator winding configurations (four pole), (a) Twenty-four slot, overlapping. (b) Twelve slot, overlapping. (c) Six slot, nonoverlapping, all teeth wound. (d) Six slot, nonoverlapping, alternate teeth wound	13
Fig 2.8	Diagram for a Voltage Source Converter (VSC) fed IPMSM	17
Fig 2.9	The open winding AC machine using a dual inverter drive structure	18
Fig 3.1	Winding factor and MMF mechanical harmonic spectrums for a, b) 9 slot 6 pole, c, d) 12 slot 8 pole, e, f) 12 slot 10 pole double layer concentrated winding PMSMs	26
Fig 3.2	Different parts of the PMSM for machine design using analytical assessment	28
Fig 3.3	A piece of a) Rotor and b) Stator of a V-shaped magnet IPMSM	30
Fig 3.4	a) Inductance evaluation, b) Back-EMF voltages, c) Back-EMF THDs, d) Cogging torques for five different machines with different γ and without any constraint on the utilized magnets (900 rpm)	32
Fig 3.5	a) Back-EMF voltages, b) Back-EMF THDs, c) Cogging torques, for three different machines with different γ and minimum clearance (900 rpm)	34
Fig 3.6	a) Back-EMF voltages, b) Back-EMF THDs, c) Cogging torques, for three different machines with different γ and wide clearance (900 rpm)	34
Fig 3.7	L_d and L_q evaluation using the wide and minimum clearances between two adjacent magnets in three different V-shaped magnet IPMSMs	35
Fig 3.8	a) Back-EMF voltages, b) Back-EMF THDs, c) Cogging torques, for three different machines with different γ and 85% magnet pitches (900 rpm)	36
Fig 3.9	a) Back-EMF voltages, b) Back-EMF THDs, c) Cogging torques, for three different machines with different γ and 100% magnet pitches (900 rpm)	36
Fig 3.10	L_d and L_q variations in 100% and 85% magnet pitches for three different γ IPMSMs	37
Fig 3.11	The initial design of the IPMSM	38

Fig 3.12	The physical structures and flux density plots in presence of different changes applied on the initial design, a) Case 1, b) Case 2, c) Case 3, d) Case 4, e) Case 5	39
Fig 3.13	B-H curve versus temperature changes for NEOMAX-52	40
Fig 3.14	B-H curve versus temperature changes for NEOMAX-35EH	41
Fig 3.15	Inductance as the function of γ when there is a specific constraint on the utilized magnet flux density	41
Fig 3.16	75° γ IPMSM using NEOMAX-35EH, case 6	42
Fig 3.17	Comparison for the six cases a) Maximum speed, b) L_d , c) Saliency, d) Back-EMF THD, e) Cogging Torque	43
Fig 3.18	The final model a) Back-EMF waveform in 900 rpm, b) Back-EMF harmonic spectrum, c) L_d , and d) L_q	44
Fig 3.19	a) B-H curve, and b) Loss density variations for M19 lamination	46
Fig 3.20	Copper loss, iron loss, eddy current loss and hysteresis loss evaluation, for the designed IPMSM using 29 gauge M19 lamination	47
Fig 3.21	a) Current profile b) Magnet loss c) Power-Torque versus speed profile taking into account the mechanical loss including friction and windage (F&W), for the designed IPMSM using M19 core	47
Fig 3.22	Efficiency analysis for the designed IPMSM	48
Fig 3.23	Designed IPMSM's a) Air gap flux density, b) Harmonic analysis for the air gap flux density in 900 rpm	49
Fig 3.24	Harmonic iron loss for the designed IPMSM, a) 1 st harmonic, b) 3 rd harmonic, c) 5 th harmonic, d) 7 th harmonic, e) 9 th harmonic	49
Fig 3.25	Percentage of total iron loss for each harmonic in a) Base speed (900 rpm), b) Maximum speed (6300 rpm)	50
Fig 4.1	a) Conceptual vector diagram and b) Circuitry of the dual inverter scheme	53
Fig 4.2	Dual inverter drive conceptual voltage vector diagram, a) In 1.1 times machine's rated voltage (lagging power factor), b) In 1.2 times machine's rated voltage (leading power factor), c) In 1.41 times machine's rated voltage (leading power factor)	54
Fig 4.3	Dual inverter open winding PMSM controller block diagram for the maximum speed to 1.41 times maximum speed region, rated power is fulfilled	57
Fig 4.4	The open winding SPMSM fed by two VSCs in Simulink space	58
Fig 4.5	The open winding SPMSM modeled in Simulink	59
Fig 4.6	a) Capacitor voltage control, b) Speed control, c) Modulating signals assessment in 150 rad/s	60

Fig 4.7	a) Capacitor voltage control, b) Speed control, c) Modulating signals assessment in 250 rad/s	61
Fig 4.8	a) Capacitor voltage control, b) Speed control, c) Modulating signals assessment in 425 rad/s	62
Fig 4.9	Torque-Power versus speed profile showing different regions of operation for the comparison purposes	63
Fig 4.10	The dual inverter open winding IPMSM model in JMAG-Designer	64
Fig 4.11	Peak current changes in wide range of speeds	64
Fig 4.12	The Floating Bridge (FB) voltage components in wide range of speeds	65
Fig 4.13	Power-torque versus speed profile for showing the contribution of the dual inverter drive structure	66
Fig 4.14	Copper loss, and iron loss analysis in wide range of speeds using single and dual inverter drives	67
Fig 4.15	Efficiency analysis for the designed IPMSM in the wide range speeds	67
Fig 4.16	Iron loss harmonic analysis in single and dual inverter drive structures for the designed IPMSM in a) Fundamental harmonic, b) 3 rd harmonic, c) 5 th harmonic, d) 7 th harmonic, e) 9 th harmonic	68
Fig 4.17	The contribution of each harmonic to the total iron loss of machine in 8800 rpm	69
Fig 5.1	The stator lamination and its different dimensions in Auto-CAD	72
Fig 5.2	a) Rotor, b) Magnet dimensions	73
Fig 5.3	Actual laminations for a) Rotor, b) Stator	74
Fig 5.4	a) Welded stator stack, b) The rotor fixture	74
Fig 5.5	NEOMAX-35EH used in the built machine structure	74
Fig 5.6	a) Winding arrangement for the 12 slot 8 pole IPMSM, b) Coils arrangement for phase (A)	75
Fig 5.7	The actual wound stator	75
Fig 5.8	The built machine	76
Fig 5.9	a) Schematic side view of machine's frame and housing, b) The built machine ready for the tests	76
Fig 5.10	The conventional PMSM drive with the control structure	77
Fig 5.11	The schematic view of the system for the single inverter drive tests	77
Fig 5.12	a) Semikron inverter for the load side control, b) Semiteach inverter for the motor side control	78
Fig 5.13	Complete test bench in the lab	78
Fig 5.14	Close-up of the motor stand	79

Fig 5.15	Back-EMF voltage verification in open circuit analysis, a) Simulation, b) Experiment in 900 rpm	79
Fig 5.16	Inductance measurement circuit for AC standstill approach	80
Fig 5.17	d- and q-axes static inductances using AC stand still method (Experiment)	81
Fig 5.18	a) L_d and b) L_q as the function of current magnitude and angle for the built machine, (Simulation)	81
Fig 5.19	a) Three phase current in no load, b) Three phase currents in 80% load, c) d- and q-axis currents in 80% load, (Experiment, 900 rpm)	83
Fig 5.20	a) Torque versus speed capability of the machine in simulation and experiment, b) d- and q-axis current profiles in FW region (Experiment)	84
Fig 5.21	Loss evaluation for the final model in 1kW power (FEM Simulation)	85
Fig 5.22	Efficiency assessment of the finally designed IPMSM in wide range speeds and loads using JMAG-RT (Simulation)	86
Fig 5.23	Circuit configuration to measure the input power of the machine	87
Fig 5.24	Copper loss analysis (Experiment) in the maximum possible power (it is assumed that the resistance is not the function of frequency changes)	87
Fig 5.25	Summation of friction, windage and iron losses (Experiment)	87
Fig 5.26	Efficiency assessment of the built machine in wide range of speeds and load levels (Experiment)	88
Fig 5.27	Dual inverter open winding IPMSM	89
Fig 5.28	The Main Bridge (MB), and Floating Bridge (FB) inputs in the built machine	89
Fig 5.29	The schematic view of the system in dual inverter drive structure	90
Fig 5.30	Complete test bench in lab for the dual inverter drive experiments	90
Fig 5.31	Inputs and output of capacitor voltage PI controller	92
Fig 5.32	Block diagram used in experimental analysis for the dual inverter drive structure	94
Fig 5.33	a) Capacitor voltage control, and the speed control in b) 900 rpm, c) 6300 rpm, d) 8100 rpm	95
Fig 5.34	Simulated control signals, a) Phase current and the MB modulating signal in rated power and 900 rpm, the MB and FB modulating signals in the rated power and speeds of b) 900 rpm, c) 6300 rpm, d) 8100 rpm	96
Fig 5.35	Simulated control signals, a) Phase current and modulating signal of the MB, b) Modulating signals for the MB and FB, in base speed and 1.3 times rated power	97
Fig 5.36	The MB voltage, FB voltage, phase current and capacitor voltage in 900 rpm	98

Fig 5.37	The MB Line to Line voltage (V_{ab}), and phase current in maximum possible power for a) 4500 rpm, b) 5400 rpm, c) 6000 rpm, the fundamental component of MB voltage leads current by 30 degrees	99
Fig 5.38	a) Developed torque for single and dual inverter drives, b) Output power for single and dual inverter drives, c) d- and q-axis currents for the dual inverter drive	100
Fig 5.39	The circuit for the input power calculation from the MB side of view	101
Fig 5.40	The input power signal from the MB side in a) 4500 rpm, b) 5400 rpm, and c) 6000 rpm	102
Fig 5.41	Efficiency assessment of the built machine in wide range of speeds and load levels from the MB side of view (Experiment)	103

Tables

Table 3.1	Detailed winding factor (k_w) and MMF assessment for different slot pole combinations	27
Table 3.2	Some of the initially defined parameters for obtaining the machine's dimensions	28
Table 3.3	PMSM's general specifications using the analytical assessment	29
Table 3.4	The total volume of the utilized magnets in different γ	42
Table 4.1	Specifications of BSM90N-275AA PMSM and the utilized drive	58
Table 5.1	Machine specifications for SIMULINK modeling and control	95
Table 5.2	Detailed comparison for the developed torques using single and dual inverter drives	101

Nomenclature

A_{rot}	Air gap surface area	(m ²)
$B_{air-gap}$	Air gap flux density	(T)
B_{max}	Maximum flux density	(T)
B_n	n_{th} harmonic of air-gap flux density	(T)
B_r	Remnant flux density	(T)
B_s	Stator flux density	(T)
B_t	Tooth flux density	(T)
B_y	Back Iron flux density	(T)
$CPSR$	Constant power speed region	
D_i	Stator inner diameter	(m)
D_o	Stator outer diameter	(m)
E_a	Phase (A) Back-EMF	(V)
FB	Floating Bridge	
f_e	Electrical frequency	(Hz)
GCD	Greatest common divisor	
H_c	Coercivity	(A/m)
h	Thickness	(m)
I_a	Phase (A) current	(A)
I_{ch}	Characteristic current	(A)
i_d	Stator d-axis current	(A)
i_{dF}	Filtered d-axis current	(A)
I_{max}	Machine's maximum possible current	(A)
$I_{ph}(i, I)$	Phase current (rms)	(A)
i_q	Stator q-axis current	(A)
i_{qF}	Filtered q-axis current	(A)
K	Back-EMF constant	
K_d	Distribution factor	
k_e	Eddy current loss constant	
k_h	Hysteresis loss constant	
k_i	Integral coefficient in PI controller	

K_p	Pitch factor	
k_p	Proportional coefficient in PI controller	
K_{skew}	Skewing factor	
k_w	Winding factor	
k_{w1}	Fundamental component of winding factor	
L	Stack length	(m)
L_a	Phase (A) inductance	(H)
LCM	Lowest common multiple	
L_d	Machine's d-axis inductance	(H)
L_q	Machine's q-axis inductance	(H)
L_s	Synchronous inductance	(H)
l_t	Tooth length	(m)
l_y	Back Iron depth	(m)
m	Number of phases	
m_a	Modulation index using SVM	
MB	Main Bridge	
MMF	Magnetomotive force	(AT)
M^+	Forward MMF component	
M^-	Backward MMF component	
N_{phase}	Phase turn number	
n_c	Number of coils	
n_y	Electrical displacement factor for phase shifts	(rad)
P	Real Power	(W)
p	Poles	
P_{Copper}	Copper loss	(W)
P_{Demand}	Required real power of machine	(W)
$P_{Demand-FB}$	Required real power to charge capacitor	(W)
$P_{Eddy-current}$	Eddy current loss	(W)
$P_{Friction\&Windage}$	Friction and windage loss	(W)
P_{Iron}	Iron loss	(W)
P_{out}	Output power	(W)
Q	Reactive power	(Var)

Q_s	Slots	
R_a	Phase (A) resistance	(Ω)
Rel	Reluctance	(AT/Wb)
R_g	Air gap reluctance	(AT/Wb)
R_s	Stator phase resistance	(Ω)
$SPP(q)$	Slot per pole per phase	
t	Time	(s)
T_{cog}	Cogging torque	(N.m)
T_e	Developed torque	(N.m)
THD	Total Harmonic Distortion	
T_{rel}	Reluctance torque	(N.m)
V_a	Phase (A) voltage	(V)
V_{ab}	Phase (A) and Phase (B) line to line voltage	(V)
V_{cap}	Capacitor voltage	(V)
$V_{cap-ref}$	Reference value of capacitor voltage	(V)
V_{cb}	Phase (C) and Phase (B) line to line voltage	(V)
V_{DC}	DC link voltage of a VSC	(V)
v_{d1}	Main Bridge d-axis voltage	(V)
v_{d2}	Floating Bridge d-axis voltage	(V)
V_{FB}	Floating Bridge voltage	(V)
V_m	Motor terminal voltage	(V)
V_{max}	Machine's maximum possible voltage	(V)
V_{MB}	Main Bridge voltage	(V)
$v_{md} (v_d)$	Motor d-axis voltage	(V)
$v_{mq} (v_q)$	Motor q-axis voltage	(V)
$V_{Phase-Peak}$	Peak of phase voltage	(V)
v_{q1}	Main Bridge q-axis voltage	(V)
v_{q2}	Floating Bridge q-axis voltage	(V)
X_s	Synchronous reactance	(Ω)
γ	The angle between two magnets in each pole	(Degree)
η	Efficiency	
η_{st}	Steinmetz constant	

η_V	Angle from voltage vector graph	(rad)
θ_r	Rotor position	(rad)
λ_{ds}	Stator d-axis flux linkage	(Wb)
λ_{pm}	Permanent magnet flux linkage	(Wb)
λ_{qs}	Stator q-axis flux linkage	(Wb)
ξ	Speed of MMF vector rotation	(rad/s)
σ	Conductivity	(S/m)
τ_{cc}	Coil pitch of the c^{th} coil	
τ_{pole}	Pole pitch	(rad)
τ_{slot}	Slot pitch	(rad)
φ	Flux	(Wb)
φ_g	Air gap flux	(Wb)
ω_e	Electrical frequency	(rad/s)

Chapter 1

INTRODUCTION

Efficient performance and a wide speed range of an Interior Permanent Magnet Synchronous Machine (IPMSM) in constant power are desirable characteristics in applications such as Electric Vehicles (EVs) and machine tools. In this regard, desirable operational characteristics for this kind of machine should be obtained while limiting unwanted harmonics in the torque and terminal voltage. These characteristics are all influenced by the machine's geometry and its impact on circuit parameters. The relationship between geometry and performance is nonlinear and not well characterized. In many cases, designers must rely on numerical optimization to fully understanding the relationship between design choices and performance compromises. Relating geometry to the circuit parameter, an efficient PMSM with wide speed range may be achieved by effectively tuning the physical design variables while taking into account the cost of manufacturing. In order to fulfill this aim the parametric design of experiments procedure is followed. In this regard, some of the main physical variables of IPMSM are manually adjusted to introduce an initial design with high potential to be used in wide speed range applications, and then the design refinement steps are conducted to define a final IPMSM model.

One of the limiting factors on the speed range and Constant Power Speed Region (CPSR) of an IPMSM is the available terminal voltage. One option to increase the terminal voltage from a fixed supply is to use an open winding machine. In a three phase open winding IPMSM, there is no neutral point, and six separate leads of the machine are connected to two Voltage Source Converters (VSCs) [1]. In this work, one VSC is connected to a single DC power source, called the Main Bridge (MB), whilst the other, called the Floating Bridge (FB), uses a floating capacitor DC voltage source. This approach assists in enabling the machine to operate from a limited DC voltage; for example it may allow the motor voltage to be increased without increasing battery voltage in an EV. Compared to the delta connected machine, there are two degrees of freedom to tune the applied voltage on the machine's phases in an open winding scheme. However, a suitable and reliable controller is required to control the two separate voltage sources feeding the inputs of the open winding machine. Such as control scheme is one of the contributions of this Thesis.

To understand and predict the performance of an IPMSM, basic definitions and equations are described and interpreted in Chapter 2. Design of an IPMSM with large d-axis inductance is discussed and the dual inverter drive structure for extended speed range is introduced.

The steps taken to find a design for an IPMSM with wide range speed capability and promising efficiency are described in Chapter 3. Cogging torque, Back-EMF harmonic analysis, and maximum speed assessment for different IPMSMs are evaluated in the presence of various physical changes on the rotor structure. Magnet pitch, clearance between magnet, and angle between magnets (γ) are manually tuned, and the performance of the IPMSM is evaluated in each geometry change to introduce an initial model. Additional geometry changes including flux barrier shape, slot opening and air-gap are applied to the initial model in order to propose a final IPMSM design. The geometry changes aim to adjust the d- and q-axis magnetization for inductance assessment and to reduce the harmonic content of the air-gap flux density. Lower loss density laminations and lower magnetic flux density (B_r) magnets are used for the final model. The main contribution of Chapter 3 is to conduct a step-by-step parametric design of experiments procedure to finalize an IPMSM model. In first steps, different changes are applied to the rotor geometry and their impacts on the machine's performance are evaluated. In next steps, the further physical and material modifications are applied to the initially designed model to finalize an IPMSM model with wide speed range performance potential.

Chapter 4 discusses the dual inverter drive structure and how the PMSM can be used and controlled in an open winding configuration as part of the drive. This chapter studies the vector diagram as the basic criterion for control approach assessment in the dual inverter drive structure. An initial control approach is introduced and a series of simulation results carried out by Matlab/Simulink are included to verify the practicality of the control approach. The FB voltage is set to be perpendicular to the current by the controller and the MB and FB voltages are simultaneously applied to the phases of machine to extend the operating region of the machine compared to the single inverter drive. The magnitude of the MB and FB voltages are the function of the operating point and the tuned i_d current. The final IPMSM design introduced in Chapter 3 is simulated and investigated in an open winding configuration using a 2D-FEM simulation. It is shown that the newly designed machine can support a wider range speed than the single inverter drive. Loss analysis and efficiency assessment of the final design are carried out to give broader information about the machine in the dual inverter drive. 41% operating region extension

including the maximum speed, and the efficiency above 87% for the wide range of speeds are expected by simulation investigations in open winding analysis presented in Chapter 4.

The experimental performance evaluations for the newly designed IPMSM using single and dual inverter drives are presented in Chapter 5. The prototype design is built and experimentally investigated in both single and dual inverter drive structures. The test facility is described together with some discrepancies between the finally simulated design and the actual built machine. A new control technique is proposed and simulated for the open winding IPMSM using a dual inverter drive. A 10-15% output power capability improvement is also experimentally verified. The exact output power capability improvement in each operating point and speed is clearly included in this Chapter. The main contribution of this chapter is to introduce the actual built machine and its different parts and testing it in both single and dual inverter drive structures, as well as proposing a new Floating Bridge (FB) control technique for the dual inverter open winding IPMSMs. Construction of the machine, preparation of the test rig and implementation of the different controller schemes using the TI-28335 based Digital Signal Controller (DSC) are carried out by the author. The utilized converters are not specifically designed and sized for this research and are bought for the experimental analysis.

The contribution of the Thesis may be improved if additional considerations beyond the scope of this work are implemented. These considerations may include better quality manufacturing, using lower loss components in experimental analysis, and the use of converters designed specifically for operation with this machine. The concluding remarks of the study and the most important suggestions for future work to improve the Thesis contributions are presented in Chapter 6.

Chapter 2

THEORY OF OPERATION AND CONTROL

The basic equations and concepts regarding the PMSMs performance are included in this chapter. It is shown that the circuit parameters of IPMSM including the inductances are affected by the machine geometry changes. In addition, maximizing the inductance and applying extended voltage on the machine's phases are presented as two main alternatives to introduce an IPMSM with wide speed range characteristic. A compromise should exist between the different circuit parameters of machine for maximizing the speed range and the torque capability.

Permanent Magnet (PM) machines can be classified into two main groups, depending on the supply voltage; AC and DC. A Permanent Magnet Synchronous Machine (PMSM) is a category of AC machine, typically with sinusoidal Back-EMF (Fig 2.1 [2]).

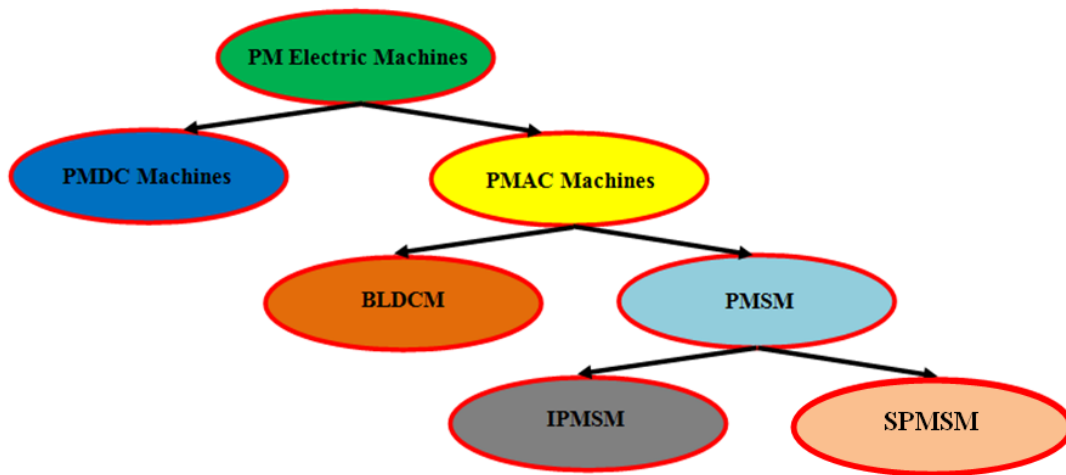


Fig 2.1 PM Electric machines classification [2]

PMSMs are classified, depending on the positioning of the magnets in the rotor of the machine. Magnets can be mounted on the rotor structure; surface mounted PMSMs (SPMSMs), or they can be implemented in the rotor; Interior PMSMs (IPMSMs), see Fig 2.2 which shows both introduced structures [3].

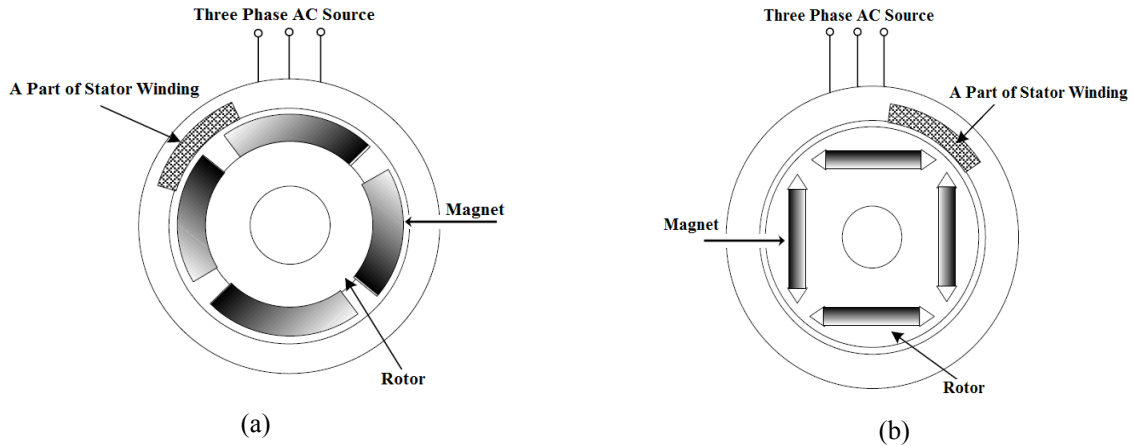


Fig 2.2 Physical structures for a) SPMSM b) IPMSM [3]

SPMSMs usually have a characteristic that the stator windings inductance is independent of the rotor position, or d-axis inductance (L_d) is equal to q-axis inductance (L_q), $L_d=L_q$ [4, 5]. The rotor of this machine has an iron core that may either be solid or made of punched laminations for simplicity in manufacturing [6]. On the other hand, the geometry of an IPMSM is such that the stator windings inductance is a function of the rotor position. As a result, IPMSMs are capable of providing reluctance torque in addition to the excitation (Magnetic) torque. In these types of the machines the d- and q-axis inductances are not same [7].

There are four basic rotor geometries for IPMSMs. These include single-piece/pole, rectangular shaped magnet design, segmented magnet design, V-shaped magnet design, and the multi-barrier design [8-10]. In this thesis, the V-shaped magnet IPMSM is considered for the performance evaluation procedure due to its high flux concentration. An 8-pole, 12-slot, V-shaped magnet IPMSM and some of its different parts are shown in Fig 2.3.

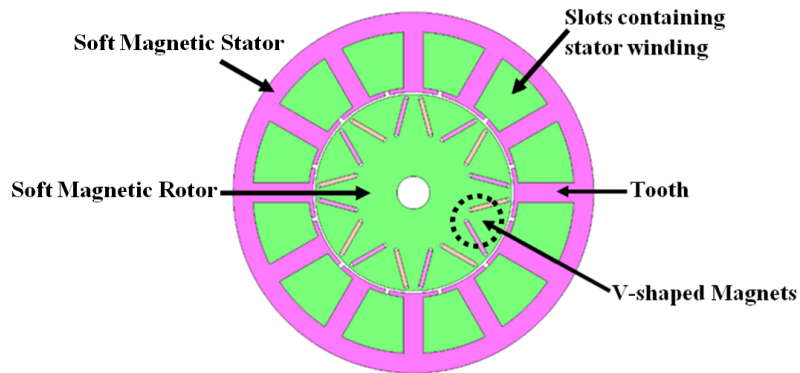


Fig 2.3 12 slot- 8 pole V-shaped magnet IPMSM

The PMSM's phase voltage equation is described in equation (2.1) [11-13]:

$$V_a = E_a + (R_a + j\omega_e L_s)I_a = E_a + (R_a + jX_s)I_a \quad (2.1)$$

Where Back-EMF (E_a) is the function of rotor permanent magnet flux (ϕ) and speed (ω_e) as follows:

$$|E_a| = K\phi\omega_e \quad (2.2)$$

A detailed model of the PM motor drive system is required for proper simulation of the system. The d- and q-axis model has been developed in the rotor reference frame as shown by Fig 2.4. At any time (t) the rotating rotor q-axis makes a mechanical angle with the fixed stator phase axis, and the rotating stator Magnetomotive Force (MMF) makes an angle (α) with the rotor d-axis. The stator MMF rotates at the same speed as that of the rotor [14].

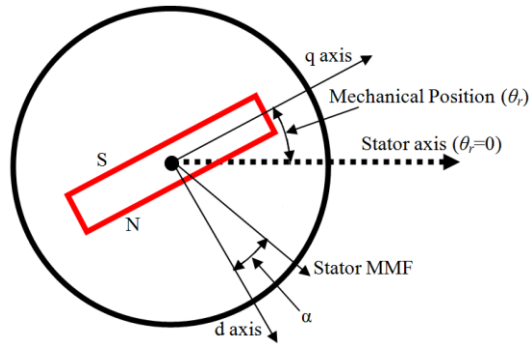


Fig 2.4 Motor d- and q-axes and MMF vector [14]

The MMF's simplified equation is as follows [15]:

$$MMF = B_s \cdot A_{rot} \cdot R_g \quad (2.3)$$

As the magnet flux and winding inductances are functions of the rotor position, it is usual to use the Park Transformation referring the current variables to the rotor reference frame, when analyzing PMSM performance. In the rotor reference frame and assuming no common mode voltages, the voltage equations in d- and q-axis frame are given by [16, 17]:

$$v_{mq} = R_s i_q + \omega_e \lambda_{ds} + \frac{d\lambda_{qs}}{dt} \quad (2.4)$$

$$v_{md} = R_s i_d - \omega_e \lambda_{qs} + \frac{d\lambda_{ds}}{dt} \quad (2.5)$$

The derivative operator ($\frac{d}{dt}$) in equations (2.4) and (2.5) becomes zero in the steady state analysis. The flux linkages in d- and q-axis frame are given by:

$$\lambda_{qs} = L_q i_q \quad (2.6)$$

$$\lambda_{ds} = L_d i_d + \lambda_{pm} \quad (2.7)$$

And the developed torque can be calculated as [18]:

$$T_e = \frac{3}{2} \left(\frac{p}{2} \right) (\lambda_{pm} i_q + (L_d - L_q) i_d i_q) \quad (2.8)$$

The developed torque has two components: magnetic torque and reluctance torque. In the case of SPMSM, $L_d=L_q$ and the reluctance component is zero. In the case of IPMSM, $L_d<L_q$ and the reluctance torque can increase the total torque, if i_d is negative. The torque given by equation (2.8) neglects the harmonic effects in the machine.

There is another type of torque in a PMSM which is unbeneficial and should always be minimized. This torque is called cogging torque and is described by (2.9) [19].

$$T_{cog} = \frac{1}{2} \varphi_g^2 \frac{dRel}{d\theta_r} \quad (2.9)$$

The cogging torque (T_{cog}) is the main result of the magnetic variation energy stored in the air gap. It is principally caused by the movement position between the rotation of the rotor's permanent magnets and the fixed stator slots.

An IPMSM is considered for the evaluation assessments for three principal reasons: First, with a buried magnet design, flux concentration can be achieved, which induces higher air gap flux density [20]. Secondly, due to the difference between L_d and L_q values in the IPMSM, reluctance torque can be employed to increase the developed torque of the machine [21]. Thirdly, there is more freedom to change the shape, orientation, and organization of the magnets in the IPMSM's rotor which gives the manufacturer more options for saliency, speed range, and CPSR improvement.

2.1 Field Weakening (FW) Operation

Under all operating conditions, the machine current and voltage should be kept below the maximum value (V_{max} and I_{max}). These limiting constraints in the d-q frame can be expressed by the following equations [22, 23]:

$$i_d^2 + i_q^2 \leq I_{max}^2 \quad (2.10)$$

$$v_{md}^2 + v_{mq}^2 \leq V_{max}^2 \quad (2.11)$$

where;

$$\vec{V}_m = v_{mq} + jv_{md} \quad (2.12)$$

The vector diagram of a PMSM's voltage in d-q frame using equations (2.4-2.7) is seen in Fig 2.5(a). According to this figure, when a limited voltage is applied to the PMSM's phases, one of the most important factors helping the machine to work in higher speeds is the term of $\omega_e L_d i_d$. The magnitude of V_m (vector) cannot exceed the radius of the base speed circle. In Fig. 2.5(a), this area (V_m) is indicated by the dotted semi-circle, and in Fig. 2.5(b), this limit is indicated by the current ellipses. Applying the negative d-axis current and having a machine with large L_d can be the useful methods for increasing the speed range of the machine. As the other alternative, supplying a bigger voltage (V_m) on the machine's phases (for example using higher rating converter) enhances the dotted semi-circle radius which makes it possible to extend the speed range. The current ellipses seen in Fig 2.5(b) are based on equation (2.13). It is worth noting that the dropped voltage across the resistance has been neglected to find equation (2.13)

$$i_q^2 + \left(\frac{\lambda_{pm} + L_d i_d}{L_q}\right)^2 \leq \frac{V_{max}^2}{L_q^2 \omega_e^2} \quad (2.13)$$

When the speed increases, the centre of the current ellipses converges to $(-\frac{\lambda_{pm}}{L_d}, 0)$. In order to regard both voltage and current limitations in the rated power, the machine should work in the shaded region (A) shown in Fig 2.5(b). This area is called the Field Weakening (FW) region.

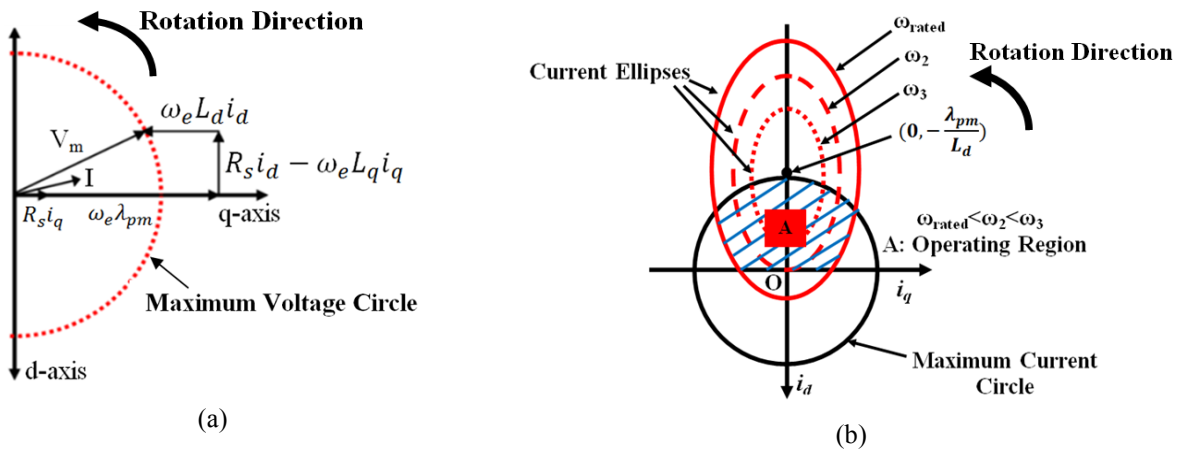


Fig 2.5 PMSM's a) Voltage vector diagram in d-q frame b) Current ellipses and current circle

According to Fig 2.5(b), if the fraction $\frac{\lambda_{pm}}{L_d}$ is decreased, the centre of the current ellipses can be shifted into the current limit circle. Designing a large d-axis inductance machine is a suitable method to fulfill this aim. In addition, in order to fully extract the reluctance torque in an IPMSM, the largest possible saliency ($\frac{L_q}{L_d}$) should always be taken into account as well. However, when the speed range of an IPMSM is widened by a high d-axis inductance, the saliency of the machine is reduced, because the denominator of ($\frac{L_q}{L_d}$) as the saliency ratio is increased. As the machine's circuit parameters are not independent variables, a compromise between a high d-axis inductance for having wide range speed and high saliency should be taken into account when designing the machine which makes the design procedure more complicated.

In an IPMSM, permeability of the d- and q-axis inductances is the function of the rotor laminations. Saturation in the d- or q-axis path results in the smaller inductances. The inductance of an IPMSM can therefore be adjusted by changing the rotor geometry, including for instance the magnet's shape, orientation and angle. In a V-shaped magnet IPMSM, there are more degrees of freedom to adjust the inductance of the machine such as changing the angle between the two pieces of magnet, defining the clearance between two pieces of magnets, or changing the shape of the flux barrier [24].

When defining and predicting the IPMSM performances and speed range, an analytical method for L_d and L_q calculations [25, 26] can be useful. However, many research studies do not rely on this method due to its complexity and low accuracy under highly saturated conditions of the machine. This thesis study uses the Finite Element Analysis to the IPMSM structure to investigate the rotor geometry variations and their impacts on the IPMSM's performance and inductances value.

Performance evaluations are carried out for the PMSMs with rotor geometry changes and various iron bridges in [27]. The main objective of [27] is to design an IPMSM model with high saliency that can be used in a wider speed range. In a design proposed by [27], the rotor geometry utilized a lower volume of magnet compared to the SPMSMs. The V-shaped magnet structure is selected by [25, 28, 29] for IPMSMs as a suitable configuration offering the widest speed range. A comparison is carried out in [30] between a V-shaped magnet IPMSM and two other rectangular shaped magnet IPMSMs showing that the V-shaped magnet IPMSM offers the

widest speed range. [31] indicates that the magnet width of the rectangular magnet IPMSM can be precisely defined to adjust the L_d and L_q of the machine for wide speed range and high torque density operations. [29, 32, 33] investigate how setting the angles between two pieces of magnets in the V-shaped magnet IPMSM can be done to design a final model with wide speed operation. In [34], two layers of magnets are inserted into the rotor structure of an IPMSM increasing the saliency of the machine and widening the speed range. The segmented magnet rotor structure is analyzed and offered in [35, 36] to introduce an IPMSM model with wide range speed performance. In [35, 36], bridges are introduced in each pole to increase the d-axis inductance.

Modifying the flux barrier is helpful to reduce the flux leakage and tune the inductances in the IPMSM rotor structure. In [37, 38], the flux barrier shape is adjusted in the rotor structure of IPMSMs to propose an IPMSM with wide speed range characteristic. Another interesting rotor structure, called Machaon, is proposed by Bianchi et al in [39] for high power density and wide speed range operations. The main scope of study by [39] is optimizing the flux barrier's shape to finalize a proposed IPMSM model.

In another study [40], instead of using the flux barrier, a non-magnetic shaft sleeve is used in the rotor geometry to adjust the inductances and the saliency of the IPMSM for the high speed performance. Hybrid rotor structures are also proposed in [41, 42] for wide speed range and high torque applications: [41] presents a rotor comprised of the buried magnet and surface magnet; [42] presents one comprised of the radial and circumferential magnet orientations. The hybrid rotor structure is helpful to enable two rotor capabilities at the same time.

In [43, 44], the stator physical structure modification is considered as another suitable alternative for high torque density and wide speed range operation. A similar modification is done by [45] in the form of optimally tuning the stator slot opening to increase the saliency of machine and support the required power for the wide speed range operation. In addition to the rotor and stator physical modifications, the stator winding modification is noticed as the other important alternative in [46- 49] to widen the operational speed range of an IPMSM by reducing the losses of machine.

The results of the above mentioned research studies provide evidence of the advantages of geometry modifications in widening the speed range and operating region. Thus, these motor

geometry changes can be beneficial in the final IPMSM design for wide speed range performance and promising developed torque capability.

In order to introduce an IPMSM with promising saliency, low Back-EMF harmonic contents, and capable to be used in wide speed range applications, different physical changes are applied to the rotor geometry of a V-shaped magnet IPMSM in this work,. These changes aim to adjust the d- and q-axis paths reluctances for inductance increment and to reduce the harmonic content of the air-gap flux density by the parametric design of experiments procedure.

The speed range over which constant rated power can be maintained is known as the Constant Power Speed Range (CPSR). Fig 2.6 shows the constant power area in the FW region above base speed and constant torque area below the base speed. CPSR is the focus of the analysis carried out in this thesis and constant torque region is only shown for general information.

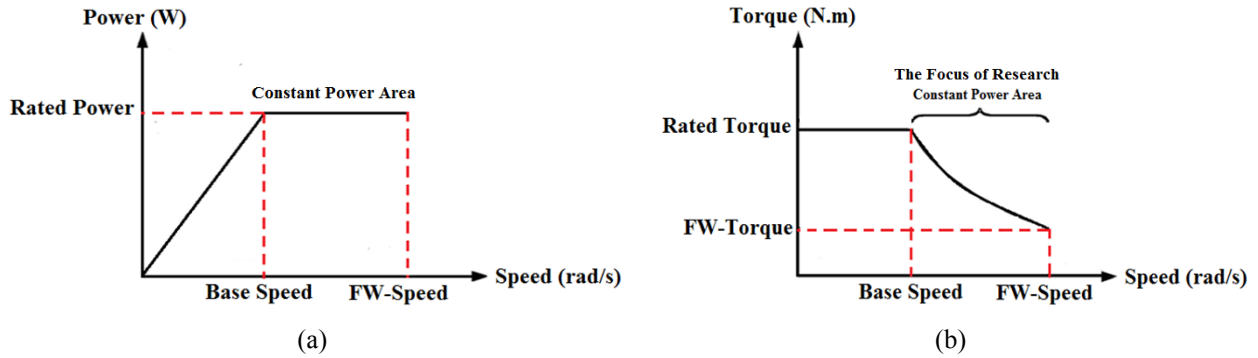


Fig 2.6 Curves showing Field Weakening (FW) region, a) Power versus speed and b) Torque versus speed

After base speed, the i_d current of machine should be set in a way that both current and voltage limitations are fulfilled and the required power is supported. Using an offline look-up table is the first method that can be employed to specify the required i_d current in each operating point in FW area [50]. In this method, the required i_d current in each operating point is calculated offline and then used during the experimental analysis of the IPMSM in the wide speed range. The most important disadvantages of this method are its complexity and lesser accuracy as the inductances of the IPMSM are not fixed in all operating regions and vary non-linearly. The offline calculation of the required i_d current is not always reliable especially when the L_d and L_q of the machine vary considerably in the wide speed range.

The second method of i_d tuning is adjusting it manually. In this method, the i_d current is manually set during IPMSM performance while the current and voltage limitations of the machine in each operating point are taken into account. This method is utilized in this thesis in a wide range of speeds. Although the method is not suitable for having optimized efficiency performance, it is simple and can be easily applied.

In addition to these two methods, a voltage-angle based control method for FW region control of IPMSM is proposed in [51]. Current regulation control gives a fixed q-axis voltage command while the d-axis current is actively controlled simultaneously for the FW region [52]. Frozen permeability technique [53], adjusting the winding turn numbers [54], the physical movement of magnets in the rotor due to the centrifugal force [55], establishing a partial magnetic short circuit between rotor permanent magnets [56], and the optimal reference i_d current trajectory [57] are among the other interesting methods used to control the IPMSMs in their FW region.

According to the information described by section 2.1, designing a large L_d IPMSM using motor geometry changes, or applying more voltages on the machine's phases are the beneficial methods used to extend the speed range of IPMSMs in the FW region. In addition, the d-axis current tuning should be effectively carried out in the FW region to offer a reliable performance.

2.2 Concentrated and Distributed Windings

The winding configurations in electrical machines can be classified as either distributed or concentrated [58, 59]. Distributed windings have been used for different types of electrical machines for many years. Concentrated winding have become common in the PMSM over the past decade.

Concentrated windings refer to the windings that attempt to eliminate any end-winding overlap with other phase windings.

Examples of the overlapping distributed winding and concentrated winding schemes are shown in Fig 2.7(a) and Fig 2.7(b) respectively. In addition, the nonoverlapping all teeth wound and alternate teeth wound concentrated winding configurations are indicated by Fig 2.7(c) and Fig 2.7(d) [59].

For non-overlapping single layer winding: The winding coil is wound around every second tooth of the stator core. Hence, the pattern number of coil is half of the slot number. There is a

flexibility to vary the coil pitch in order to improve the machine performance. For the reduction of cogging torque, variable slot pitch can be used instead of skewing the rotor [60].

For non-overlapping double layer winding: The winding coil is wound around each tooth of the stator core. Hence, the number of coil is equal to the number of slots. As the coil pitch is fixed, skewing the rotor can be a useful method for reducing the cogging torque [60, 61].

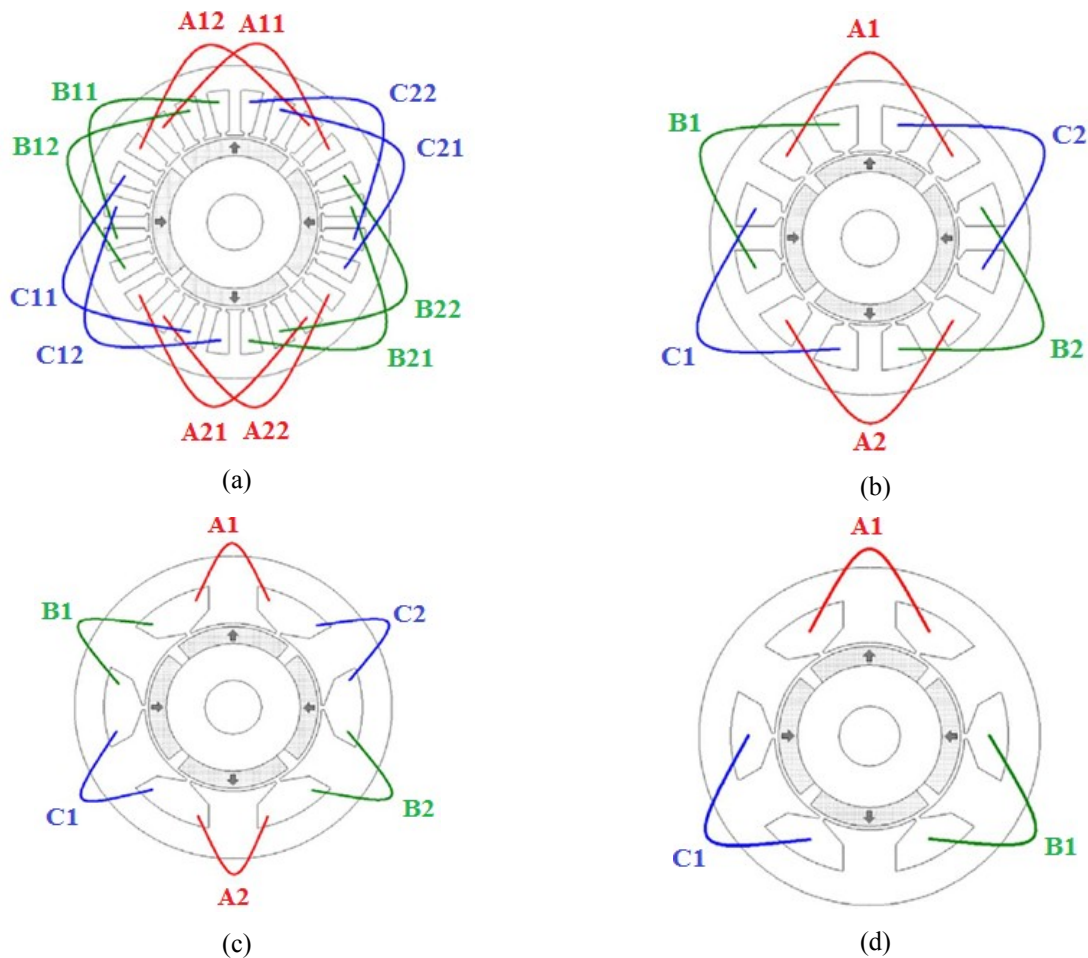


Fig 2.7 Typical stator winding configurations (four pole), (a) Twenty-four slot, overlapping. (b) Twelve slot, overlapping. (c) Six slot, nonoverlapping, all teeth wound. (d) Six slot, nonoverlapping, alternate teeth wound [59]

Concentrated windings offer some significant advantages over distributed windings [62]. These include: 1) significant reduction in the copper volume and copper losses in the end region; 2) significant reduction in the machine total length; 3) reduction in machine manufacturing cost; 4) compatibility with segmented stator structures which makes it possible to achieve significantly higher slot fill factor values. Higher slot fill factor enables more turns in a given slot resulting in higher inductance.

Concentrated winding is a suitable winding option in industrial applications. This winding configuration is preferred for having more power density and wide speed range applications, due to the higher magnetization in the rotor structure [63]. It is also capable of providing more salient [64], shorter teeth [65], and high inductance IPMSM [61, 66]. In addition, the inductance of the IPMSM can be well-adjusted by this winding configuration for high power density and wide FW applications [67, 68]. Furthermore, concentrated winding is a suitable option for some special applications like low speed direct drive [69], outer rotor PMSMs [70], and Hybrid Electric Vehicles (HEVs) [71]. Concentrated winding can be a useful alternative to improve the efficiency in high speed performance by having an increased number of layers in the winding configuration [58, 72]. After consideration of these capabilities and advantages over distributed winding, the concentrated winding structure is selected for the machine design and analysis in this work.

In addition to the type of winding, the Slots per Pole per Phase (SPP) should be selected in a careful way. SPP, which sometimes is called q in literatures, is defined in a concentrated winding PMSM by [58]:

$$SPP = \frac{Q_s}{p \times m} \quad (2.14)$$

The criteria for choosing the preferred SPP values have been identified by many authors [32, 62] as follows:

- The lowest common multiple (LCM) of the number of stator slots (Q_s) and the number of rotor poles (p) should be as high as possible. The harmonic frequency that corresponds to this LCM order value represents the cogging torque frequency. As a result, choosing SPP values to increase this LCM value raises the cogging torque frequency and lowers its magnitude.
- The greatest common divisor (GCD) of the product of the number of stator slots and the number of rotor poles must be an even number. This GCD value is an indication of the machine's symmetry. If it is an even number, the net radial force on the machine will be very low.

The double-layer winding is selected as the base layout in studies with high frequency performances due to its lower losses in higher speeds [59]. In addition, a vertically divided layer

would be better than a horizontally divided layer to reduce the end winding length and loss [73]. According to the mentioned advantages of the concentrated winding schemes especially including less losses, high inductance and less manufacturing price, so the concentrated, double layer, vertically divided winding is selected as the desirable winding configuration for the Thesis study.

2.3 Losses

The main equations and concepts relating to the definition and evaluation of losses in the PMSM performance are briefly covered. The losses definition and evaluation is the main tool to predict and assess the efficiency of the designed and the built machine.

The main types of losses to be considered in PMSM application are electrical and mechanical losses.

Electrical losses include the copper loss, iron (core) losses, and magnet loss. The iron loss includes hysteresis and eddy current losses. In this study, multiple strands of conductors are used for each coil, and high frequency effects on the copper loss are neglected.

The iron loss, which is the function of hysteresis and eddy current losses, is expressed by equation (2.15) [74]:

$$P_{Iron} = k_e f_e^2 B_{max}^2 + k_h f_e B_{max}^{\eta_{st}} \quad (2.15)$$

A general definition of eddy current loss indicates that it is not only a function of the fundamental component of flux density but also of all other harmonics as well. So the general definition and equation for eddy current loss anticipation, taking into account the flux density harmonics, is expressed by equation (2.16) [75].

$$P_{Eddy-current} = \frac{h^2 \sigma}{12} \left(\frac{d}{dt} B_n \sum_{n=1}^{\infty} \frac{1}{n} \sin(n\omega_e t) \right)^2 \quad (2.16)$$

According to equation (2.16), if the amplitude of flux density's higher frequency components is reduced, the total eddy current is consequently reduced. Higher frequency components are always seen in flux density waveform in a concentrated winding PMSM. Using a double layer winding structure reduces the amplitudes of high frequency components.

The Finite Element Method (FEM) is commonly used to predict the electrical losses of the IPMSM. This method is employed as an example by [76] and is used in this thesis study as well.

In addition to the usual FEM analysis, other interesting methods exist to investigate the iron loss in electric machines. An IEM formula is used in order to include the higher order harmonics of flux density to precisely calculate the iron loss of machine [77]. Analytical prediction [78], conventional three term expression [79], a combination of stress analysis and EMF analysis [80], and surface function fitting process to create a generalized loss function [81] are among the other attractive approaches for iron loss evaluation. In addition, [82, 83] take into account the magnetic characteristics nonlinearity for more accuracy in loss evaluation for IPMSMs performance.

An additional type of loss related to the machine's phase current and phase resistance is copper loss. Compared to other electric losses, copper loss is usually the largest electric loss in the machine. Equation (2.17) is presented for copper loss evaluation.

$$P_{Copper} = 3I_{ph}^2 R_s \quad (2.17)$$

If phase current is increased, the total amount of copper loss is enhanced as well. This means that copper loss is directly affected by the machine's drawn current. Phase resistance is literally the phase windings' resistance. This resistance is function of winding (conductor) length, conductor's area and material conductivity. The frequency dependent variations in resistance value are neglected in this thesis.

The time varying magnetic field may cause other losses on magnets which are thereby called Magnet losses. In an SPMSM, a magnet loss is more significant due to the structure and placement of the magnet in the outer surface of the rotor [15]. This physical structure increases the magnet's exposure to air-gap flux density variations. As a result, more eddy currents are induced on a magnet's surface increasing loss in the magnets. In the IPMSM, however, the magnets are buried and are therefore not significantly exposed to the air-gap flux density variations. Accordingly, less magnet loss is expected in the IPMSM [15, 84].

Bearing, friction, and windage losses are the main types of mechanical losses in the performance of electric machines [85-87]. According to [85-87], Friction and windage loss is usually bigger and more dominant than bearing loss especially in high speeds. That is why this loss is evaluated in experimental analysis of this Thesis work.

2.4 Voltage Source Converter fed PMSM

A Voltage Source Converter (VSC) is used for the motor drive in this thesis work. A schematic view of a VSC fed IPMSM and its different parts is presented by Fig 2.8 [88].

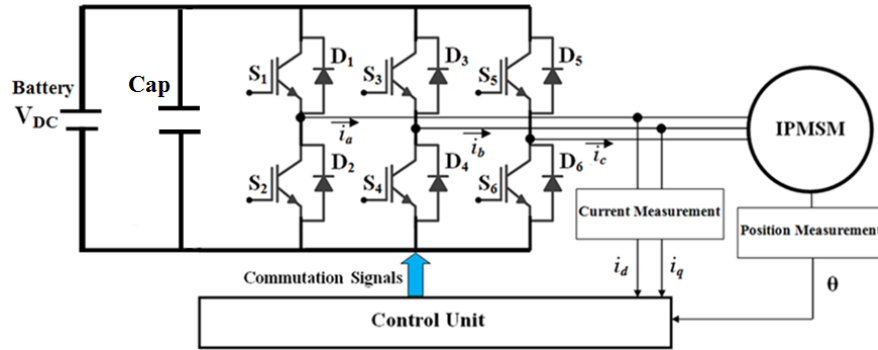


Fig 2.8 Diagram for a Voltage Source Converter (VSC) fed IPMSM [88]

A VSC fed IPMSM drive is comprised of the following different elements:

- A DC link, which is a DC voltage (V_{DC}) used to support the required power to the machine phases.
- Switches (S_1 to S_6), which are responsible for transferring the power to the IPMSM's phases based on the operating point of the machine.
- The control unit, which uses a digital signal processor to apply the digital commands to the gates of the power electronic switches in the VSC.
- Gating or commutation signals, which are commanded by a control unit to exactly specify which switch should be on or off in the VSC.
- Current measurement unit, which measures the current flowing through the phases of the machine and are utilized to command the control unit based on the operating point of the machine.
- Position measurement, which is carried out by an encoder mounted on the shaft of the PMSM and is used in d-q to abc frame transformation for the motor control purposes.

In a VSC fed IPMSM the maximum phase voltage of the machine supported by the converter is calculated by equation (2.18):

$$V_{Phase-Peak} = m_a \frac{V_{DC}}{2} \quad (2.18)$$

Where, theoretically, $m_a=1.15$ in Space Vector Modulation schemes [89].

2.5 Open Winding AC Machines

An approach to increase motor voltage from a given DC supply is to use an open winding machine. Conventional three phase AC machines usually have either Delta (Δ) or Wye (Y) connections. The open winding AC machine has the same internal phase winding implementation. However the winding structure does not include any neutral point or delta terminations. The six leads of the three phase windings are brought out of the machine and are supplied by two inverters. These two inverters have two DC power sources which can be isolated [90] as is illustrated in Fig 2.29 or can be the same [91]. Using two batteries for two inverters as their sources of energy in their DC links is common, but the cost of batteries and the whole drive system should always be taken into account. To overcome this issue, the DC input of one inverter can be supported by using a battery, and the second inverter can be supplied by the DC voltage from a controlled voltage capacitor. The first source of energy using a battery DC source is called Main Bridge (MB), and the inverter which has the capacitor in its DC link is called Floating Bridge (FB). Using these two inverters to apply the voltages simultaneously on the machine's phase can increase the machine's terminal voltage. This results in a wider speed range and operating region of machine. An open winding AC machine using a dual inverter drive structure and a floating capacitor is presented in Fig 2.9.

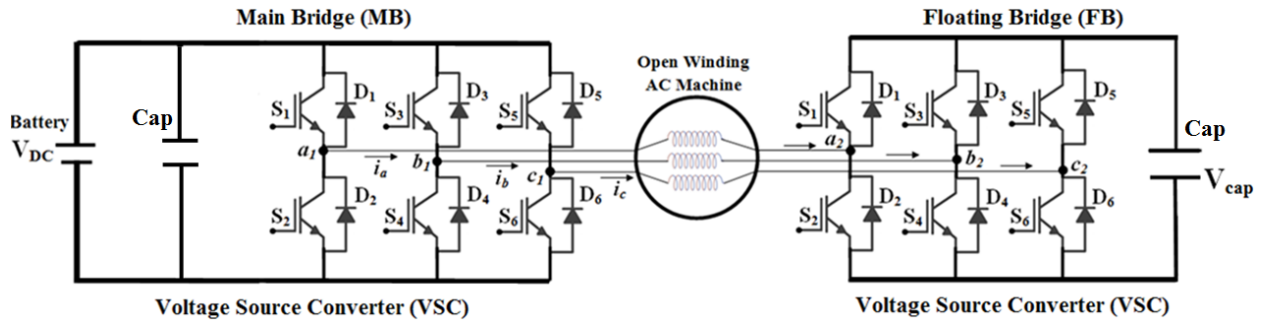


Fig 2.9 The open winding AC machine using a dual inverter drive structure

The performance improvement for the VSC-fed open winding Induction Machines (IMs) using different bridges and modulation schemes [92-99] and controllers [100] have been investigated in the recent decades. Despite the IM case, lower attention has been paid to the open winding PMSM using a dual inverter drive. However, several other studies have been done for the open winding PMSMs using a dual inverter drive: modulation scheme investigations for the drive efficiency improvement [101-103]; new inverter topology to improve the power capability

[91]; contribution in grid connected configuration [104]; and high capability for use in multiphase structures and fault tolerant capability [105, 106].

Different controlling approaches for the open winding PMSMs using the dual inverter drive structure are another important research area. Without a reliable controller, applying the required voltage on PMSM's phases and employing the machine in a desired performance are impossible.

The research studies investigate the aspect of controller schemes. In [90], a double-ended inverter-fed PMSM for hybrid vehicles is studied along with a number of other control methods: unity power factor control method, voltage quadrature control method, and optimum inverter utilization control method. In the work presented by [90] two fixed DC voltage sources are used for two inverters. In [107], the FW control of an open winding PMSM is investigated. Both sides of the open windings are connected to the two isolated inverters with fixed DC link voltages, which illustrated that the torque capability of the open winding PMSM can be increased compared to the Y-connected machine. In this case, two sources of energy are simultaneously used to apply the extended voltage on the machine's phases and conclude the operating region extension including the torque capability. Authors in [108, 109] investigate the possibility of extending the operating region of a PMSM constrained by a given power-supply voltage by using an open winding motor drive configuration. In their study, a second inverter with a floating capacitor is controlled to provide reactive power to the motor. The study also tried to increase the systems equivalent inductance by making the impedance seen from the FB side to be inductive which forces the characteristic current of PMSM to be consequently less than its rated current. In [110], a dual inverter drive with floating capacitor is controlled and investigated for an open winding SPMSM. However, the main trait of the studied machine is its low inductance, causing the contributions of study to be less influential. The drive has a voltage boosting function that accomplishes the following: extends the high-speed range of the PMSM; operates the main inverter bridge at unity power factor above the base speed; and, compensates for battery voltage fluctuations. In [111], a dual inverter drive with a floating capacitor is proposed for Hybrid Electric Vehicle (HEV) PMSM. The purpose of this structure is to accommodate high speed operation without increasing battery voltage. The secondary inverter does not carry a voltage source and is controlled to do the reactive power compensation in the motor drive. DC link voltage regulation for the secondary inverter is also achieved through the control of active power flow. In [112], an open winding PMSM is employed and controlled using

a hysteresis current regulator for high power wind generation applications. However, the controller used in this study is not well-defined or clearly explained, so more investigations in this application are required. Three control techniques based on modification of modulation scheme are proposed by [113, 114] to improve the FW capability of PMSM by applying more voltage on machine's phase, while a same DC link is used for both utilized converters. In [115], a controller is proposed for a dual inverter open winding PMSM to extend the CPSR of machine. In this study, the unity power factor from the Main Bridge side of the drive is fulfilled by the proposed controller, and the capacitor reference voltage is selected based on the operating region of machine. In [116], the dual inverter open winding IPMSM is designed and investigated by 2D-FEM. A control approach is briefly explained by some vector diagrams; however, the study presents no experimental verification.

The controller schemes presented by research studies above have one or more of the following drawbacks:

First, the triangular or rational functions of d-axis and q-axis currents, $[(\tan^{-1} \frac{i_q}{i_d})]$, $[(\frac{i_q}{i_d})]$, are used to set the reference angle [90, 107, 108, 109, 115], define the magnitude and angle of voltage vectors especially for Floating Bridge side [90, 107, 110, 111], and shift the d-q axis plane [108, 109]. Using the rational or triangular function of current is not a reliable way to set the voltage vector, reference angle, and shifting the d-q plane as there are infinite number of voltage magnitude and angle combinations when the PMSM is employed in high speeds and low current magnitudes. The capacitor voltage in the FB side overshoots in this case.

Second, the control approach is complex and hard to implement or requires modulation scheme changes [113, 114], or it is not clearly defined [112, 116].

Third, the controller is activated only after the maximum possible speed of machine in a single inverter drive structure [110, 116], and is not activated from the beginning. Activation of one of the bridges in high speed causes a severe disturbance to the drive performance.

It is also important to note that the PMSM utilized in the studies mentioned above is the Surface Mounted PMSM. Fewer studies and investigations have been carried out to control and analyze the open winding IPMSM as more complicated control scheme is required due to the d-axis current tuning above the base speed which is needed to exploit the reluctance torque.

2.6 Summary

The basic equations and definitions for PMSMs modeling are included in this chapter. It is shown that having the magnets buried into the rotor structure can contribute in three main aspects. The first contribution is to provide higher flux concentration, the second is to increase the torque capability of machine by adding the reluctance torque and the third one is to provide more degrees of freedom for changing the d- and q-axis inductances of the machine which all are helpful in setting the operational characteristics of machine including the maximum speed range and saliency.

It is shown in this chapter that relationship between the physical geometry and the circuit parameters is not clearly understood and the circuit parameters are not independent variables. A compromise between machine's different parameters is recommended to introduce a model which satisfies the suitable operational characteristics at a same time. This compromise complicates the machine design procedure.

It is shown that the speed range of an IPMSM is extended by designing a machine with increased d-axis inductance. In addition, providing more voltage on the phases of machine can be considered as the second alternative. In order to provide more voltage on the machine's phases either the DC link voltage of inverter should increase or two separate voltage sources can be applied simultaneously on the phases of the machine using the dual inverter drive scheme.

Concentrated winding is selected as the suitable winding configuration for the machine due to its advantages including less losses, lower manufacturing cost, and higher inductances. Combination of concentrated winding design with dual inverter open winding structure is recommended for the lower loss and wide speed range application. This structure can be considered as a suitable configuration for the fault tolerant applications preventing full voltage to be applied to the Main Bridge (MB) in the moment of the fault occurrence.

In order to fulfill the contribution of the dual inverter drive scheme in providing more voltages on the machine for operating region extension, a reliable and easy to implement Floating Bridge (FB) control approach is required which works finely both in high speeds as well as low currents operating regions.

Chapter 3

ELECTRIC MACHINE ANALYSIS AND DESIGN

In order to introduce a final model for an IPMSM, motor geometry changes are selected as the main tool. The performance evaluation of the 1kW V-shaped magnet IPMSM in different motor geometries is investigated to find a model with high d-axis inductance to provide wide speed range and promising saliency to support the required torque. During the design procedure, minimizing the cogging torque value and Back-EMF THD are taken into account.

The simulation investigations presented in this chapter are carried out using a widely used commercial Finite Element Method (FEM) based software (JMAG-Designer, 2012 version). In order to simulate the current controlled converter, a three phase controllable Current Source Inverter (CSI) is utilized and supply currents are modelled as ideal sinusoids. Automatic mesh generation is used and the mesh exploits 90° rotation periodic symmetry as one quarter of the machine's structure is drawn in the geometry editor window for saving the simulation time. The simulations are carried out and illustrated in the steady state at fixed speed with 128 discrete time steps per supply cycle. (The mechanical step size increases with supply frequency). The iron loss evaluation is carried out by the Fast Fourier Transform (FFT) analysis provided by the JMAG-Designer loss study option.

3.1 Initial Machine Specifications

Mathematical analyses are presented, in order to develop an initial machine design. The impact on winding design, pole number and external dimensions are investigated and presented.

3.1.1 PMSM Slot-Pole Combination Selection

The slot pole combination is mathematically analyzed and the reliable slot pole combination for an IPMSM providing high torque density is introduced.

The permanent magnet field and stator electromagnetic field interaction provides the required developed torque or electromagnetic torque (T_e) for the IPMSM. This developed torque is comprised of three parts called; reluctance torque (T_{rel}), cogging torque (T_{cog}) and electro dynamic torque [13]. See Equation (3.1) for the further clarity.

$$T_e = \frac{1}{2} i^2 \frac{dL_a}{d\theta_r} - \frac{1}{2} \lambda_{pm}^2 \frac{dRel}{d\theta_r} + k_w \cdot N_{phase} i \frac{d\lambda_{pm}}{d\theta_r} \quad (3.1)$$

Among the three parts of the developed torque two of them which are reluctance torque and electro dynamic torque should be maximized as they are positively contributing to the machine's power capability. On the other hand, the cogging torque should be minimized as it negatively affects the power and torque capability of the designed machine.

According to equation (3.1), electro dynamic torque is directly affected by the values of k_w (winding factor), the machine winding turn number (N_{phase}), phase current (i), and permanent magnet flux linkage (λ_{pm}).

An electrical machine with a low winding factor needs to compensate for its lower torque with higher current or a higher number of turns, both of which are inversely proportional to the winding factor.

In the third term of equation (3.1) the multiplication of the phase winding turn number (N_{phase}) with the machine's current (i) briefly explains the MMF effect on the machine's torque production. This implies that the MMF assessment and its effect on machine torque density increment should be taken into account.

3.1.1.1 Winding Factor Assessment

The winding factor assessment should be carried out as the first step of the machine design procedure to introduce the slot-pole combination of an IPMSM model with increased electro dynamic torque capability.

Generally, the winding factor is made up of three parts as shown in equation (3.2) [62].

$$k_w = K_p \cdot K_d \cdot K_{skew} \quad (3.2)$$

In concentrated winding machines, skewing factor (K_{skew}) is considered as one. Pitch factor (K_p) can be easily obtained mathematically.

Authors in [73, 86] have carried out studies on how the winding factor for a concentrated winding machine can be calculated. The following equations for winding factor assessment are based on their definitions and introductions.

Equation (3.3) shows the main equation for determining the type of winding in the studied machine as 1st or 2nd grade winding.

$$q = \frac{Q_s}{2.p.m} = \frac{z}{n} \quad (3.3)$$

Briefly, if n in the denominator is an odd number, then the winding structure is 1st grade. If n is an even number, then the winding structure is 2nd grade.

The pitch factor (K_p) in its n^{th} harmonic is calculated using equation (3.4) for a concentrated winding PMSM.

$$K_{p(n^{th})} = \sin\left(\frac{n^{th}.\pi\tau_{slot}}{2\tau_{pole}}\right) \quad (3.4)$$

According to equation (3.4), the pitch factor is the function of slot and pole pitches (τ_{slot} and τ_{pole}) in the machine.

The winding factor (k_w) for a 1st grade winding PMSM is given by equation (3.5).

$$k_w = \frac{\sin\left(\frac{v\pi}{2p.m}\right)}{nq.\sin\left(\frac{v\pi}{2p.m.nq}\right)} \cdot \sin\left(\frac{v\pi}{2p.m.q}\right) \quad (3.5)$$

The winding factor (k_w) for a 2nd grade winding PMSM is given by equation (3.6).

$$k_w = \sin\left(\frac{v\pi}{2p}\right) \cdot \frac{\sin\left(\frac{v\pi}{2p.m}\right)}{nq.\sin\left(\frac{v\pi}{nq.2p.m}\right)} \cdot \cos\left(\frac{v\eta_Y}{2p}\right) \quad (3.6)$$

Equations (3.4), (3.5) and (3.6) describe the winding factor assessment in a harmonic spectrum. The harmonics for 1st grade, and 2nd grade windings are given by equations (3.7) and (3.8) respectively.

$$\frac{v}{p} = \pm \frac{1}{n}((2mg) + 1) \quad g = 0, \pm 1, \pm 2, \pm 3, \dots \quad (3.7)$$

$$\frac{v}{p} = \pm \frac{1}{n}((2mg) + 2) \quad g = 0, \pm 1, \pm 2, \pm 3, \dots \quad (3.8)$$

In addition, it is clear that the slot pole numbers in a given machine have the most important role in winding factor determination. So, in order to have a broader investigation, the above mentioned equations are used for doing the winding factor assessment in different slot pole combinations.

3.1.1.2 MMF Assessment In PMSMS

According to equation (3.1), MMF waveform and its assessment have important influence on machine torque production and prediction. [62, 28] describe an investigation on MMF harmonic analysis and prediction in single layer and double layer winding PMSMs. This section includes the main equations for MMF evaluations.

The MMF-wave of order n for a coil fed by sinusoidal current is expressed by equation (3.9).

$$MMF_{(n)} = \frac{4N_{phase}}{n \cdot 2p \cdot \pi} \cdot \sin\left(\frac{n\pi \cdot \tau_{slot}}{\tau_{pole}}\right) \cdot \cos(n(\xi - \vartheta)) \cdot \hat{I} \cdot \cos(\omega_e t) \quad (3.9)$$

According to equation (3.9), MMF is the function of the machine's winding number (N_{phase}), poles and slots numbers, current (I) and electrical frequency (ω_e) of the supplied current, mechanical place of the point in which MMF is assessed (ϑ), and the speed of the MMF vector rotation (ξ).

Equation (3.9) implies that the MMF can be mathematically separated into two sinusoidal waveforms, rotating in opposite directions. The sinusoidal waveform must be repeated at least once over the entire periphery of the machine, due to the need for symmetry, which means that the minimum harmonic order is 2/poles.

The MMF waveform equation when the forward (M^+) and backward (M^-) MMF components are separated is shown by equation (3.10).

$$MMF_{3ph(n)} = \sum_{n=\frac{2}{2p}}^{\infty} \sum_{c=1}^{n_c} \sin\left(\frac{n\pi}{2} \cdot \frac{\tau_{cc}}{\tau_{pole}}\right) (M^+ + M^-) \quad (3.10)$$

M^+ and M^- are as follows:

$$M^+ = \hat{I} \cos(\omega_e t - n(\xi - \vartheta_c)) \cdot \left[\frac{1}{2} + \cos\left(\frac{2\pi}{3}(n-1) + 2\pi \cdot n \cdot n_y\right) \right] \quad (3.11)$$

$$M^- = \hat{I} \cos(\omega_e t + n(\xi - \vartheta_c)) \cdot \left[\frac{1}{2} + \cos\left(\frac{2\pi}{3}(n+1) + 2\pi \cdot n \cdot n_y\right) \right] \quad (3.12)$$

Some examples for the harmonic analysis of winding factor and MMF for three different slot pole combinations using equations (3.11) and (3.12) are presented by Fig 3.1 for further clarity.

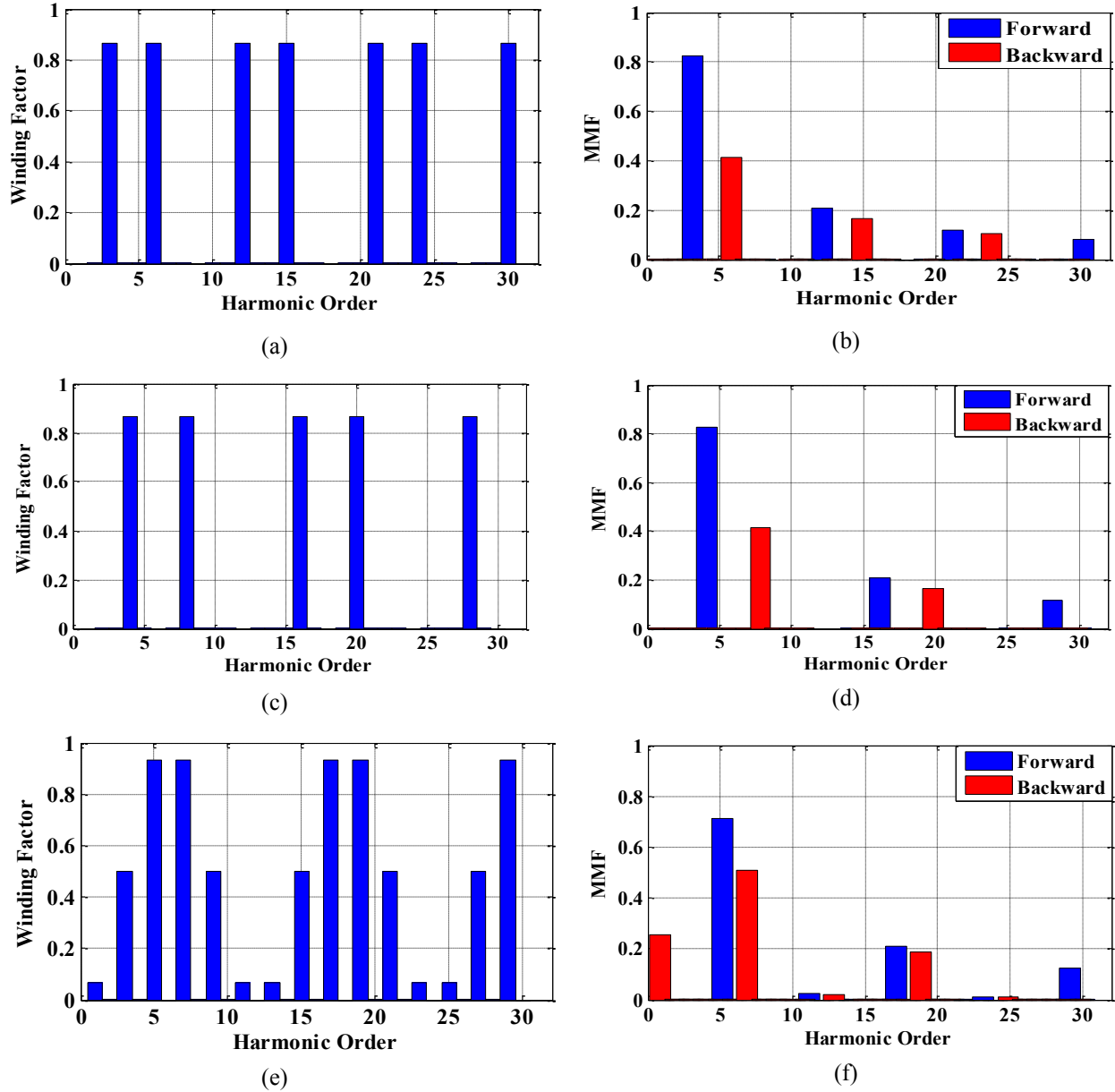


Fig 3.1 Winding factor and MMF mechanical harmonic spectrums for a, b) 9 slot 6 pole, c, d) 12 slot 8 pole, e, f) 12 slot 10 pole, double layer concentrated winding PMSMs

It is worth noting that, some slot pole combinations like 9 slot - 8 pole, 9 slot - 10 pole, 15 slot - 16 pole are not considered as the suitable slot pole combinations due to the high radial force [117]. These slot pole combinations are not considered for MMF and winding factor assessment.

Table 3.1 collects the k_w and MMF harmonic analyses for different slot pole combinations.

Table 3.1Detailed winding factor (k_w) and MMF assessment for different slot pole combinations

Slot	Pole	Max k_w	Max MMF	MMF $\times k_w$
9	6	0.866	0.827	0.716
9	12	0.866	0.827	0.716
12	8	0.866	0.827	0.716
12	10	0.933	0.712	0.664
12	14	0.933	0.712	0.664
12	16	0.866	0.827	0.716
12	20	0.5	0.955	0.477
15	10	0.866	0.827	0.716
15	20	0.866	0.827	0.716
18	14	0.902	0.738	0.665
18	16	0.945	0.677	0.639
18	20	0.945	0.677	0.639
21	14	0.866	0.827	0.716
24	16	0.866	0.827	0.716
24	20	0.933	0.712	0.664

According to the harmonic analysis for winding factor and MMF, the maximum value that can be obtained as the maximum multiplication of winding factor and MMF is 0.712. Accordingly, the first three options with 9 slot - 6 pole, 9 slot - 12 pole, and 12 slot – 8 pole slot pole combinations have the least number of poles and slots and offer the highest MMF and winding factor multiplication. 12 slot-8 pole combination is selected as it has higher LCM compared to 9 slot- 6 pole case and lower pole number compared to 9 slot-12 pole case.

3.1.2 Initial Dimensions for the Investigated IPMSM

Analytical calculation is utilized to find out the initial dimensions of the IPMSM based on the required performance.

As an example, the machine design steps are taken in a way to introduce a model with 1kW output power, an efficiency of 90% and 0.9 lagging power factor at base speed of 900 rpm or 60Hz of supply frequency. In addition, the DC voltage source of the VSC for machine drive is 320V. By taking into account these requirements and limitations and using some basic power

engineering equations as well as an influential analytical research by Bianchi [118], the various dimensions of the motor can be analytically calculated.

Some of the other important parameters which are taken into account during the machine design and its analytical dimension assessment are shown by Table 3.2.

Table 3.2

Some of the initially defined parameters for obtaining the machine's dimensions

Parameter	Value	Parameter	Value
Conductor current density (A/mm^2)	6.5	Back Iron flux peak (T)	2
Specific magnetic loading, B (T)	0.6	Slot packing factor	0.4
Efficiency (%)	90	Strands per turn	1
Winding layers	2	Copper resistivity ($\Omega.m$)	1.68×10^{-8}
Tooth flux peak (T)	2	Permeability, μ_0 ($N.A^{-2}$)	1.26×10^{-6}

Using [118], the most important machine dimensions can be easily calculated. [118] has assumed the physical structure of the PMSM as shown in Fig 3.2.

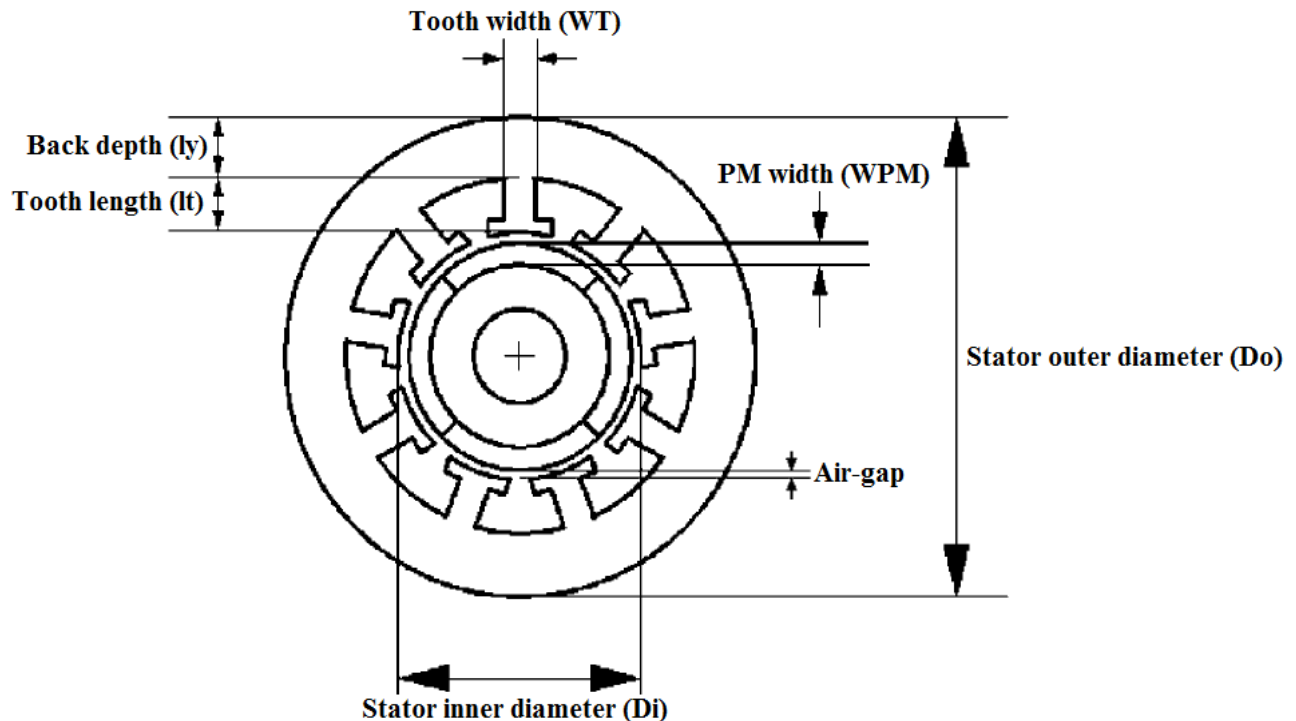


Fig 3.2 Different parts of the PMSM for machine design using analytical assessment [118]

For example, back iron depth (length) can be expressed as a function of the air-gap flux density ($B_{air-gap}$), pole number and stator inner diameter.

$$l_y = \frac{B_{air-gap} \pi D_i}{2B_y \cdot 2p} \quad (3.13)$$

The tooth length is found using stator outer diameter (D_o), and stator inner diameter (D_i) as shown in equation (3.14):

$$l_t = \frac{D_o - D_i}{2} - l_y \quad (3.14)$$

In this Thesis, the tooth width and back depth are set equal for having least iron losses. Bianchi has proposed equation (3.15) for tooth width evaluation.

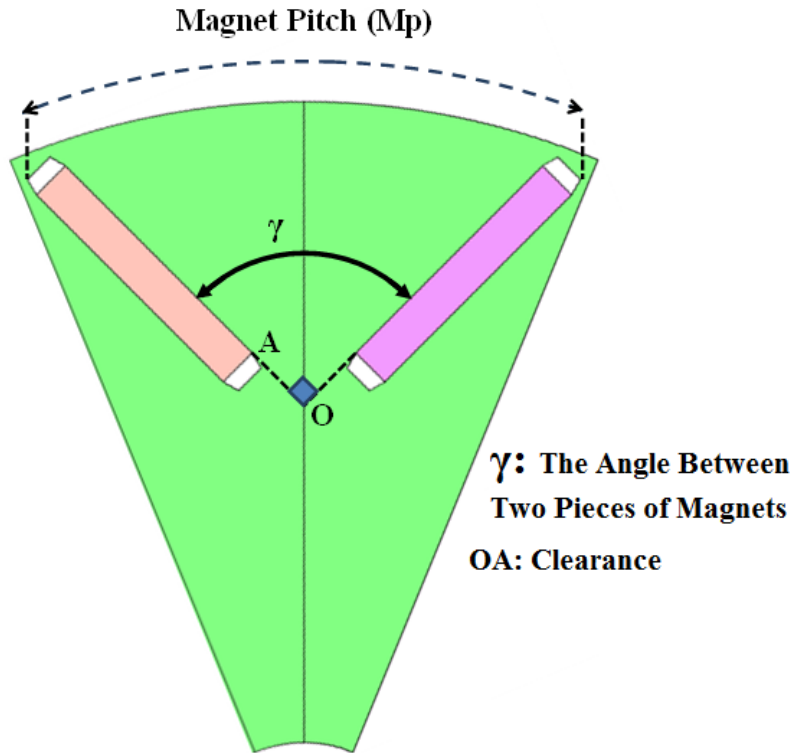
$$W_T = \frac{B_{air-gap} \pi D_i L}{B_t Q_s l_t} \quad (3.15)$$

Using the analytical calculations described by [118] and [86], and taking into account the information in Table 3.2, Table 3.3 below offers the initial dimensions and parameters of an IPMSM that fulfills the desired power requirement in the presence of the drive and machine limitations.

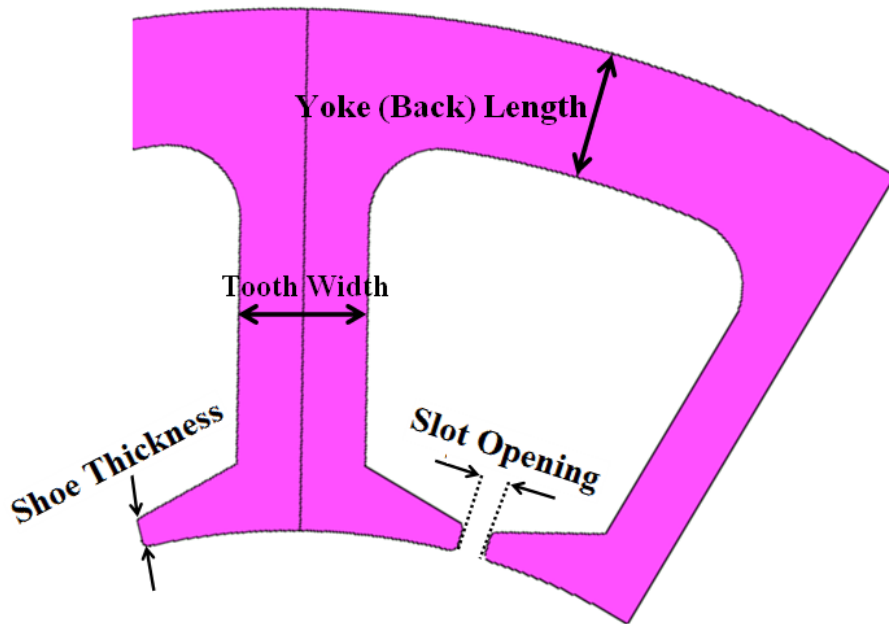
Table 3.3
IPMSM's general specifications using the analytical assessment

Parameter	Value	Parameter	Value
Power (W)	1000	Conductor area (mm ²)	0.5188 (AWG 20)
Rated Speed (rpm)	900	Phase resistance (Ω)	3.652
Slot-pole	12-8	Rotor diameter (mm)	90.13
Power factor	0.9	Tooth width (mm)	9.03
Maximum current (A)	5	Yoke (Back) length (mm)	9.03
Fundamental k_w	0.866	Stator outside diameter (mm)	165
DC link voltage (V _{DC})	320	Air gap (mm)	0.6-1
Conductor type	Copper	Shoe thickness (mm)	2
Coil turn	135	Stack length (mm)	50

The different parts of the stator and rotor in a V-shaped magnet IPMSM with 90° angle between two pieces of magnet (γ) are shown by Fig 3.3.



(a)



(b)

Fig 3.3 A piece of a) Rotor and b) Stator of a V-shaped magnet IPMSM

The most important dimensions required for the different parts of the PMSM are calculated analytically. But in order to have the best performance, the orientation of the magnets in the rotor

and some other minor changes, such as changes in the slot opening tuning or the shape of stator shoes, should be applied before finalizing an IPMSM model with wide speed range, low cogging torque, low Back-EMF THD, high d-axis inductance and high saliency.

As described in Chapter 2, the machine's inductance (L_d) can be maximized by changing the machine's initial geometry. Maximizing the d-axis inductance forces the IPMSM's characteristic current to be less than or equal to the machine's rated current. In this case, wide speed range is theoretically fulfilled, and the current ellipses' center is always placed inside of the current circle. The characteristics current (I_{ch}) and its mathematical relationship with d-axis inductance is described by equation (3.16)

$$I_{ch} = \left| \frac{\lambda_{pm}}{L_d} \right| \quad (3.16)$$

3.2 Impact of Rotor Geometry Changes on Performance of The IPMSM to Find the Initial Design

Geometry changes area applied to the V-shaped magnet IPMSM designs with different γ in order to introduce an initial model with big d-axis inductance, low cogging torque, and low Back-EMF harmonic content. The geometry changes affect the level of magnetization in d- and q-axis paths resulting in inductance adjustment and affect the harmonic content reduction in the air-gap flux density profile. The three main geometry changes are as follows:

- First, the inductance evaluation and performance assessment are carried out for different IPMSMs with various γ (30° , 45° , 60° , 75° , and 90°) when there is no constraint on the flux density of the utilized magnet. The magnet flux density varies from 1T to 1.4T.
- Second, the magnet clearance (OA in Fig 3.3(a)) between two pieces of magnets is tuned to see the effects on the model's performance and inductance evaluation.
- Third, the Magnet Pitch (MP) in each pole is arranged, and its effects on inductance changes and on the machine's performance are assessed.

For the initial design procedure, the ideal magnets found in JMAG- Designer library are used. Furthermore, no loss density consideration and limitation are taken into account to select the lamination for the initial design steps.

3.2.1 Impact of γ Changes with no Constraint on the Magnet's Flux Density

The performances of five different IPMSMs with different γ are evaluated. There is no constraint on their magnet densities (B_r), and the full magnet pitches and wide clearances are initially set. The B_r of the utilized magnets varies between 1T-1.4T. The inductance, Back-EMF voltages using equation (3.17), Back-EMF THDs using equation (3.18), and cogging torques comparison for these five cases are illustrated in Fig 3.4. For all cases, the machines should be able to fulfill the rated power of 1kW in base speed of 900rpm with the peak phase voltage of $m \cdot \frac{V_{DC}}{2} = 184V$ (m is modulation index which is 1.15 in SVM) and the maximum peak current is 5 A. In equation (3.17) V_h is the peak of induced voltage in h_{th} harmonic obtained from Fast Fourier Transform (FFT) analysis.

$$Back - EMF_{rms} = 2\pi f_e \frac{N_{phase} k_w 1 \cdot \lambda_{pm}}{\sqrt{2}} \quad (3.17)$$

$$THD(\%) = \frac{\sqrt{\sum_{h=2}^{\infty} V_h^2}}{V_1} \quad (3.18)$$

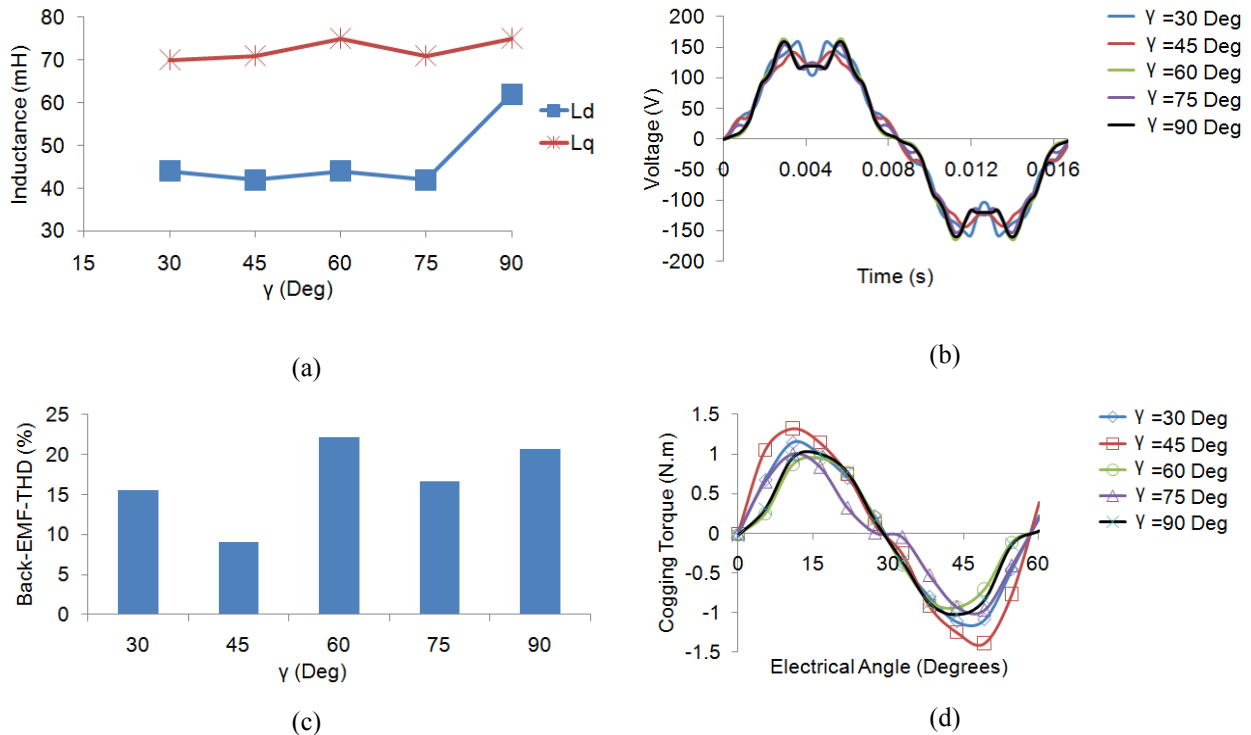


Fig 3.4 a) Inductance evaluation, b) Back-EMF voltages, c) Back-EMF THDs, d) Cogging torques for five different machines with different γ and without any constraint on the utilized magnets (900 rpm)

The design results using the first series of geometry changes are summarized as follows:

A γ of 90° produces the biggest d-axis inductance results in the magnitude of characteristic current to be very close to the rated current of machine. Accordingly, a high speed performance can be expected by this design, although high saliency is still not fulfilled.

To fulfill the rated power, the winding turn number varies in different γ . This explains why the inductance in 90° γ is bigger than the other cases as it has more winding turn.

Back-EMF analysis and the THD show that, although a machine with γ of 90° has high inductance, large voltage harmonics are still produced. This should be minimized in the next steps of the design procedure.

The peak of cogging torque for the machine with a γ of 90° is among the lowest peaks of other machines. However, its peak is still 1N.m, which causes approximately 10% cogging torque peak. In the final model, this peak will be reduced as much as possible.

When there is no constraint on the magnet flux density, the IPMSM with a γ of 90° is considered a suitable option with the highest d-axis inductance and low cogging torque in comparison with other IPMSMs with 30° , 45° , 60° , and 75° γ . Therefore, the widest speed range can be expected from 90° γ IPMSM case.

3.2.2 Impact of Clearance Changes

Three different V-shaped magnet motors with different γ of 60° , 75° , and 90° are simulated while the Magnet Pitches (Mps) are kept on maximum, and the impact of opening the clearance between the magnets is investigated on the machines' performance. Conventionally, in a V-shaped magnet IPMSM, the clearance between magnets is minimized, so as to reduce leakage flux from the magnets. The impact of this choice is to significantly reduce L_d . If speed range is not a concern, this is a beneficial step, increasing saliency and providing additional torque capability.

The Back-EMF voltage waveforms, their THDs, and cogging torques comparison for the three introduced IPMSMs with different γ using a minimum clearance between adjacent pieces of magnets are shown in Fig 3.5. The minimum clearance is set at 1mm for all cases. On the other hand, the performance evaluation in wide clearance is illustrated by Fig 3.6. The wide clearance varies between 3.5mm to 4mm in the evaluated IPMSMs.

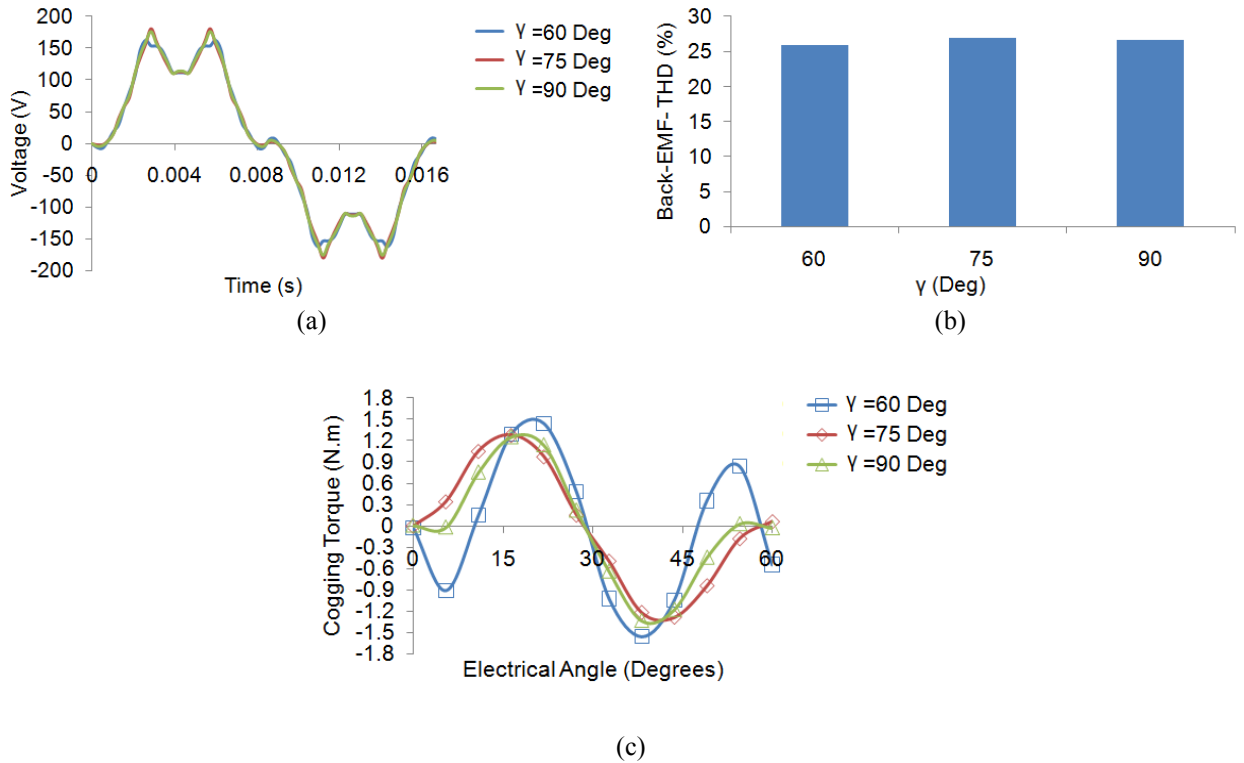


Fig 3.5 a) Back-EMF voltages, b) Back-EMF THDs, c) Cogging torques, for three different machines with different γ and minimum clearance (900 rpm)

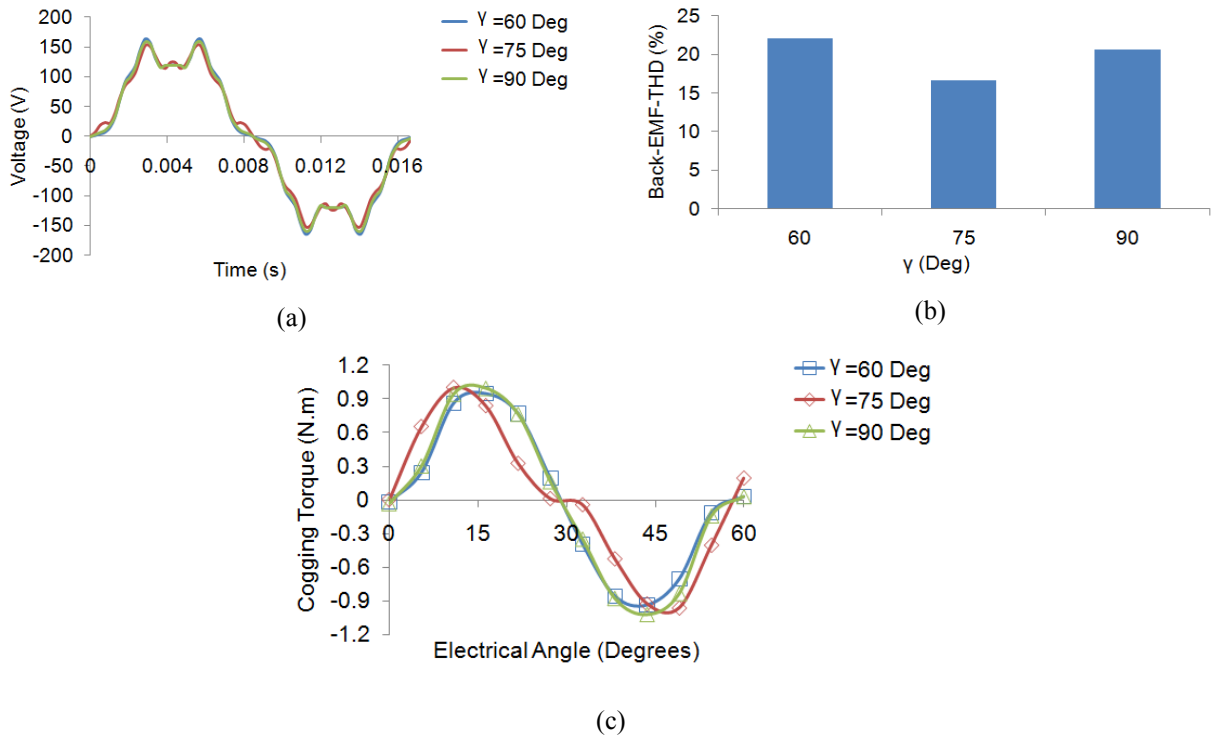


Fig 3.6 a) Back-EMF voltages, b) Back-EMF THDs, c) Cogging torques, for three different machines with different γ and wide clearance (900 rpm)

The d-axis and q-axis inductance evaluation for the IPMSMs using three different γ (60° , 75° , 90°) and in minimum and wide clearances are shown by Fig 3.7.

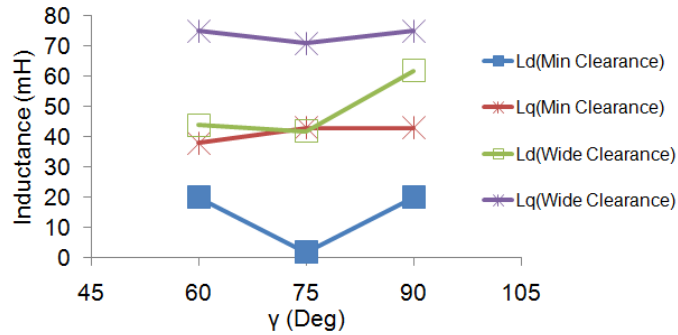


Fig 3.7 L_d and L_q evaluation using the wide and minimum clearances in three different V-shaped magnet IPMSMs

The summaries of design steps in this section are as follows:

The 90° γ IPMSM design shows the highest L_d inductances in both minimum and wide clearances, due to higher winding turn number compared to the other γ .

When a wide clearance is set between the two pieces of magnets in each pole, higher inductances are seen for all three different γ . In the wide clearance the reluctance of d-axis flux path is reduced causing the bigger L_d .

Increasing the clearance increases the L_d at the expense of saliency, especially at wider angles between the magnets. In order to maintain λ_{pm} , the magnet strength has to be increased by 0.2T, and the number of turns has to be increased from 135 turns with the minimum clearances to 145 turns with the wide clearances. With inductance proportional to turns squared, it is clear the change in L_q seen in Fig 3.7 is due to more than just the change in the number of turns.

7% of rated torque is seen for the cogging torque profile of the designed 90° γ IPMSM with the wide clearance. This should be minimized further in the final design.

Unfortunately, high Back-EMF THD is seen for six designed machines. The reduction of THD in the Back-EMF for the final model should be the other main objective.

The B_r of the magnet for 90° γ case is 1.4 T which is too high. In the final design, lower flux density magnet should be taken into account to reduce the cost and demagnetization problem.

Briefly, setting the wide clearance between the adjacent magnets in each pole can result in a big d-axis inductance and low cogging torque.

3.2.3 Impact of Magnet Pitch Changes

At the third design stage, further evaluation is carried out for Back-EMFs and their THDs, cogging torque and inductances for three different γ of 45°, 60°, and 75° using wide clearance, while their magnet pitches are set on 85% and 100% (See Fig 3.8, Fig 3.9, Fig 3.10).

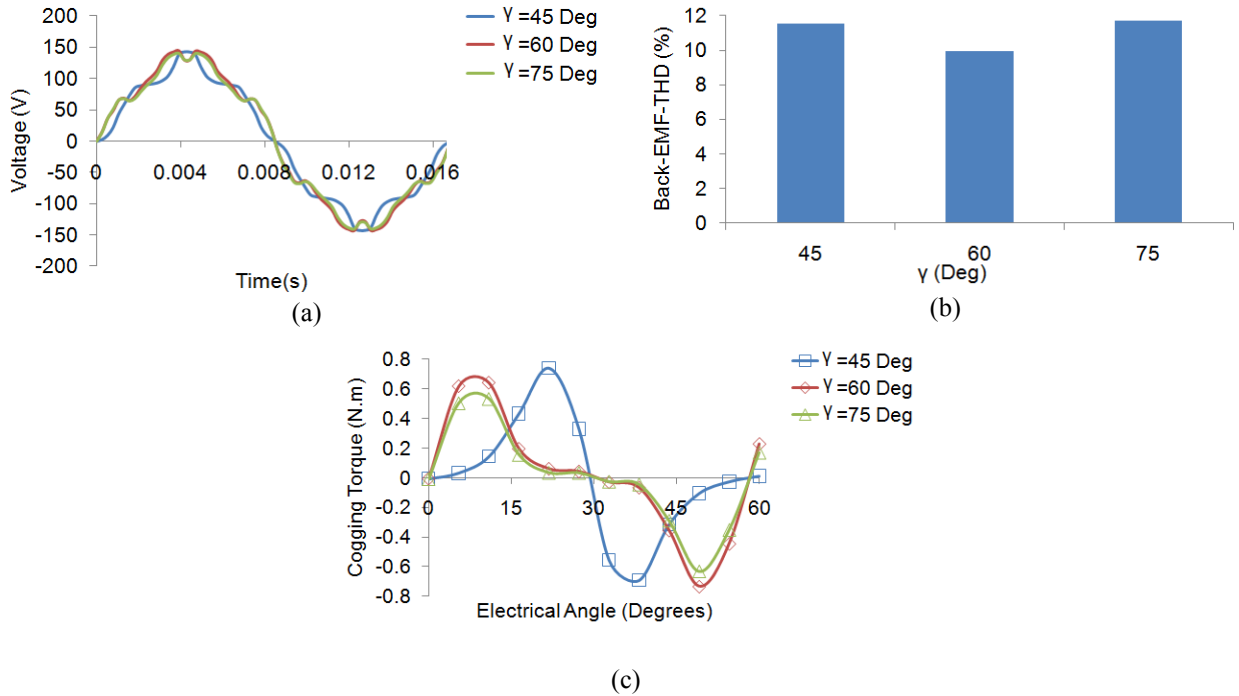


Fig 3.8 a) Back-EMF voltages, b) Back-EMF THDs, c) Cogging torques, for three different machines with different γ and 85% magnet pitches (900 rpm)

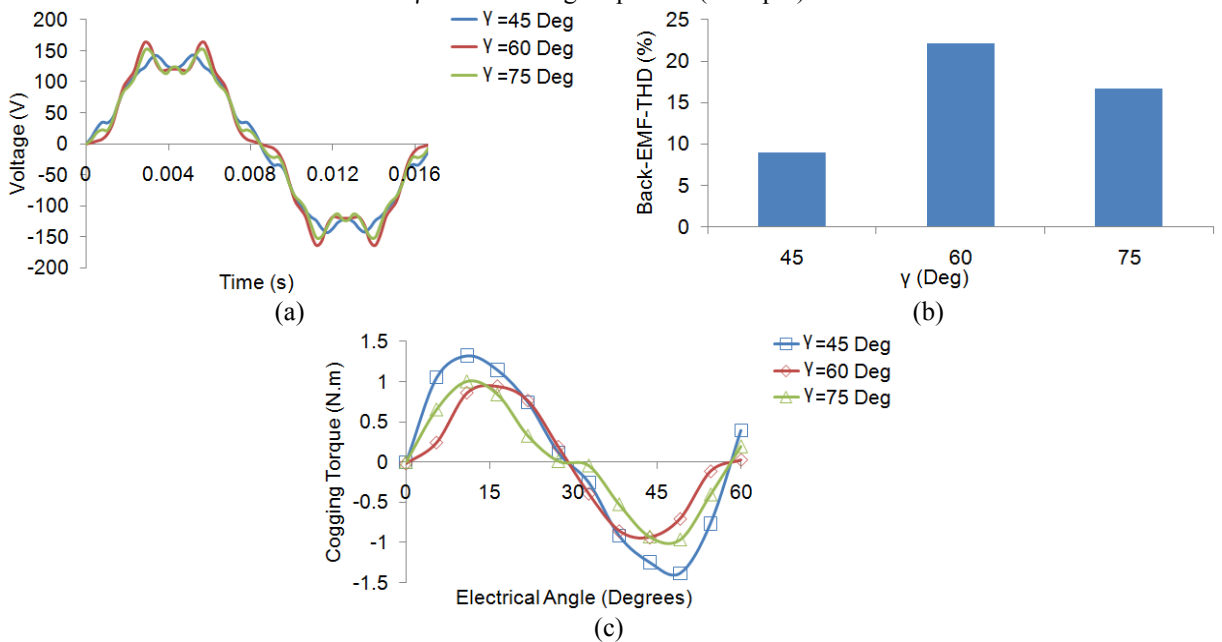


Fig 3.9 a) Back-EMF voltages, b) Back-EMF THDs, c) Cogging torques, for three different machines with different γ and 100% magnet pitches (900 rpm)

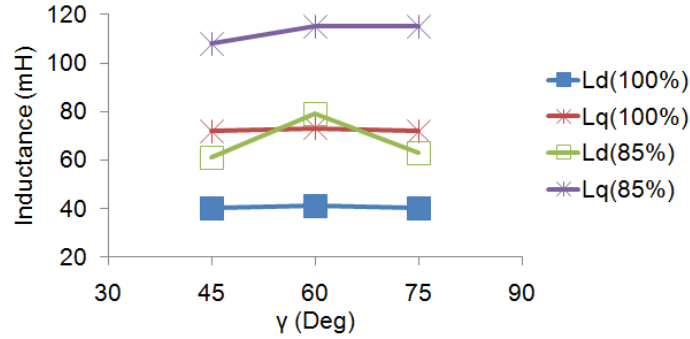


Fig 3.10 L_d and L_q variations in 100% and 85% magnet pitches for three different γ IPMSMs

The summaries from the analysis carried out in this section are as follows:

An inspection of Fig 3.8 shows that reducing the magnet pitch will have two positive impacts: (a) the harmonic content of the air-gap field will be reduced, improving voltage THD; (b) the q-axis flux path will have lower reluctance, resulting in higher L_q and saliency ratio.

The simulations demonstrate that reducing the magnet pitch to 85% can reduce the cogging torque to even 3% of the rated torque.

In the case of a reduced magnet pitch, the higher B_r magnet is used to provide the required torque.

Briefly, reducing the magnet pitch is a useful option to increase the machine's inductances.

3.2.4 Initial Design Summary

The impacts of clearance changes and magnet pitch changes when there is no constraint on the B_r of the utilized magnet and in different γ are thoroughly evaluated especially on inductance changes, cogging torque assessment, and Back-EMF harmonic analysis. Some benefits and disadvantages are briefly explained in each section, and accordingly a 90° γ , with wide clearance and 85% magnet pitch is selected as the initial design showing the highest potential for inductance increment, least cogging torque and low harmonic contents. The physical structure of the initial design using the introduced investigations is shown in Fig 3.11.

The main drawbacks for this initial design are the high B_r for the utilized magnets, no considerations on the loss density, and sharp edges on the stator's teeth. These drawbacks are resolved in the final model by applying some physical and material refinements to the initial model.

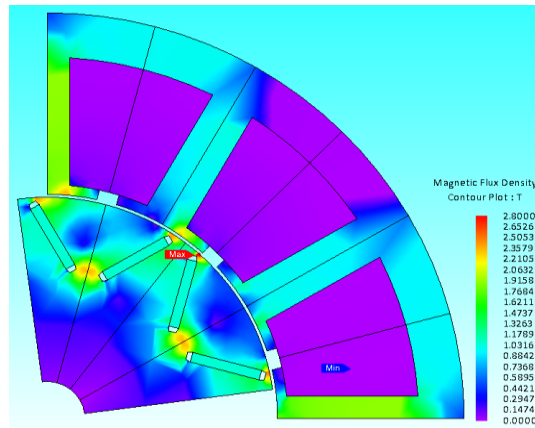


Fig 3.11 The initial design of the IPMSM

3.3 Design Refinement

The initially designed IPMSM presents a number of problems in its physical structure as well as in the cores and magnets used in its structure. Therefore, the following physical and material modifications are applied to the design to produce a more reliable final model:

- In the IPMSM design results described in section 3.2, all the shoes are T-shaped. These should be changed to an angled shape so that loss reduction and saturation are seen in the stator part. In addition, other sharp angled edges that are seen in the junction of the teeth and yoke of machine should also be modified into a circular curve for the same reason.
- The other sets of physical changes such as the flux barrier shapes, air-gap length, and slot opening reduction can have some beneficial impact on the machine's performance.

In addition, more reliable metal cores for the stator and rotor laminations should be used as well. In the design steps of section 3.2, the lamination used for rotor and stator structures are selected from the standard lamination found in JMAG library. No limitations are applied to have low less density for the selected lamination. To solve this problem, lower loss density and thinner lamination, 29 gauge M19 (36X250), is used for the final model verification.

Furthermore, in the initial design presented by Fig 3.11 the ideal magnet found from JMAG-Designer library with 1.4T is used to do the simulations. However, in this part, the real magnet of NEOMAX-52, which has the B_r of 1.4T, is used.

To understand the impact of the design changes on the IPMSM's performance, five specific cases are chosen, taking into account the mentioned physical and material considerations.

Case 1: The initially designed IPMSM shown in Fig 3.11 plus removing the sharp edges in the stator structure and taking into account the material (magnet and cores) considerations; Case 2 is like Case 1 plus reduced slot opening from 4 mm to 2 mm; Case 3 is like Case 2 plus additional flux barrier between magnets; Case 4 is like Case 2 but with magnet pitch further reduced to 75%; and Case 5 is like Case 2 plus air-gap increased from 0.6 mm to 1 mm. The physical structures of these five different cases are shown in Fig 3.12.

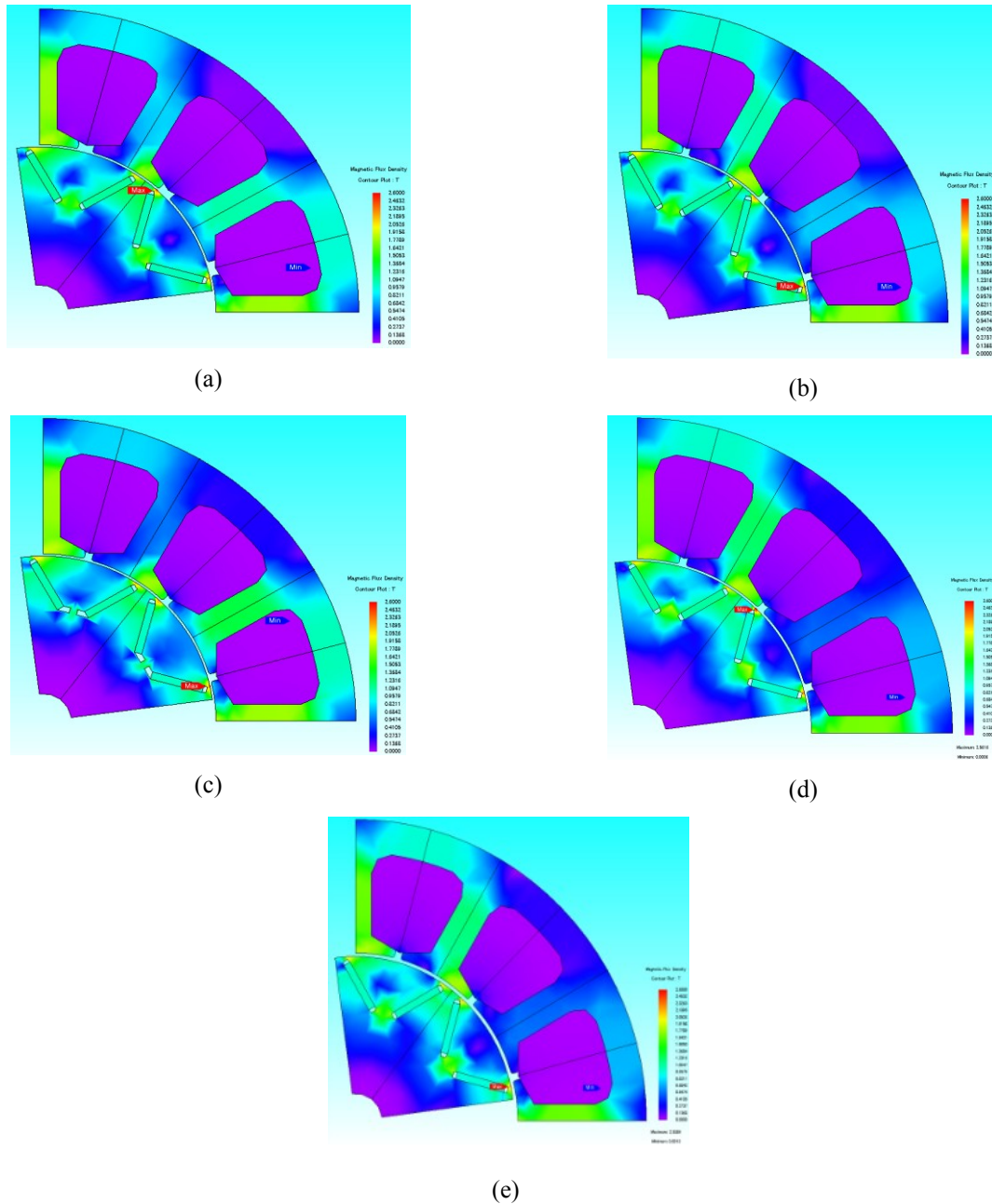


Fig 3.12 The physical structures and flux density plots in presence of different changes applied on the initial design, a) Case 1, b) Case 2, c) Case 3, d) Case 4, e) Case 5

In these five cases, the B_r of the magnet utilized in the machine structure is NEOMAX-52 which is very susceptible to demagnetize and usually more expensive than the weaker magnets [119]. The B-H curve versus temperature changes for NEOMAX-52 form JMAG-Designer library is shown in Fig 3.13.

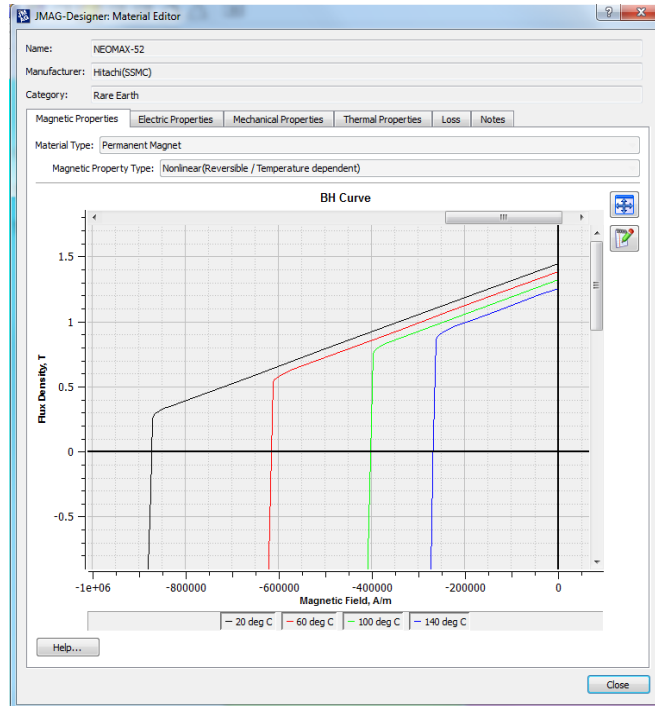


Fig 3.13 B-H curve versus temperature changes for NEOMAX-52

According to Fig 3.13, the B_r of NEOMAX-52 is the function of temperature changes. In high speed applications, the temperature of the rotor increases and results in lower magnetic flux density for the utilized magnet (demagnetization). Lower torque density and efficiency are seen in this situation.

Despite the high remnant flux density magnets, lower B_r magnets are demagnetized in higher temperatures and in more reverse magnetic field intensity. To solve the demagnetization problem of NEOMAX-52 magnet, using the lower B_r is considered as a useful method.

NEOMAX-35EH with $B_r=1.2T$ is used instead of NEOMAX-52. Although this magnet has lower B_r , its demagnetization trend is more reliable in the higher temperatures. In addition, NEOMAX-35EH belongs to the NdFeB magnet series and has the beneficial characteristics of this series of magnets. The B-H curve of NEOMAX-35EH is shown by Fig 3.14 for further clarity.

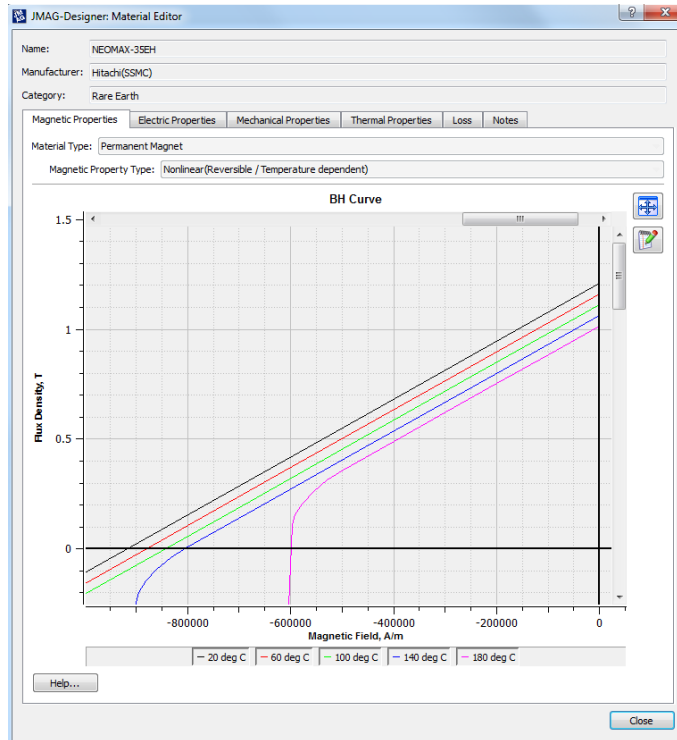


Fig 3.14 B-H curve versus temperature changes for NEOMAX-35EH

According to Fig, 3.14, NEOMAX-35EH has the B_r of almost 1.2 T and is demagnetized in 100°C while its reverse magnetic field intensity (coercivity H_c) is 2 times that of the NEOMAX-52 magnet. So, this type of magnet is considered more reliable, especially in higher speeds and higher temperature performances. Four different IPMSMs using NEOMAX-35EH magnet with fixed B_r of 1.2T and γ of 45° , 60° , 75° , and 90° , with wide clearance, and 85% Magnet Pitch (Mp) have been simulated for inductance evaluation prediction. The inductance evaluation is seen in Fig 3.15.

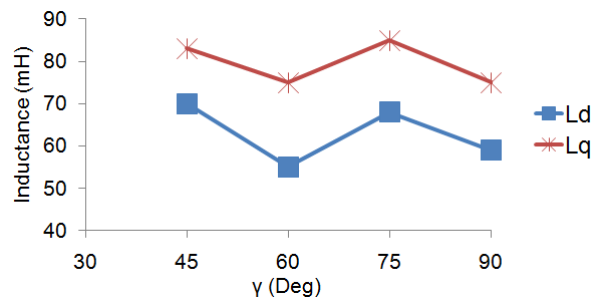


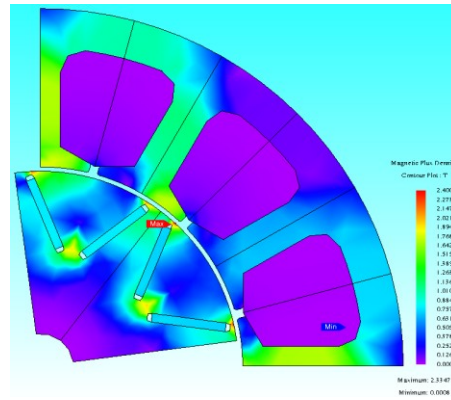
Fig 3.15 Inductance as the function of γ when there is a specific constraint on the utilized magnet flux density

The total volumes of the utilized magnets in cases shown in Fig 3.15 are collected in Table 3.4.

Table 3.4The total volume of the utilized magnets in different γ

γ (Degree)	Total Magnet Volume (mm ³)
45	35.84
60	32.8
75	27.2
90	26.24

As less amount of magnet is required for 75° γ case compared to 45° angle one, so 75° γ , an 85% magnet pitch and wide clearance IPMSM are selected as the sixth case for performance investigations. The physical structure of Case 6 is shown by Fig 3.16.

Fig 3.16 75° γ IPMSM using NEOMAX-35EH, case 6

3.4 Final Design

The final design of the IPMSM with widest speed range, lowest Back-EMF harmonic content, and lowest cogging torque is selected based on the performance evaluation carried out on the six cases presented in section 3.3. The field weakening method is used for finding the maximum speed capability of the machines in the constant power region. The mechanical losses, which include bearing losses, friction and windage losses, are neglected for verifying the maximum speed of the machines. On the other hand, when the angle and magnitude of the current flowing through the machine's phases change, the level of saturation in machine's phases is affected as well. This phenomenon causes the d-axis and q-axis inductances of the IPMSM to have dynamic behavior versus current changes [24]. Like the impacts seen on the Back-EMF harmonic contents, and cogging torque by the various changes applied to the rotor geometry presented in Section 3.3, it is expected that the Back-EMF and cogging torque of the machine are mainly

affected again by the new applied physical changes and modifications. Maximum speed range in constant power, L_d evaluation and saliency as $|L_d-L_q|$ in 4.5A current, Back-EMF THD comparison, and cogging torque comparison for the six cases introduced in the section 3.3 are shown by Fig 3.17.

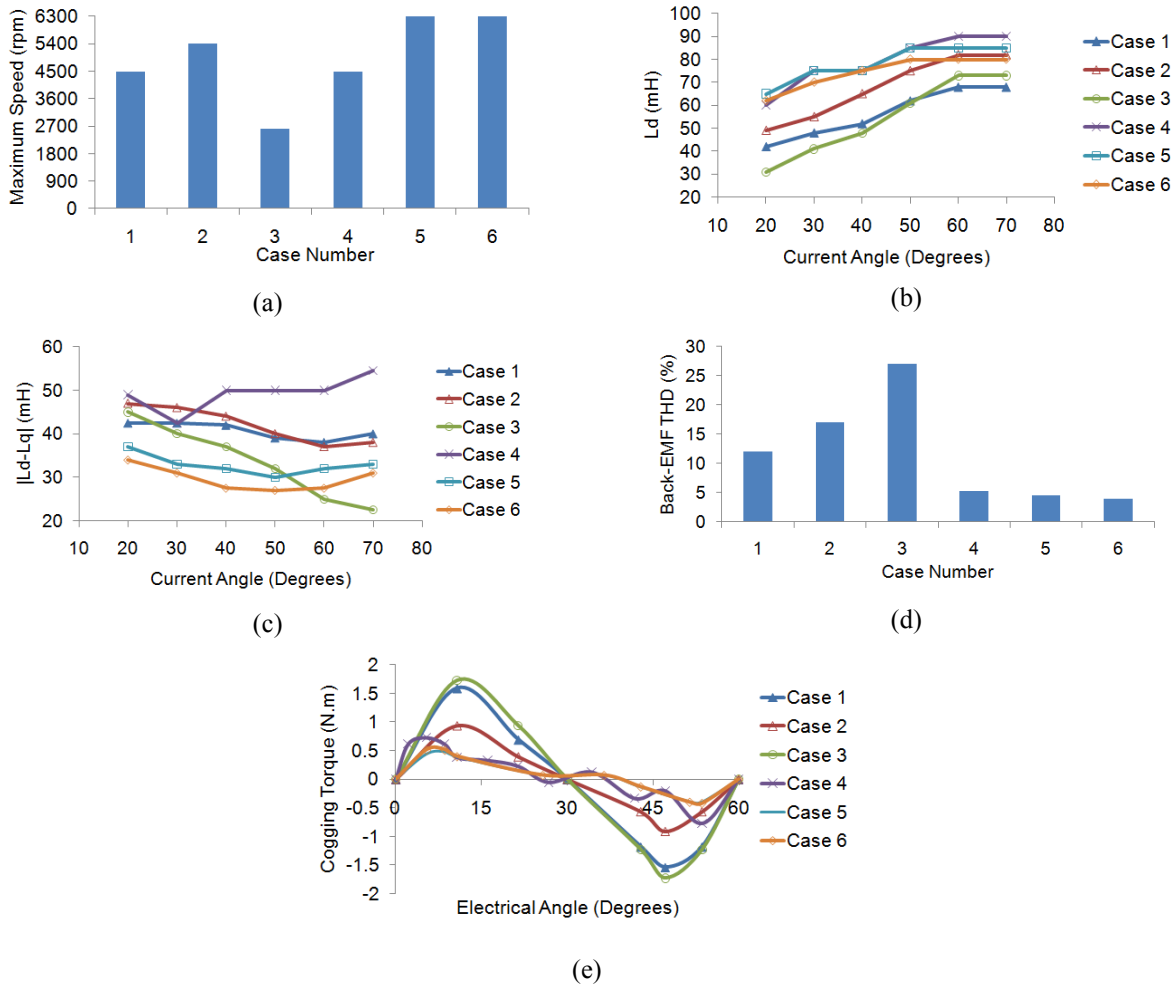


Fig 3.17 Comparison for the six cases a) Maximum speed, b) L_d , c) Saliency, d) Back-EMF THD, e) Cogging Torque

The main findings based on the comparison of the six cases are as follows:

The widest speed range, which is 6300 rpm, is seen for Case 5 and Case 6. Two low values of L_d are seen for cases 1 and 2. On the other hand, when the bridge is narrower in one structure, like Case 3, less L_d is expected due to the high reluctance of d-axis. A shorter field weakening region is expected for the cases having less L_d . In addition, the PM flux of Case 4 is low, but it has a higher d-axis inductance which may indicate a wide speed range. In Case 4, it appears that as the pole pitch has been reduced, and due to the low PM flux, the excitation torque will require excessive current to maintain the torque.

Regarding the THD evaluation in the Back-EMF waveform, it is pointed out that increasing the air gap by 0.4 mm and reducing the magnet pitch to 85% and 75% can filter some of the unwanted harmonics in the air gap flux waveform and reduce the THD value. Reducing the slot opening and making the iron bridge in the rotor smaller are not indicated as useful approaches in Back EMF harmonic content reduction. The minimum Back-EMF THD is seen for Cases 5, and 6.

According to the cogging torque analysis, increasing the air gap and reducing the slot opening cause the cogging torque of the machine to be minimized. On the other hand, having a smaller iron bridge in the rotor is not indicated as a promising method for cogging torque minimization. Accordingly, least cogging torque is seen for Cases 5 and 6.

By comparing the performance evaluation for all the six cases, Case 6 is selected as the final model with $75^\circ \gamma$, wide clearance, 85% magnet pitch, 1 mm air gap, and B_r of 1.2T (NEOMAX-35EH). The widest speed range, lowest cogging torque and lowest Back-EMF harmonic contents are predicted for Case 6.

The Back-EMF waveform and its harmonic spectrum, L_d and L_q variation versus current magnitude and angle for the final model (Case 6) are shown in Fig 3.18.

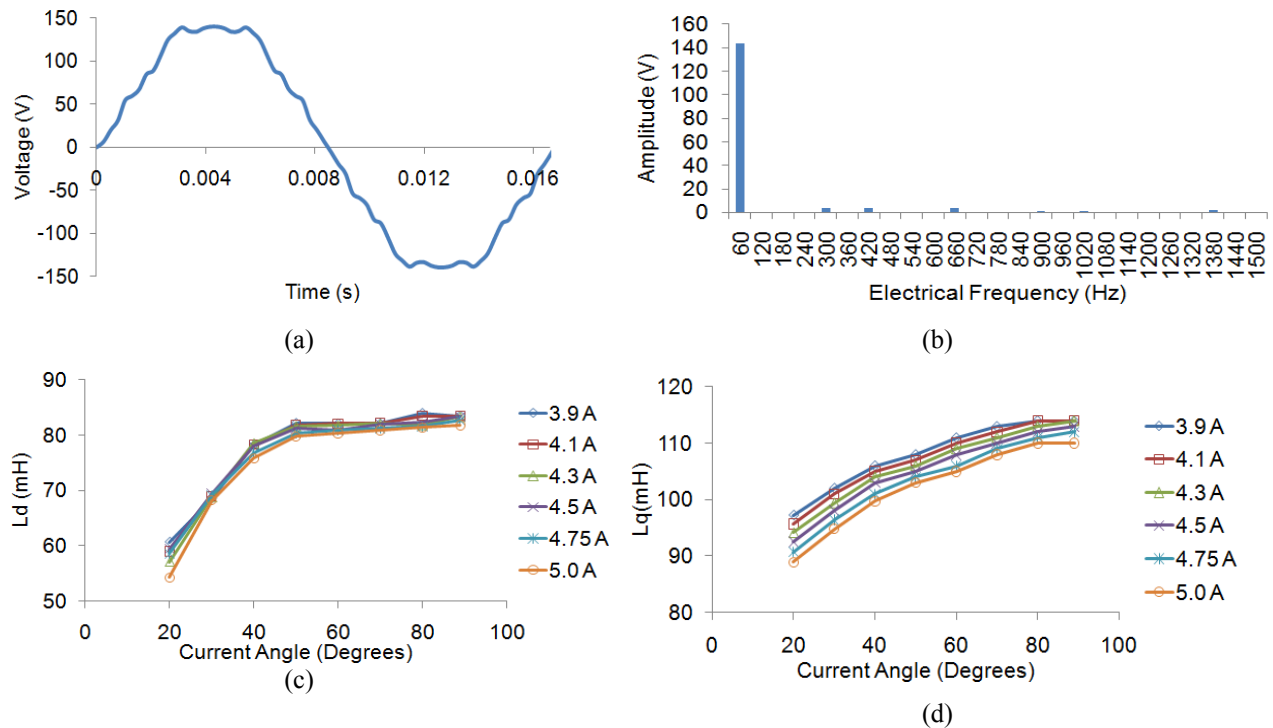


Fig 3.18 The final model a) Back-EMF waveform in 900 rpm, b) Back-EMF harmonic spectrum, c) L_d , and d) L_q

As the Fig 3.18 shows, the peak of 5th, 7th, and 11th harmonics in Back-EMF is not high in the final model which causes its THD to be even less than 3%. In addition, big L_d and L_q inductances are predicted by simulation which causes the machine to have wide speed range and torque density. Furthermore, L_d is more affected by current angle than L_q which concludes the dynamic saliency of the machine in the wide speed region of performance. In higher speeds and when the current angle is larger, more L_d is expected; therefore, the characteristic current of the machine gets smaller while less saliency is expected in the larger current angles.

3.5 Loss and Efficiency Analysis

The electrical loss analysis for the final design of the IPMSM (Case 6) is presented using FEM. The mechanical loss is ignored in the simulation but is included in the experiment.

The main electrical losses, including copper loss and iron loss, are used to predict the efficiency of the designed IPMSM. Using the loss assessment, the efficiency of the machine can be predicted by equation (3.19).

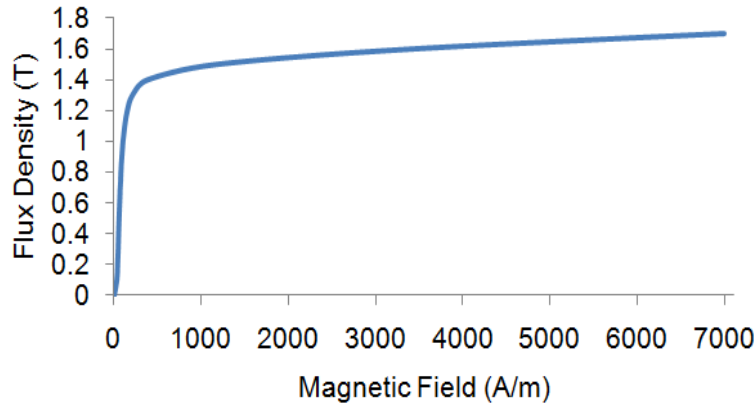
$$\eta = \frac{P_{out}}{P_{out} + P_{Iron\ Loss} + P_{Copper\ Loss} + P_{Friction\ \&Windage}} \quad (3.19)$$

AK Steel, 29 gauge, M19 lamination is used for the rotor and stator lamination of the final design. The thickness of this lamination is 0.036 mm and its loss density is 2.5 W/kg in 50Hz of supply frequency and 1.5T magnetic flux density.

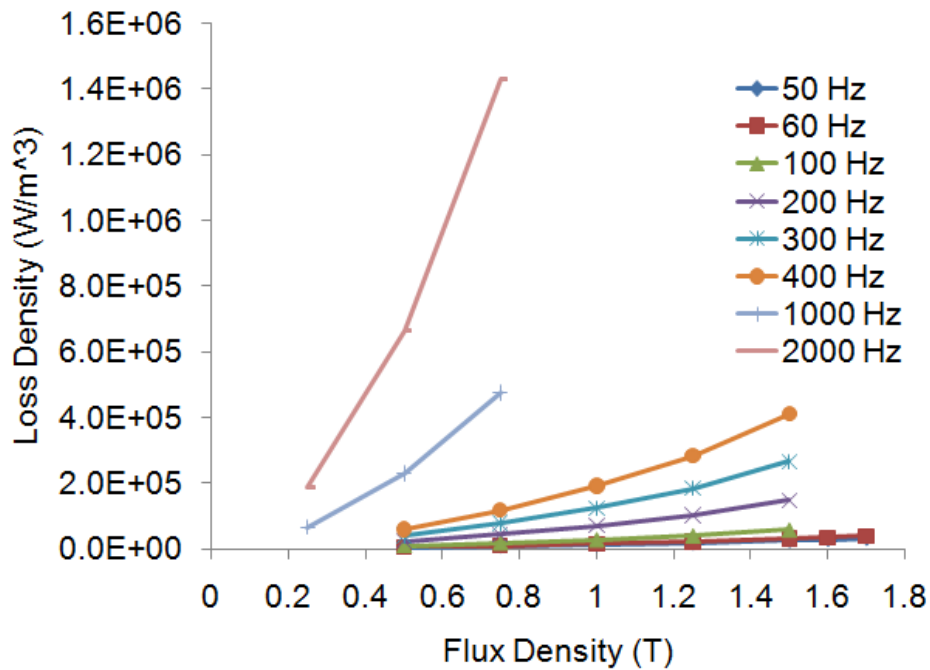
The M19 lamination B-H curve and loss density profile, which is defined as a new material in the JMAG-Designer library, are shown in Fig 3.19.

The B-H curve presented by Fig 3.19 shows that when the magnetic field intensity increases, the flux densities increase, saturating after the knee point. For M19 lamination, the maximum flux density is 1.7 T with a field intensity of 7100 A/m.

The loss density rapidly enhances in lower applied flux density when the applied frequency is increasing. That shows larger iron loss in higher speed applications.



(a)



(b)

Fig 3.19 a) B-H curve, and b) Loss density variations for M19 lamination

The copper loss, iron loss, including hysteresis loss and eddy current loss, for the final design using M19 lamination in the machine's structure are shown by Fig 3.20. The loss evaluation is presented from base speed (900 rpm) to the maximum possible speed of 6300 rpm. The current change profile, the magnet loss and power-torque versus speed taking into account the friction and windage (F&W) losses for the finally designed IPMSM with M19 lamination are shown in Fig 3.21.

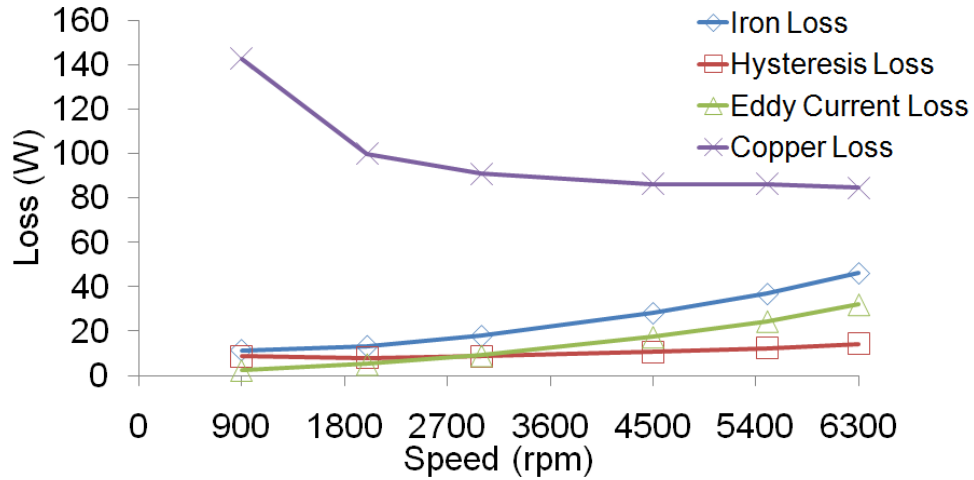


Fig 3.20 Copper loss, iron loss, eddy current loss and hysteresis loss evaluation, for the designed IPMSM using 29 gauge M19 lamination

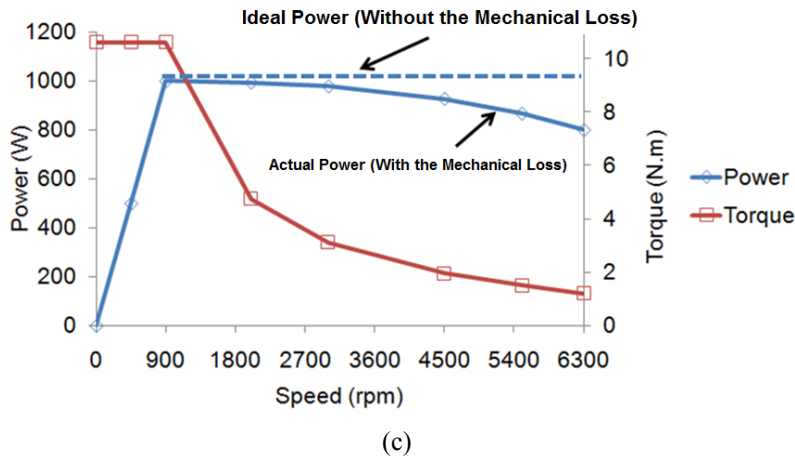
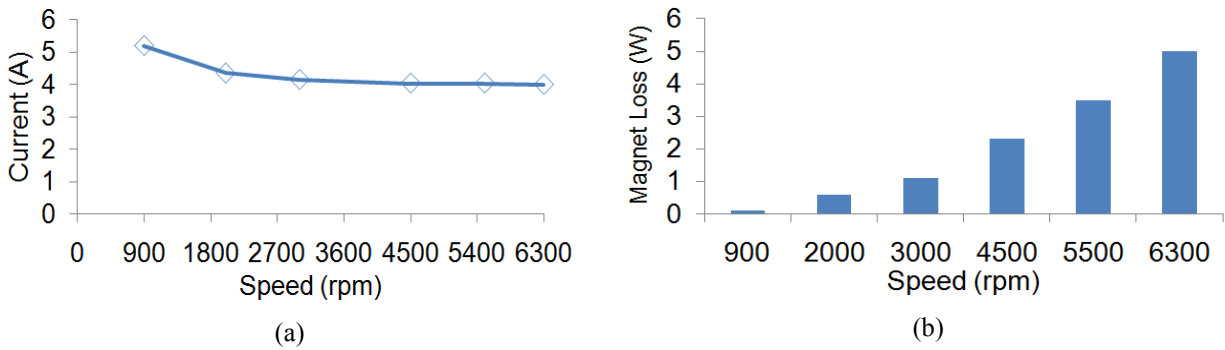


Fig 3.21 a) Current profile b) Magnet loss c) Power-Torque versus speed profile taking into account the mechanical loss including friction and windage (F&W), for the designed IPMSM using M19 core

The significant contribution of eddy current loss in the total iron loss is clearly seen in Fig 3.20. The iron loss, eddy current loss, and hysteresis loss values are all functions of supply frequency, and their values are increased in higher speed applications.

Copper loss in higher speeds is smaller than in lower speeds (See Fig 3.20). This is due to the reduction of the required current in higher speeds. As is shown in Fig 3.21(a), when the machine is working in higher speeds, smaller current is required to fulfill the rated power for the designed IPMSM. This is because of the increment of the machine's L_d and L_q inductances which are shown by Fig 3.18(c), and 3.18(d), and also due to less required torque in the high speed region.

The copper loss of the machine varies between 142W to 92W in the wide speed range, and the eddy current loss is between 11W to 46W from base speed to seven times base speed. It is worth noting that the frequency-dependent copper loss changes have been neglected.

According to Fig 3.21(b), the magnet loss is less than 6W and is not high enough to affect the total efficiency significantly. In addition, if the mechanical loss including friction and windage loss, is taken into account, even a 200W reduction in output power is observed at high speeds (See Fig 3.21(c)). Using equation (3.19) and the evaluated losses, the efficiency profile in the wide speed range for the designed IPMSM using the M19 lamination is shown by Fig 3.22. Mechanical losses have been neglected in the efficiency analysis.

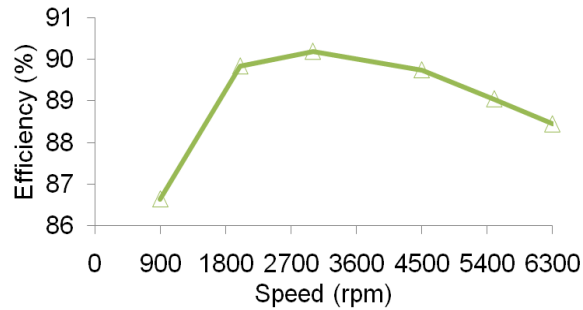
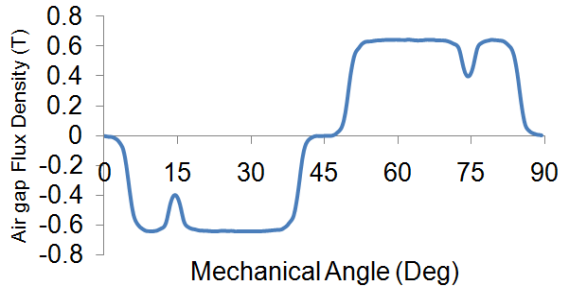


Fig 3.22 Efficiency analysis for the designed IPMSM

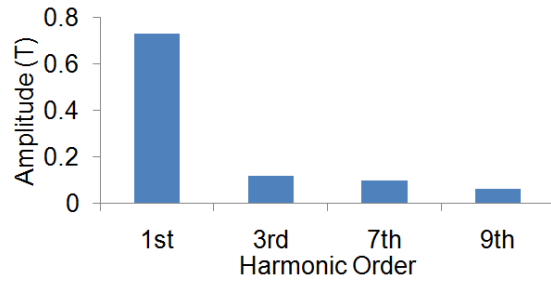
The efficiency between 86.5% and 90.2% is predicted by the FEM analysis in the wide speed range operation of the designed IPMSM.

3.5.1 Harmonic Iron Losses

As is shown in the iron loss analysis, iron loss is more greatly affected by eddy current loss variations, especially in higher speeds. So, if the eddy current loss is correctly interpreted, iron loss can be better explained. According to the eddy current loss equation introduced by equation (2.20) in Chapter 2, this loss is affected by air-gap flux density variations and its harmonics. As is shown by Fig 3.23, air-gap flux density is not pure sinusoidal waveform and has some harmonics, resulting in harmonic iron losses for the designed IPMSM.



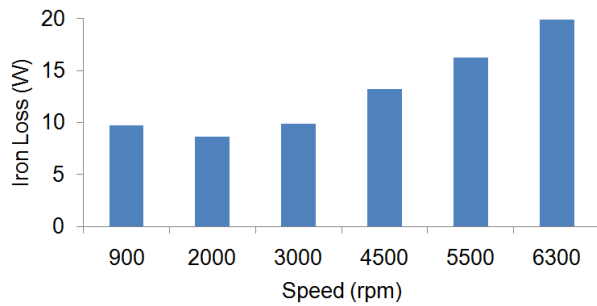
(a)



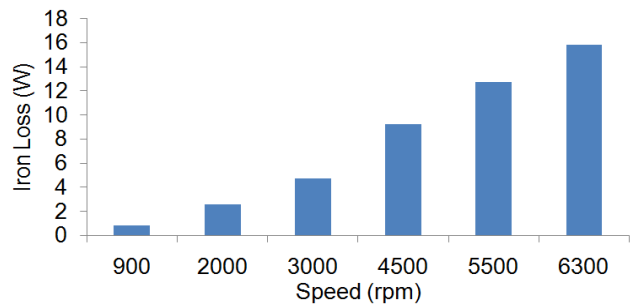
(b)

Fig 3.23 Designed IPMSM's a) Air gap flux density, b) Harmonic analysis for the air gap flux density in 900 rpm

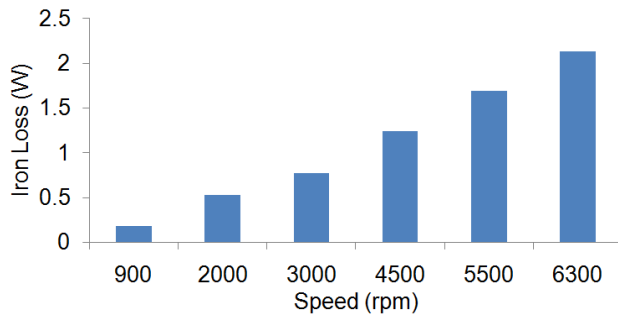
Fast Fourier Transform (FFT) analysis has been utilized to predict the iron loss of the designed IPMSM using 29 gauge M19 lamination in different harmonics (See Fig 3.24).



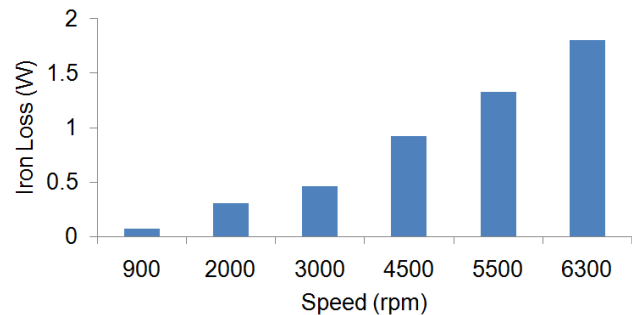
(a)



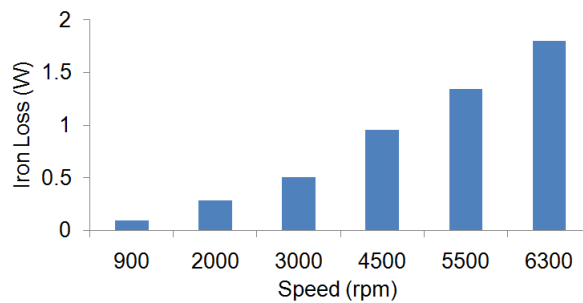
(b)



(c)



(d)



(e)

Fig 3.24 Harmonic iron losses for the designed IPMSM, a) 1st harmonic, b) 3rd harmonic, c) 5th harmonic, d) 7th harmonic, e) 9th harmonic

The summary of harmonic iron loss is described as follows:

By increasing the machine's speed, iron loss increases for all harmonics.

The highest iron loss is seen in fundamental and third harmonics for all speeds.

Fundamental harmonic iron loss is minimal at 2000 rpm speed.

Iron loss analysis versus harmonic order in base speed and maximum speed for the designed IPMSM using M19 lamination is shown in Fig 3.25.

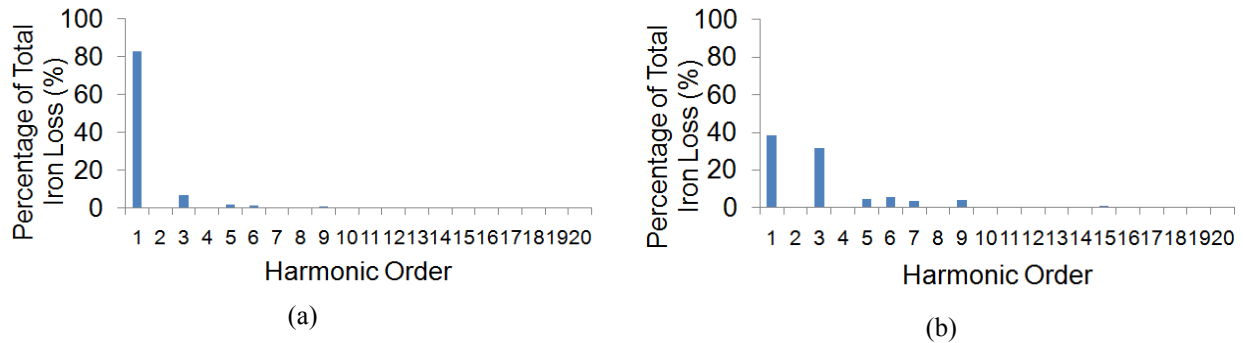


Fig 3.25 Percentage of total iron loss for each harmonic in a) Base speed (900 rpm), b) Maximum speed (6300 rpm)

An 85% contribution to the total iron loss is seen for the fundamental harmonic of the machine at base speed, while the third harmonic only has less than 7% contribution. No major contribution is observed in other harmonics.

At maximum speed, fundamental and third harmonics have the highest contributions to the total iron loss. Fundamental harmonic contribution is 41%, and third harmonic contribution is 30%.

3.6 Summary

The influence of geometry changes on motor performance is investigated. In order to fulfill the aim of a machine with a wide speed range, high efficiency and low parasitic harmonic effects, a parametric design of experiments approach is conducted to improve the operational characteristic and specify the circuit parameters of the IPMSM in each step. It has been attempted to change the motor's physical variables in each step in a way to increase the inductance especially d-axis inductance, reduce the cogging torque and reduce the Back-EMF harmonic content for the final model. Although the final model is not optimized, but the most important operational characteristics and circuit parameters of the model have been investigated

to be improved at a same time during the design of experiment procedure while some compromises are taken into account if needed.

A 12 slot-8 pole IPMSM is chosen as a suitable candidate for high torque density performance based on the winding factor and MMF assessment. This slot pole combination maximizes the MMF and winding factor multiplication. The analytical calculation based on the magnetic and electrical loading is carried out to introduce the initial dimensions of the machine to offer a model with 1kW power in rated speed of 900 rpm and in 320VDC.

The parametric design of experiments procedure is conducted and the impact of rotor geometry changes, including γ changes, magnet pitch changes, and changing the clearance between two adjacent pieces of magnet, are investigated. Rotor geometry changes are mainly employed to adjust the level of magnetization and reluctance in each axis for the inductance justification and tuning the harmonic content of air-gap flux density profile. As a result of this analysis, a design with $\gamma= 90^\circ$, wide clearance, 85% magnet pitch is introduced as the initial model IPMSM. The initial model provides the high d-axis inductance (60 mH), low Back-EMF harmonic content (less than 6% THD) and low peak cogging torque (less than 7%). Increasing the magnet pitch enhances the harmonic content of the Back-EMF voltage. On the other hand, increasing the clearance between two adjacent magnets in each pole increases the d-axis inductance value as the d-axis path is not saturated compared to the narrower clearance case.

Further physical and material modifications are applied to the structure of the initially designed IPMSM to finalize a reliable model with lower cogging torque and Back-EMF harmonic content. The simulations predict a wide range speed of 6300 rpm, 3% Back-EMF THD, and less than 5% cogging torque peak for the finally designed IPMSM.

Electrical loss analysis is presented using FEM, and efficiency between 86.5% and 91% in the wide speed range is predicted by simulation analysis for the final design. In the efficiency prediction, the mechanical losses have been neglected.

The main contributions of this chapter are to illustrate the relationships between geometry, circuit parameters and overall performance; and to introduce a reliable design with wide range speed operation and promising efficiency.

Chapter 4

DUAL INVERTER ANALYSIS

A basic explanation and vector diagram for the dual inverter open winding PMSM is discussed. This discussion gives a clear view of how a controller can be defined. The controller performance is examined by simulation results in Matlab/Simulink. A 41% extension in maximum speed of the designed IPMSM is illustrated by FEM analysis when the machine is employed in open winding structure using an ideal dual inverter drive. Loss analysis and efficiency assessment for this configuration are included for wide speed range operation.

The Simulink simulations are conducted by Matlab R2011b using the SimPower Systems toolbox. The utilized converters are modeled as three phase average-value model VSCs which receive the three phase sinusoidal waveforms as the gating signals. The Space Vector Modulation (SVM) is assumed for the machine's control purposes; therefore the peak of the gating signals to the VSCs can be 1.15 at most. The conventional abc to d-q transformation is used for defining the voltages and currents to control the machines performance in wide range of speeds and various operating points. During the open winding FEM simulation analysis, the neutral point of the Y-connected FEM coils is removed and this terminal is connected to the second controllable voltage source supply which models the terminals of the Floating Bridge (FB). The phases of the voltage provided by the voltage source are defined to be perpendicular to the current source that represents the MB side. The other details about FEM analysis are similar to that of Chapter 3.

An initial control approach is introduced and simulated based on the vector diagram and basic definition of an open winding PMSM using dual inverter drive structure. The dual inverter drive uses a controlled voltage floating capacitor on the FB side.

Although the explanations and vector diagram are shown using the case of an SPMSM, this is done merely to present a simple example to understand. The approach, however, can be extended to an IPMSM as well. In the equation below, the non-salient structure of an SPMSM gives the following developed torque [120]:

$$T_e = \frac{3}{2} \left(\frac{p}{2} \right) (\lambda_{pm} i_q) \quad (4.1)$$

Equation (4.1) demonstrates that the electric torque is only tuned by q-axis current, flux linkage of permanent magnet and the number of the machine's poles.

In a steady state condition, the steady state d-axis and q-axis components for the machine's terminal voltage are formulized by the following equations:

$$v_{qm} = R_s i_q + \omega_e \lambda_{pm} + \omega_e L_d i_d \quad (4.2)$$

$$v_{dm} = R_s i_d - \omega_e L_q i_q \quad (4.3)$$

The main aim of using an SPMSM in an open winding structure is to enable the machine to receive two separate voltages from two sources at the same time. This causes the machine to have an extended operating region by increasing the phase voltage.

The conceptual vector diagram of the studied open winding PMSM using a dual inverter drive and its simplified circuit are shown by Fig 4.1.

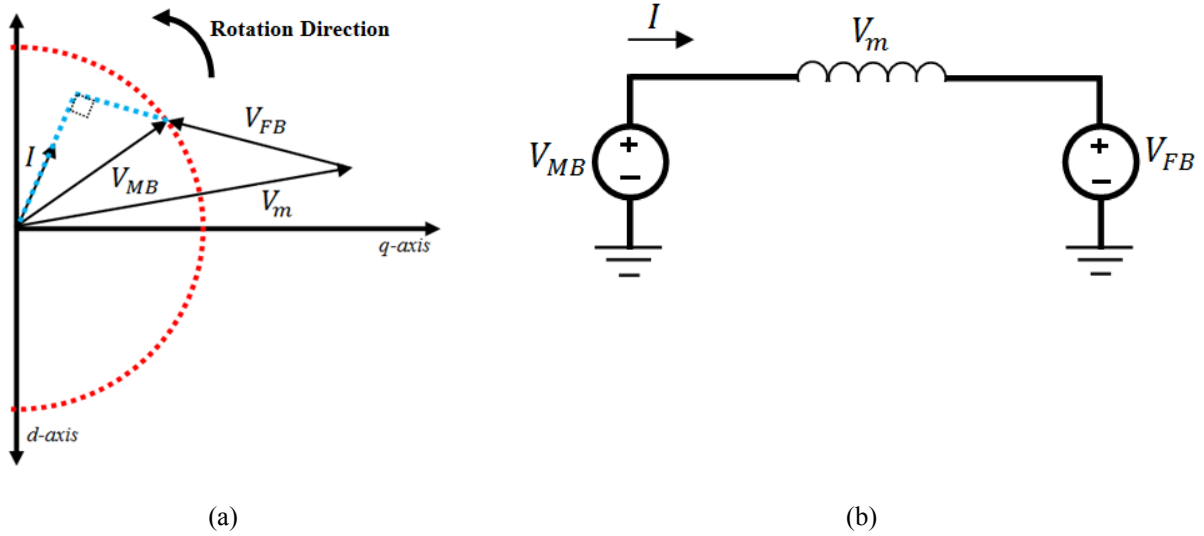


Fig 4.1 a) Conceptual vector diagram and b) Circuitry of the dual inverter scheme

The vector diagram is based on equation (4.4).

$$\overrightarrow{V_{MB}} = \overrightarrow{V_m} + \overrightarrow{V_{FB}} \quad (4.4)$$

The current flowing through the winding must be perpendicular to the FB voltage. So,

$$\frac{V_{FBq}}{V_{FBd}} = -\frac{i_d}{i_q} \quad (4.5)$$

Briefly, three regions should be considered to fulfill the requirements of dual inverter open winding PMSM in the wide speed range. Before base speed, d-axis current is not required for tuning the speed. Above base speed, the FW control should be employed. In this range, i_d is no longer zero, and i_q is decreasing to may be keep the rated power. For this area, the machine's terminal voltage is always kept to its nominal value (1 per-unit). The final region is when the machine reaches its maximum speed. In this situation, the FB's contribution is employed, and an increased voltage may be applied to the machine's terminal. In this introduced region, the machine's terminal voltage vector is increasing from 1 per unit to 1.41 per unit while still giving the rated power. A 1.41 per-unit voltage on the machine's terminal is seen in the case that both MB voltage vector and FB voltage vector have the same magnitudes and are perpendicular to each other. In the control method, the FB voltage magnitude and angle are forced to be set in a way that FB is always perpendicular to the current.

In order to fully understand the FB's contribution in widening the operating region, Fig 4.2 is presented. As is seen by the conceptual vector diagram, the FB is capable of injecting or absorbing reactive power according to the operating point of the machine.

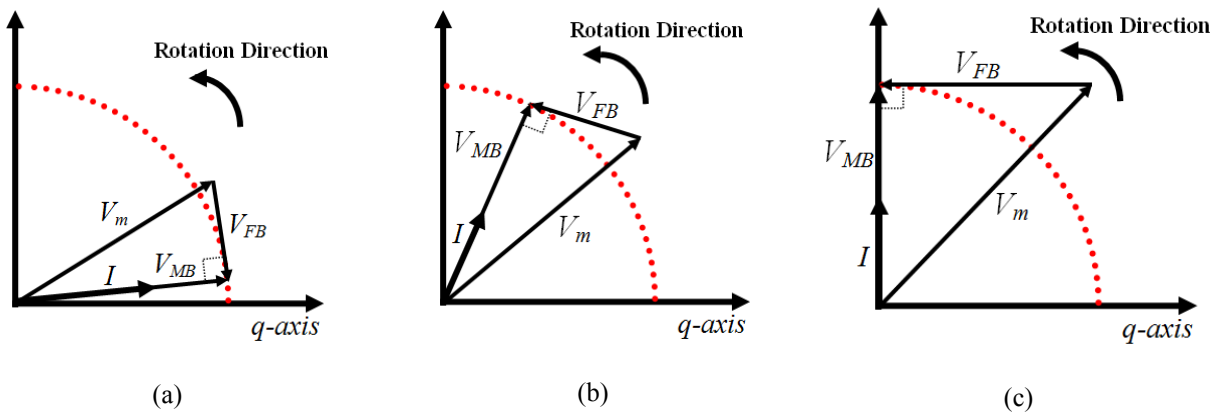


Fig 4.2 Dual inverter drive conceptual voltage vector diagram, a) In 1.1 times machine's rated voltage (lagging power factor), b) In 1.2 times machine's rated voltage (leading power factor), c) In 1.41 times machine's rated voltage (leading power factor)

Assuming that the demand torque and speed are within the limits of the system, the control of the motor may be broken down into four different stages. In the first stage, the rotor position should be detected using the derivation of the machine's speed over time changes. The rotor position can be determined by an encoder in experiments. This rotor position can be used to transfer d-q voltage and current components to abc frame and vice versa in the three-phase

system. The second stage is the identification of the machine's operation mode. This means that, in some speeds, the machine is working using only the MB, and in some other speeds, FB and its related controller should be added. In the third stage, the MB and FB voltages should be precisely defined by the studied controller in order to supply the machine's terminal voltage and take into account the perpendicularity of the FB and the machine's current. For the fourth and final stage, in the introduced controller, one PI controller is used to control the capacitor voltage on the FB side by tuning the real power flow in machine's windings.

For implementing the controller, the mathematical relationship of d-q axis voltages for the machine, the MB and FB are given by equations (4.6) and (4.7).

$$v_{q1} = v_{qm} + v_{q2} \quad (4.6)$$

$$v_{d1} = v_{dm} + v_{d2} \quad (4.7)$$

Indices 1 and 2 represent the MB and FB's components, and m shows the motor's component.

The required reactive power of the machine is given by equation (4.8).

$$Q = \frac{3}{2}(v_{qm} i_d - v_{dm} i_q) \quad (4.8)$$

Using equations (4.5) and (4.8), the d-q axis voltage components of FB calculated by reactive power transfer can be formulized as described in equations (4.9) and (4.10).

$$v_{d2Q} = -\frac{Q}{\frac{2}{3}(i_q + \frac{i_d^2}{i_q})} \quad (4.9)$$

$$v_{q2Q} = -\frac{i_d}{i_q} \cdot v_{d2Q} \quad (4.10)$$

The FB real power flow (called P_2 in this chapter) is controlled to adjust the bridge's capacitor voltage using an error signal and a PI controller. The capacitor voltage PI controller in Laplace domain is shown by equation (4.11).

$$P_2 = \left(k_p + \frac{k_i}{s}\right)(V_{Cap-ref} - V_{Cap}) \quad (4.11)$$

The FB capacitor voltage component regulation represented by P_2 is considered for real power injection into the bridge, so this voltage component must be in phase with the motor current. This characteristic is described by equation (4.12).

$$\frac{v_{q2P}}{v_{d2P}} = \frac{i_q}{i_d} \quad (4.12)$$

Consequently, FB's d-q voltage components calculated by real power flow are described by equations (4.13) and (4.14).

$$v_{q2P} = \frac{P_2}{\frac{2}{3}(i_q + \frac{i_d^2}{i_q})} \quad (4.13)$$

$$v_{d2P} = \frac{i_d}{i_q} \cdot v_{q2P} \quad (4.14)$$

Using superposition theorem, the d- and q-axis voltage components for FB are given by equations (4.15) and (4.16).

$$v_{q2} = v_{q2P} + v_{q2Q} \quad (4.15)$$

$$v_{d2} = v_{d2P} + v_{d2Q} \quad (4.16)$$

The d-q voltage components for the machine's terminal are obtained from speed and d-axis current controllers. So, the MB's d-q axis voltages can be calculated using equations (4.15), (4.16), (4.6), and (4.7).

As the FB is the component of the drive responsible for the reactive power required by machine, and it is always set to be perpendicular to the current, so the MB voltage components are adjusted by the controller in a way that supports the real power required by the machine. In the introduced controller, the MB voltage and the machine's current are aligned, causing the terminal voltage of the machine and its maximum speed range to be extended by 41% when two MB and FB have the same ratings. In this situation, the output voltages of both MB and FB are 1 per-unit.

The block diagram for the introduced controller is shown by Fig 4.3.

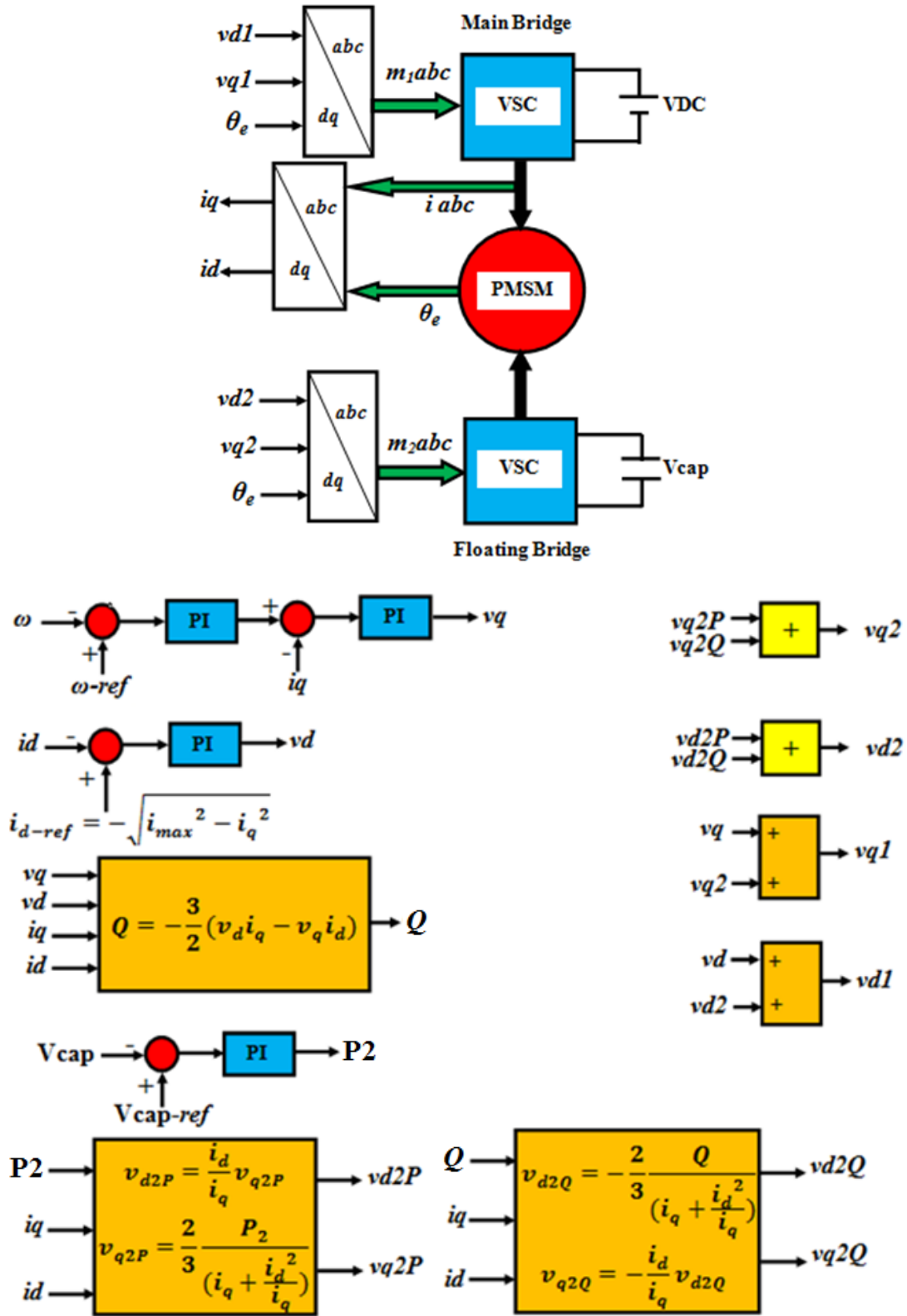


Fig 4.3 Dual inverter open winding PMSM controller block diagram for the maximum speed to 1.41 times maximum speed region, rated power is fulfilled

4.1 Drive Simulation

The concept of a dual inverter drive structure for feeding the open winding PMSM has been briefly introduced and a suitable controller for extending the operating region is developed. In order to examine the applicability of the introduced controller, some simulation analyses are presented in this section. The machine specifications are based on an SPMSM built by Baldor Company which can be found in the datasheet uploaded in its website. The type of machine is a BSM90N-275AA eight pole SPMSM. The machine's specifications and the utilized drive are collected in Table 4.1.

Table 4.1
Specifications of BSM90N-275AA PMSM and the utilized drive

Parameter	Value	Parameter	Value
Maximum Cont. Stall Torque Lb-In (N-m)	88.00 (10.00)	Poles	8
Voltage Constant $V_{pk}/KRPM$ ($V_{RMS}/KRPM$)	81.5 (57.65)	Type of magnet	NdFeB
Resistance (Ω)	0.52	Type of machine	SPMSM
Inductance (mH)	0.66	Main bridge DC link (V)	160
Inertia Lb-In-s ² (Kg-cm ²)	0.0056 (6.3224)	Floating bridge capacitor voltage (V)	160
Base speed at 160 Bus Volts RPM (rad/s)	1785 (186.92)	Maximum modulation index (SVM)	1.15

Before going through the simulation results, the Simulink configuration used to model the open winding PMSM drive is shown by Fig 4.4 and Fig 4.5.

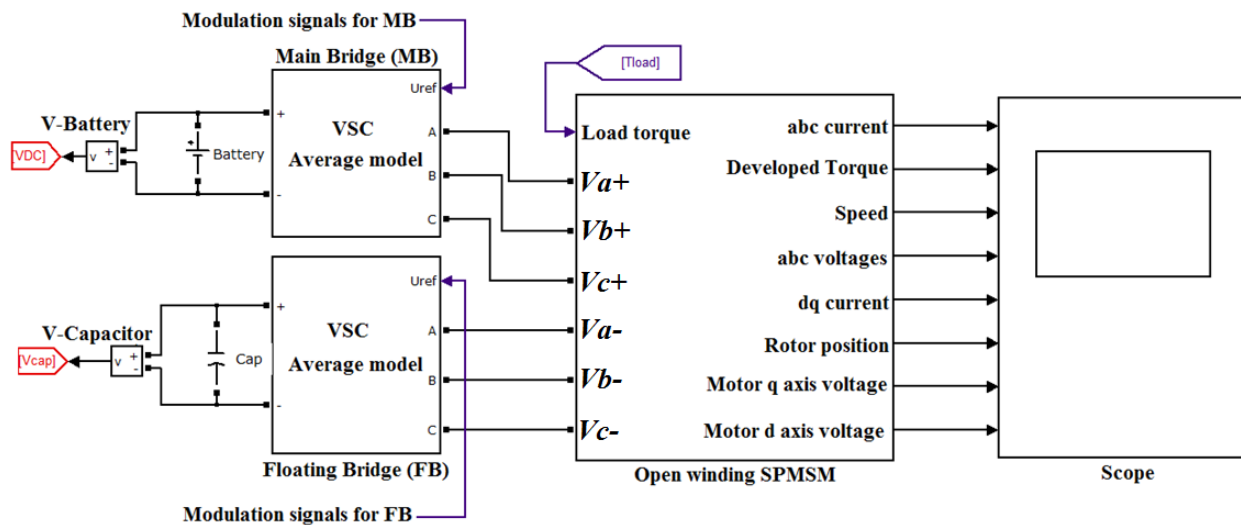


Fig 4.4 The open winding SPMSM fed by two VSCs in Simulink space

Fig 4.5 shows how the open winding SPMSM block is modeled.

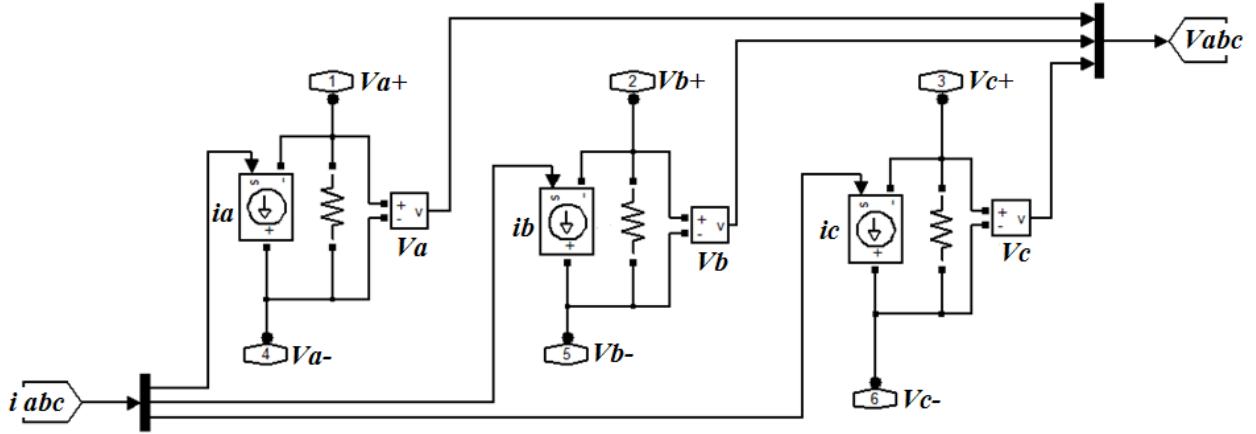


Fig 4.5 The open winding SPMSM modeled in Simulink

The general configuration depicted by Fig 4.4 and the modeling of open winding PMSM shown in Fig 4.5 merit closer consideration.

In Fig 4.4, the MB and FB are modeled by two average model VSCs found in Simulink power system library.

As is shown in the controller algorithm, the controller sets the V_{q1} , V_{d1} , V_{q2} , and V_{d2} , as the MB and FB voltage components using a series of maths and capacitor voltage control. These d- and q-axis voltages are transferred to the abc reference frame by Park Transformation. The output abc voltages are used as the modulation signals and are applied to the average model of VSC seen in Fig 4.4. Since SVM is used in this study, the peak of modulation signals should not exceed 1.15 at all.

Each phase of the open winding PMSM is modeled by a current source in order to enable the controller to adjust the current flowing through the phases. A big resistor is used in each phase and the MB and FB voltages are supplied across the resistor. V_{a+} , V_{b+} , and V_{c+} are for the MB side voltages, and V_{a-} , V_{b-} , and V_{c-} are for the FB side voltages. Three voltage measurement units are used to monitor the voltage across the phases of the open winding PMSM (V_a , V_b , and V_c).

The modeled machine has relatively low inductance (0.66 mH, 0.08 pu) as is seen in Table 4.1, so unfortunately, it does not show a wide range speed operation. The modeled machine is able to support the rated power only until 1.13 times base speed (210.18 rad/s) in a single

inverter drive and using FW control. If the machine is used in a dual inverter drive structure, the maximum speed in rated power is extended to $210.18 \times \sqrt{2} = 297 \text{ rad/s}$.

The following simulation results (Fig 4.6 - Fig 4.8) show the capacitor voltage control performance, machine's speed control, and the MB and FB modulating signals assessment below maximum speed (210.18 rad/s), i.e. 150 rad/s with having only MB activated for control, above maximum speed in rated power, i.e. 250 rad/s with having both MB and FB, and a higher speed that rated power is no longer available, i.e. 425 rad/s.

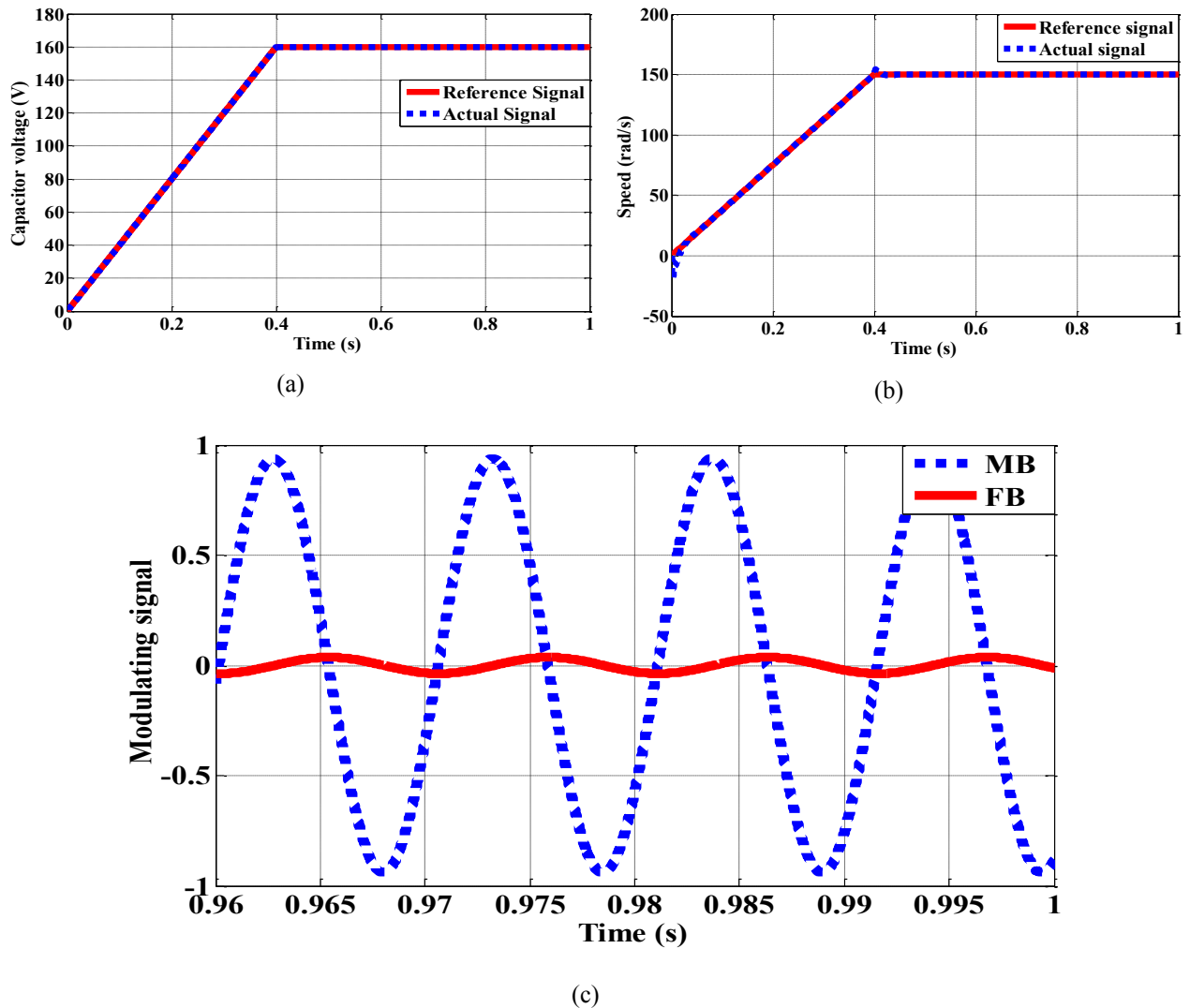


Fig 4.6 a) Capacitor voltage control, b) Speed control, c) Modulating signals assessment in 150 rad/s

These figures show an acceptable control performance using the introduced controller. Since the machine is working below base speed, there is no need to activate the FB to provide more

voltage on the machine's phases. The very low modulating signal for FB confirms this claim. However, there is a low amplitude modulating signal for FB in order to control the capacitor voltage and keep it on the desired value.

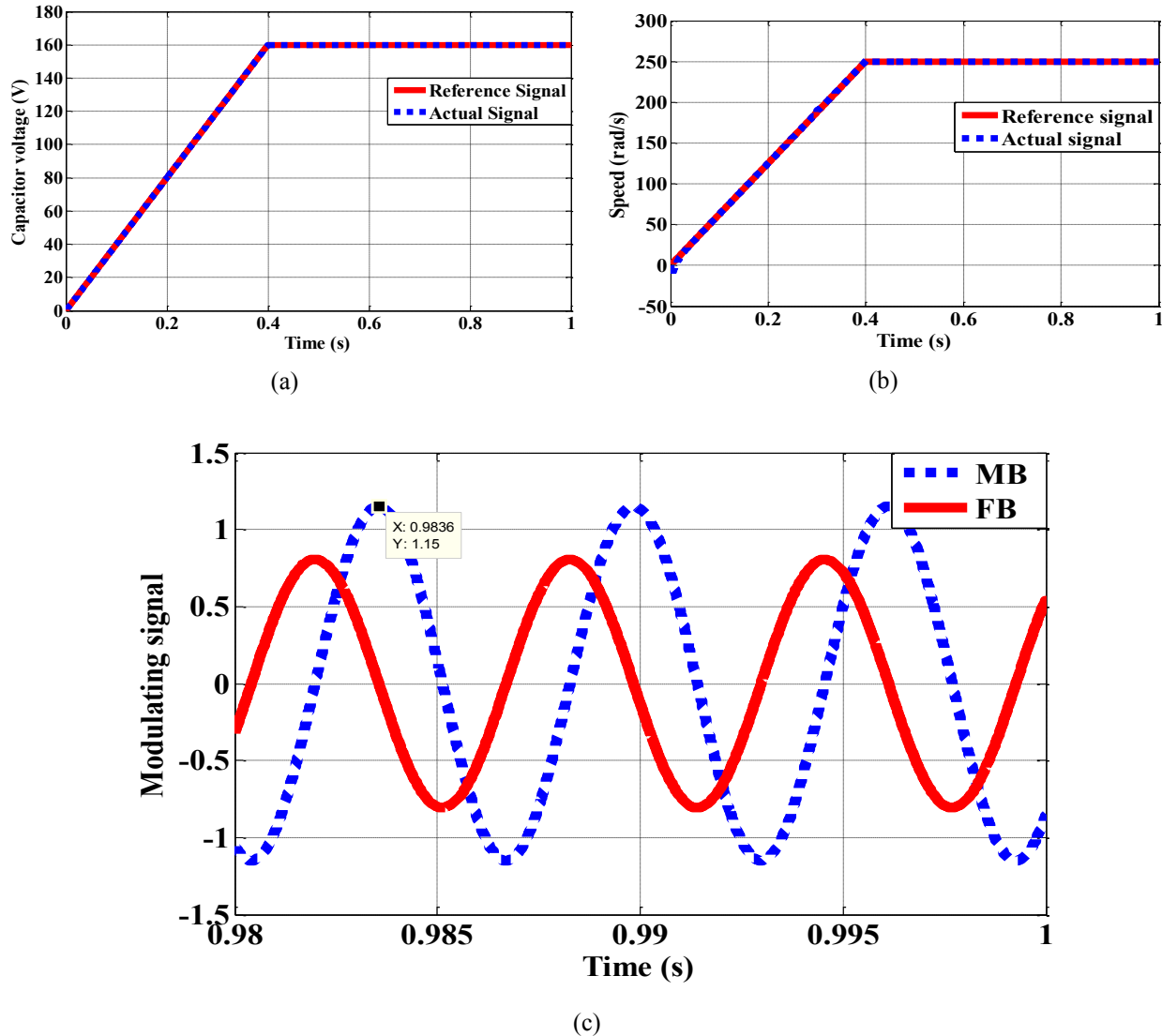


Fig 4.7 a) Capacitor voltage control, b) Speed control, c) Modulating signals assessment in 250 rad/s

According to Fig 4.7, when the machine is working above its maximum speed (210.18 rad/s), both bridges are utilized to supply the machine's terminal voltage in the rated power. In addition, it can be seen that the voltages of the two bridges are perpendicular, which verifies the vector diagram explanations. Another finding shows that the MB voltage modulating signal is set to 1.15, which is its maximum value, while the FB modulating signal varies from low values to 1.15, depending on the machine's operating point.

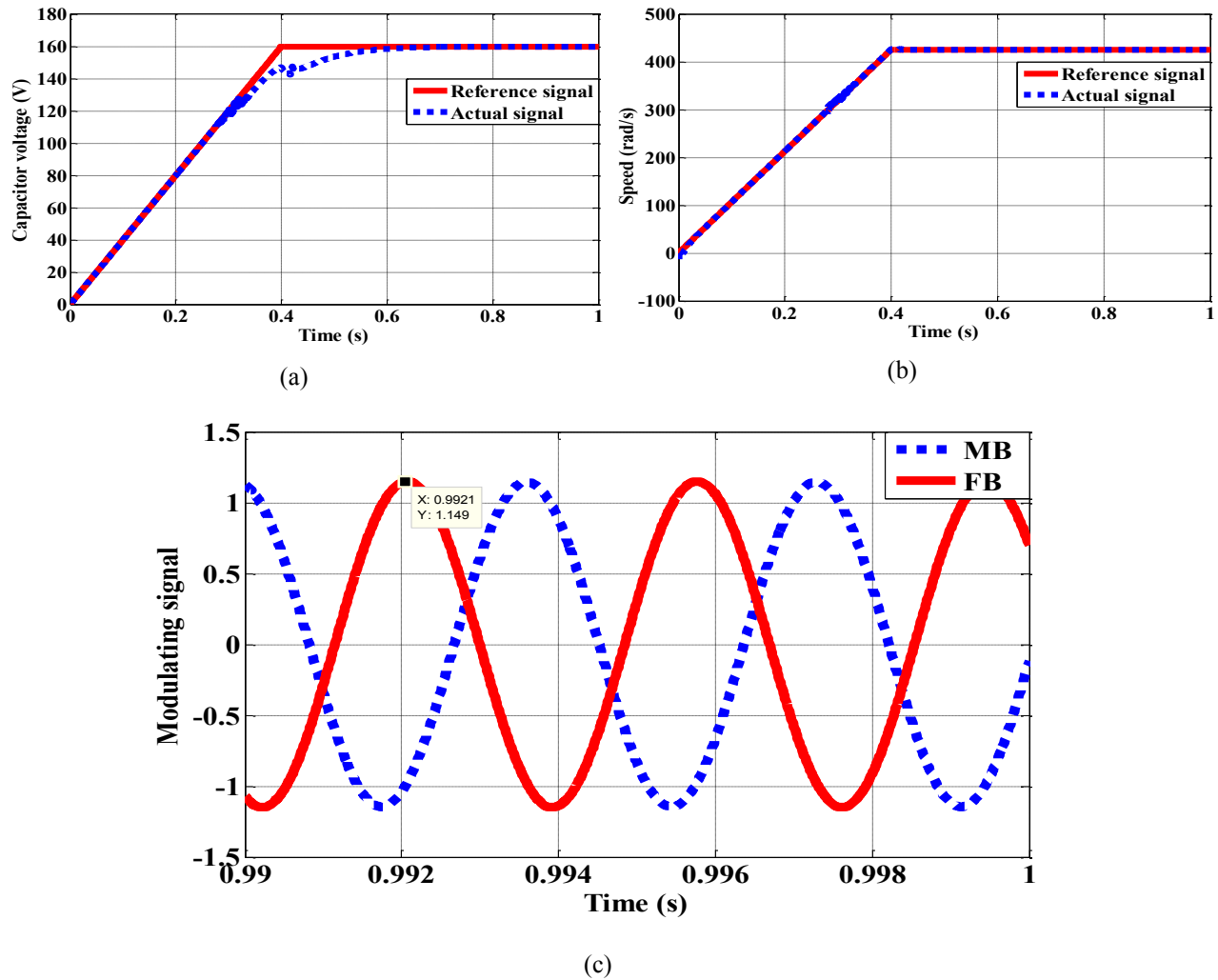


Fig 4.8 a) Capacitor voltage control, b) Speed control, c) Modulating signals assessment in 425 rad/s

According to Fig 4.8, when the machine is working beyond the CPSR area, there is a phase difference of more than 90 degrees between the MB and FB voltage vectors. In this case, the controller sets the MB and FB modulating signals to their maximum values (1.15). In this region, the rated power is no longer available. However, capacitor voltage control and speed control are both precisely fulfilled in this operating region.

To have a clear view of the machine's performance using the dual inverter drive and single inverter drive, the torque-power versus speed profile in single and dual inverter drives are shown in Fig 4.9 for wide range of speeds. The extended operating region from 210 rad/s in a single inverter drive to 297 rad/s using a dual inverter drive shows the contribution of employing the PMSM in an open winding structure and using the dual inverter drive scheme.

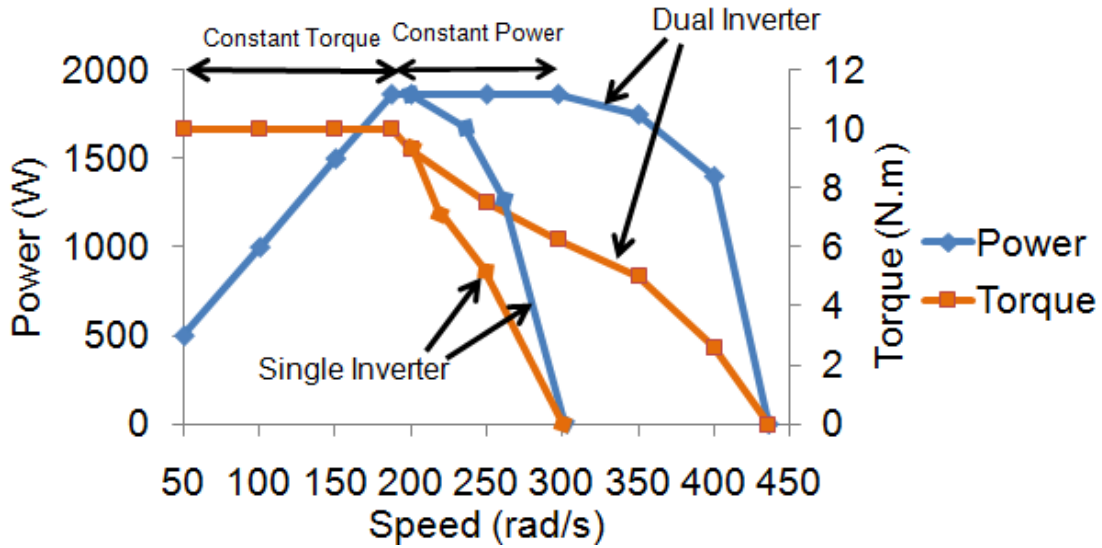


Fig 4.9 Torque-Power versus speed profile showing different regions of operation for the comparison purposes

The required controller for the dual inverter open winding SPMSM is mathematically analyzed and some simulations verifying the performance of the controller are included by Simulink simulations. The simulation analysis shows that appropriate voltages are applied to the machine's phase, and the operating region of the PMSM can be extended by 41% if the introduced controller is precisely implemented.

4.2 Finite Element Analysis of Open Winding Operation

The designed IPMSM introduced in Chapter 3 is employed in the open winding structure and is fed by two inverters using the dual inverter drive. The vector diagram and control approach are based on what has been previously described in this chapter. The main contribution of this section is to provide more voltage on the designed IPMSM to extend its operating region, including its maximum speed using the open winding structure.

The machine's phases are modeled by FEM coils found in the JMAG-Designer circuit definition table. In addition, since there should be a way to control the current flowing through the machine's phases, the first inverter used in the analysis is a Current Source Inverter (CSI). For all the performance analyses in different speeds and torques, the fundamental component (acquired by FFT analysis) of two converters voltages are monitored and kept within the limitations. For the current study, since the DC link voltage of both converters are the same and equal to 320 V, the fundamental component of the phase voltage for both MB and FB should be

184 V_{peak} at most. The JMAG-Designer circuit for the dual inverter drive structure is shown by Fig 4.10.

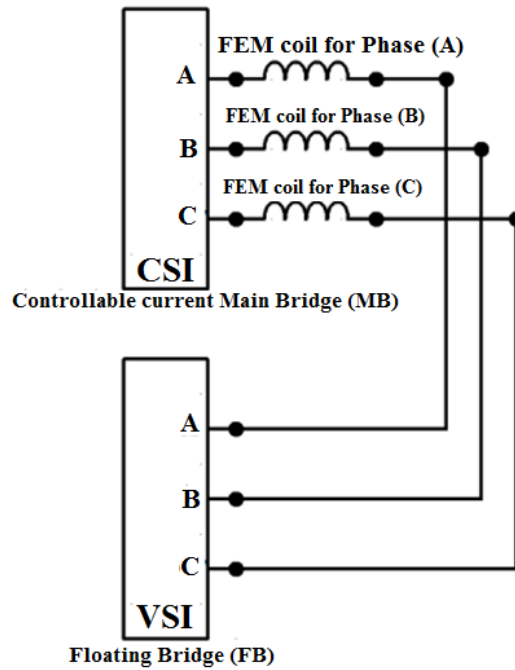


Fig 4.10 The dual inverter open winding IPMSM model in JMAG-Designer

The phase current (peak values) changes in a wide range of speeds to offer the rated power with and without FB activation is evaluated by FEM analysis and is reflected by Fig 4.11. In the single inverter drive, only the MB is used, while in the dual inverter drive, both bridges are activated simultaneously.

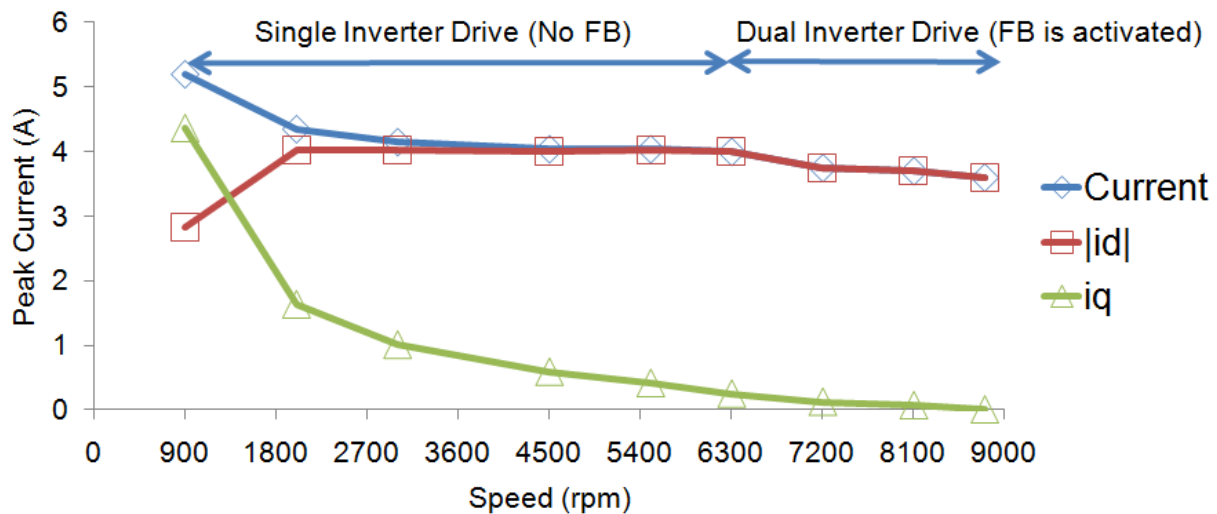


Fig 4.11 Peak current changes in wide range of speeds

According to Fig 4.11, at seven time base speed (6300 rpm), the machine requires 4 Amps peak current to generate the maximum possible power. After seven time base speed, the FB is employed, and FEM analysis shows that less current (3.8 Amps) is required to offer the maximum power. In this area, the q-axis component current is small, and the main portion of the current amplitude is supported by the d-axis component. FEM analysis shows that if the dual inverter drive is used, the maximum speed of the machine can be shifted from 6300 rpm to 8800 rpm. In order to see the d- and q-axis components' changes in the FB voltage vector, Fig 4.12 is shown in a wide range of speeds.

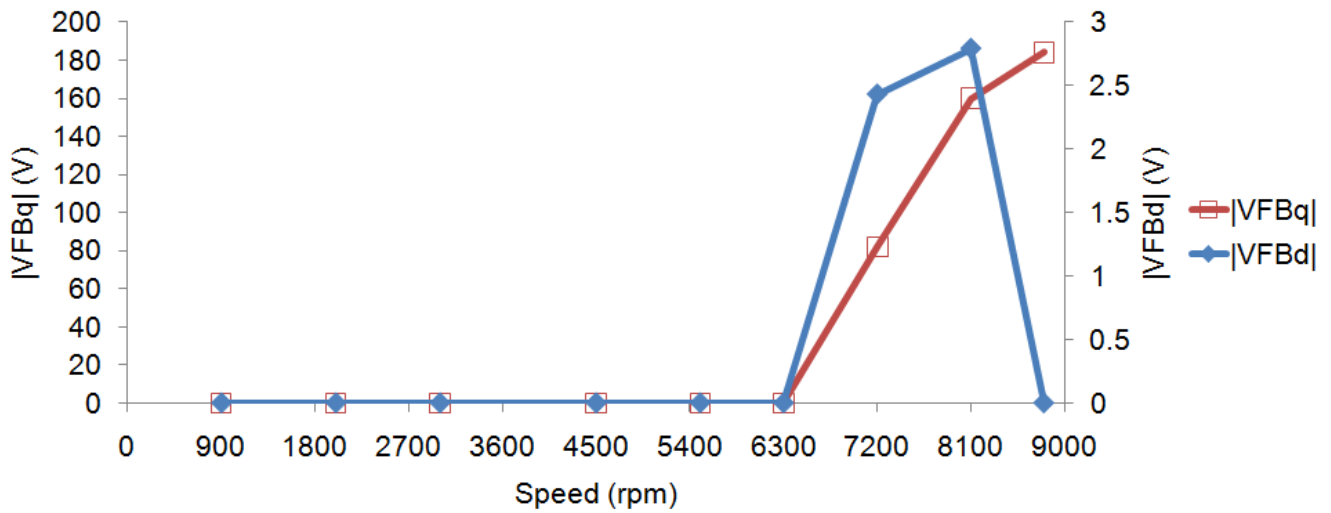


Fig 4.12 The Floating Bridge (FB) voltage components in wide range of speeds

In Fig 4.12, the FB's contribution is more clearly seen after 6300 rpm. In this range, current is almost adapted to the d-axis, and since the FB voltage is perpendicular to the machine's current, its d-axis voltage component is too small to be observed. On the other hand, by increasing the machine's speed, the q-axis component of FB voltage is increased to supply the machine's required terminal voltage.

Power-torque versus speed profile analyzed by 2D-FEM in wide speed range is shown by Fig 4.13. The mechanical losses, including friction and windage losses described in [80], are taken into account.

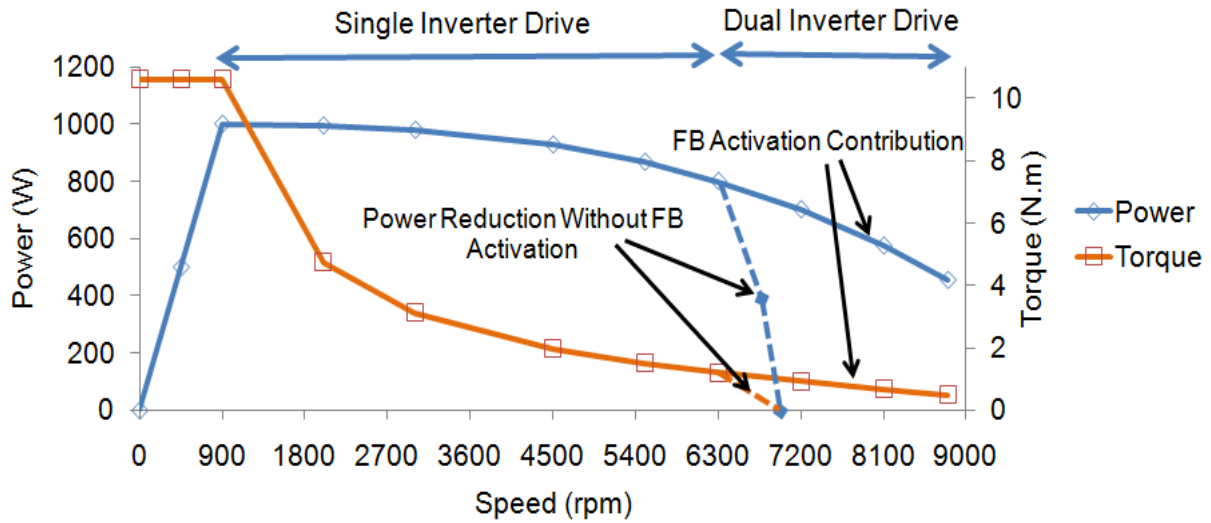


Fig 4.13 Power-torque versus speed profile for showing the contribution of the dual inverter drive structure

Although it is assumed that employing the second inverter may extend the speed range of the machine, due to the mechanical losses (especially friction and windage loss), the rated power cannot be fulfilled in higher speeds. However, the maximum speed of the machine is extended from 6300 rpm (found in single inverter drive) to 8800 rpm in the dual inverter drive structure.

4.2.1 Open Winding IPMSM'S Loss Analysis and Efficiency Assessment

Iron loss, copper loss and efficiency evaluation for the designed IPMSM in open winding structure using dual inverter drive are investigated in this section. All the physical and material considerations are similar to those presented in Chapter 3. But the phases of the designed IPMSM are opened and are fed by two separated converters as shown by Fig 4.10.

For the comparison between the single inverter and dual inverter drive structures, the loss analysis and efficiency profiles are depicted for the whole range of speed. Before seven times base speed, only the MB is used to provide the required power to the IPMSM. On the other hand, for speeds between seven times (6300 rpm) and 9.8 times base speed (8800 rpm), the FB is activated and employed, as MB is not able to provide the required voltage after seven time base speed.

The main electrical losses, including copper loss and iron loss, are shown by Fig 4.14. The frequency-dependent copper loss evaluation has been neglected in the copper loss analysis.

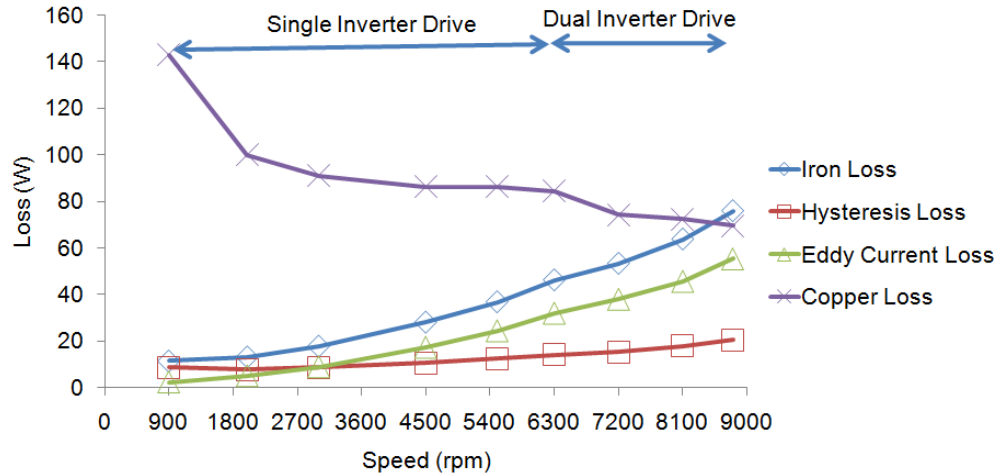


Fig 4.14 Copper loss, and iron loss analysis in wide range of speeds using single and dual inverter drives

The analysis reveals that, since the required current for having the rated power in the dual inverter drive is lower compared to the single inverter, the copper loss is lower than in single inverter drive.

The efficiency analysis for the wide speed range operation, including the single and dual inverter drive regions, is shown by Fig 4.15.

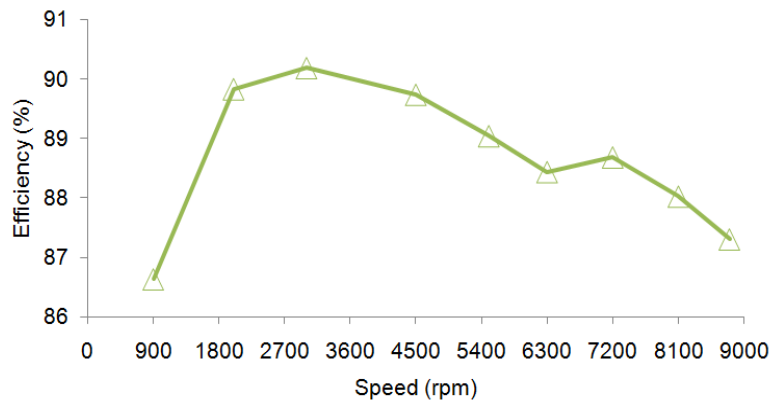


Fig 4.15 Efficiency analysis for the designed IPMSM in the wide range speeds

The analysis shows that the machine's efficiency in speeds above 6300 rpm for the open winding structure is still promising and is more than 87%. The lower efficiency seen in the dual inverter drive structure compared to lower speeds fulfilled by the single inverter drive is due to the higher iron loss in the rotor and stator structures because of the higher applied electrical frequency on the machine's phases.

It is shown by Chapter 3 that the total iron loss is affected by iron loss changes in different harmonics. FFT analyses have been carried out to find out the trend of harmonic iron loss variation versus speed, and the results are presented for the designed IPMSM in the wide speed range operation (See Fig 4.16).

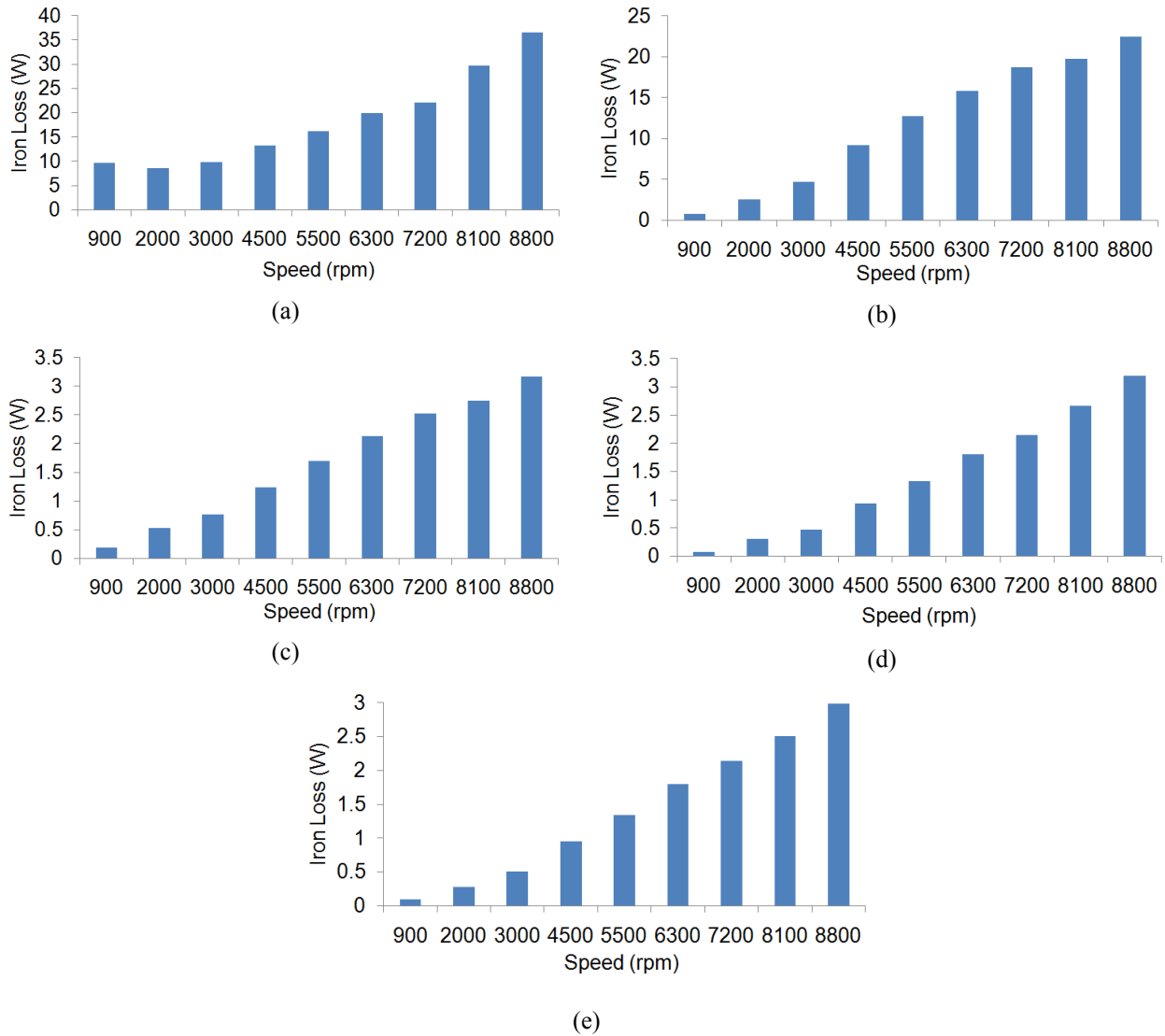


Fig 4.16 Iron loss harmonic analysis in single and dual inverter drive structures for the designed IPMSM in a) Fundamental harmonic, b) 3rd harmonic, c) 5th harmonic, d) 7th harmonic, e) 9th harmonic

The fundamental component of iron loss has the highest amplitude compared to the other harmonics. The third harmonic is placed in the second rank. Iron losses in fifth, seventh, and ninth harmonics are much significantly lower than fundamental and third harmonic iron losses. This trend confirms that most of the iron loss seen in the machine's structure is due to the

fundamental and third harmonic iron losses. In Chapter 3, the contribution of each harmonic in total iron loss production is shown for the base speed and seven times base speed. Now, this contribution is shown by Fig 4.17 for 9.8 times base speed (8800 rpm) which is the maximum possible speed that can be provided by the dual inverter drive structure.

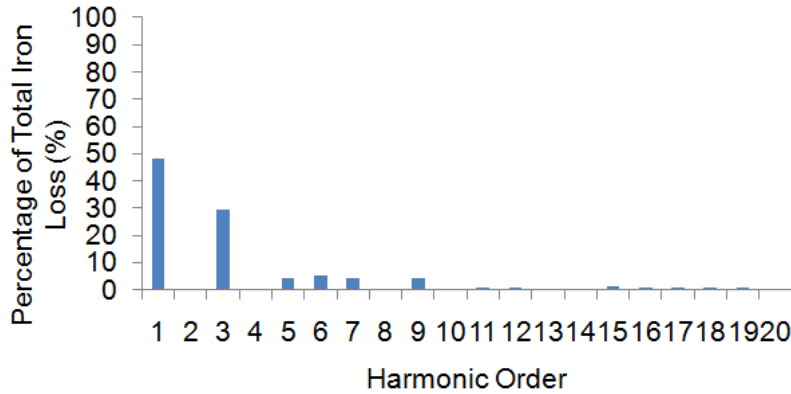


Fig 4.17 The contribution of each harmonic to the total iron loss of machine in 8800 rpm

According to Fig, 4.18, fundamental harmonic has almost 48% contribution to the total Iron loss of the machine, while third harmonic has 30% contribution. Other harmonics have less than 5% contribution to the total Iron loss assessment.

4.3 Summary

In this chapter conceptual vector diagrams are introduced to explain the concept of the dual inverter feeding the machine in the open winding structure using a FB. The diagrams show that, if two same magnitude and perpendicular voltages (MB and FB) are simultaneously applied to the machine's phases, the maximum speed and operating region of the machine can be extended by factor of 1.41. In addition, the FB is capable to provide or absorb the reactive power based on the operating point of the machine.

A control approach is introduced to enable the MB and FB to supply the required voltage of the machine in the dual inverter drive structure. FB is activated after the maximum possible speed of the machine seen in the single inverter drive, and is utilized to support the reactive power requirement of the machine. MB, on the other hand, is used to support the real power required by the open winding machine. The MB voltage and current are set to be always in phase while the current and the FB voltage are perpendicular in all operating points. The introduced controller performance is evaluated by Simulink simulation using an SPMSM example. In

Simulink simulation, the average model VSCs are used and the open winding IPMSM is modeled in d-q reference frame without taking into account the mechanical losses and electromagnetic losses. The result of the evaluation shows a 41% extension in the operating region of the SPMSM. Although the performance of the machine is examined in ideal case scenario by neglecting some important loss sources, but the simulation analysis verifies how the control approach works in wide range of speeds.

The designed IPMSM introduced in Chapter 2 is employed in an open winding structure. FEM analysis is carried out to obtain the torque-power versus speed profile. The Main Bridge (MB) is modeled by controllable Current Source Inverter (CSI) while the Floating Bridge (FB) is modeled by the controllable Voltage Source Inverter (VSI) picked up from the circuit library of JMAG-Designer software. The phases of machine are modeled by the FEM coils which are defined by number of turns and the resistance per phase. The simulations show that, when only a single inverter drive is used and the machine is employed in a Y- connected case, the machine's maximum speed is 6300 rpm. Alternatively, when the machine's phase windings are rearranged in an open winding structure and the dual inverter drive structure is used, the maximum speed of the machine and its operating regions are extended to 8800 rpm. However, due to the mechanical loss including friction and windage losses especially in high speeds, the expected rated power cannot be supported for the entire wide speed range. The operating region extension is due to the increased voltage provided on the machine's phases in the dual inverter drive structure.

The loss and efficiency analysis are presented in wide speed range operation. The iron loss has been evaluated using Fast Fourier Transform (FFT) option in JMAG-Designer's loss analysis toolbar and the efficiency has been verified by taking into account the iron loss and copper loss evaluation in wide range of speeds. The FEM evaluation illustrates that the efficiency of the machine in an open winding structure is still more than 87%.

FFT analyses are included to show the contributions of each harmonic on the total iron loss production at the maximum possible speed of the IPMSM in the dual inverter drive structure. The analyses show that the contributions of the fundamental and third harmonic components are more than those of the other harmonics in the total iron loss of the machine.

Briefly, the contribution of Chapter 4 is to show how the operating region of a PMSM can be extended by applying more voltage on the machine's phases using a reliable controller in a dual inverter drive scheme.

Chapter 5

EXPERIMENTAL VERIFICATION

The IPMSM introduced and analyzed in Chapters 3 and 4 is built, and its performance is experimentally evaluated in both Y-connected winding configuration and open winding configuration. In this evaluation, the Back-EMF voltage, inductance, losses, efficiency, and speed range assessment are presented. Additionally, a new control technique is proposed and implemented for the open winding IPMSM using the dual inverter drive to verify the operating region extension.

5.1 Machine Construction

The stator lamination, rotor lamination and magnet are shown in Fig 5.1 and Fig 5.2, respectively. The drawn models include the most important dimensions.

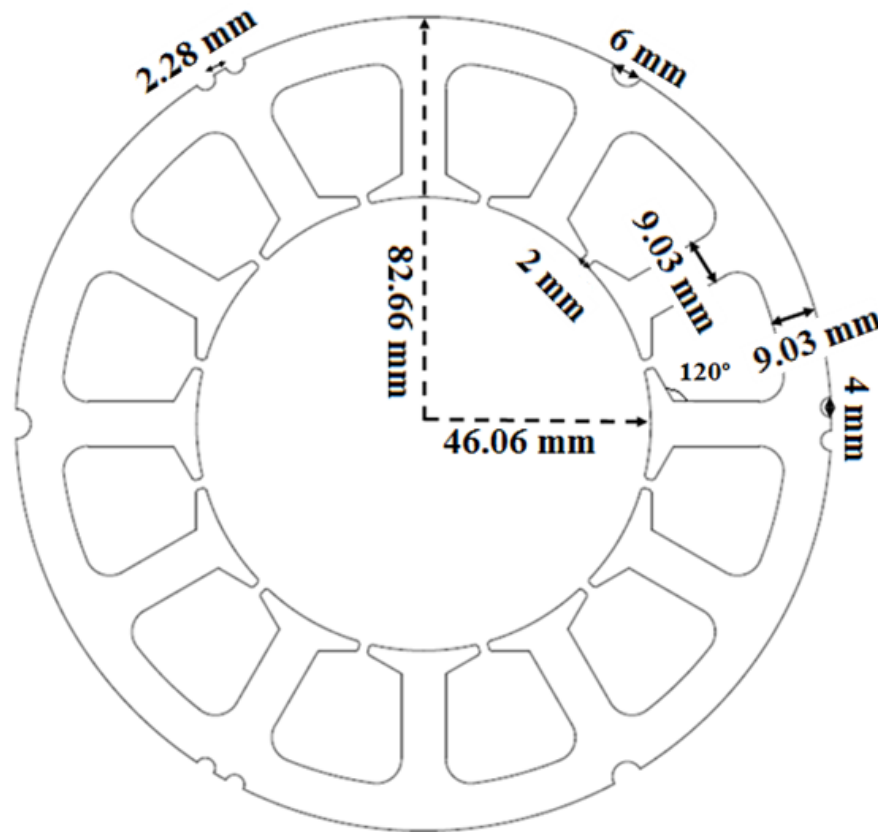


Fig 5.1 The stator lamination and its different dimensions in Auto-CAD

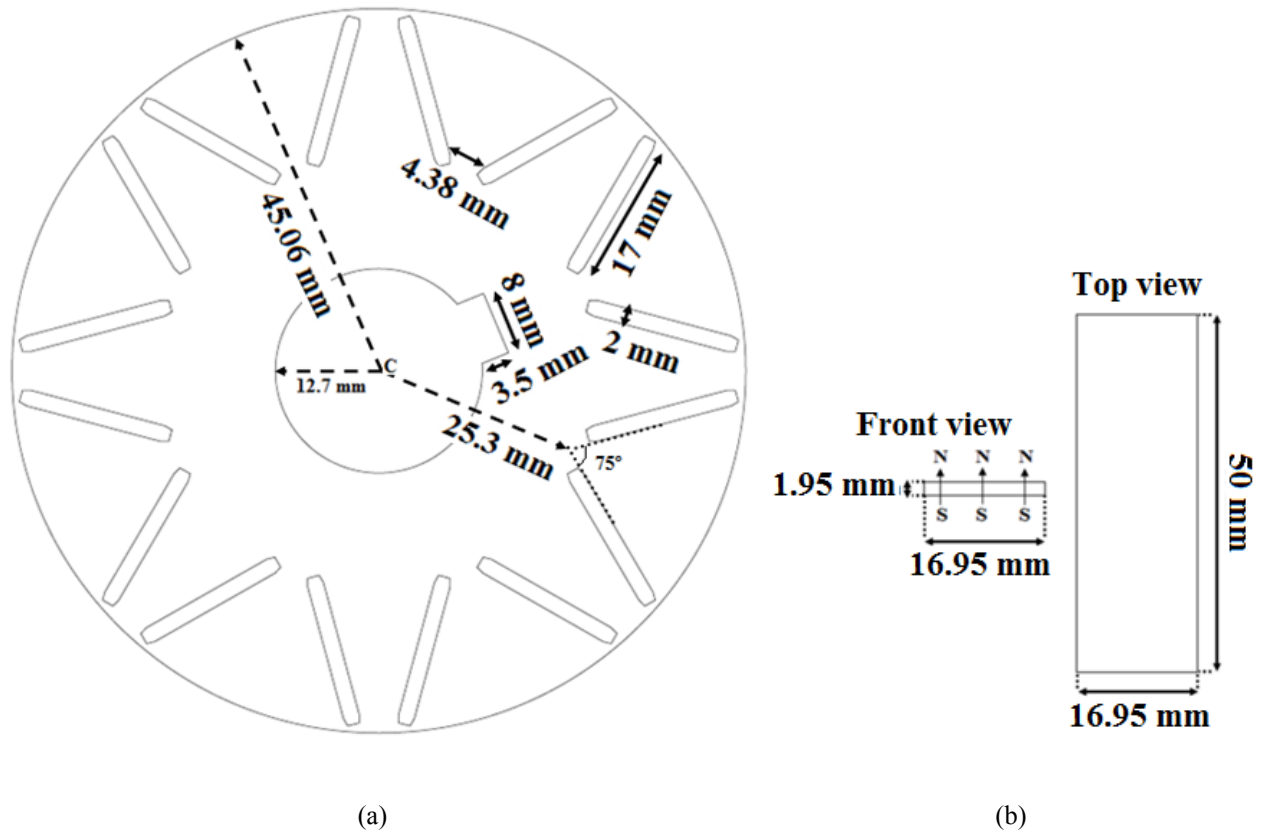


Fig 5.2 a) Rotor, b) Magnet dimensions

In these figures, all the dimensions are equal to those used in the FEM simulations. However, in building the machine, some minor modifications are made on the rotor and magnet dimensions. For instance, one key way hole is installed on the rotor's shaft to fix the lamination. Furthermore, notches on the stator lamination models are used to do the suitable alignment of the stator laminations, especially when welding the stator laminations. In addition, the length and the width of the drawn magnet are slightly smaller than those of the magnet used in the simulation. This modification allows the magnet to be inserted into the rotor tolerances more easily and without the severe pressure.

The drawn stator and rotor models have been manufactured by 150 laser cut 29 gauge M19 laminations from Proto Laminations Inc. The magnet has been manufactured by Allstar Magnetics Company in the U.S.

The cut 29 gauge M19 laminations for the rotor and stator of the machine are shown in Fig 5.3.

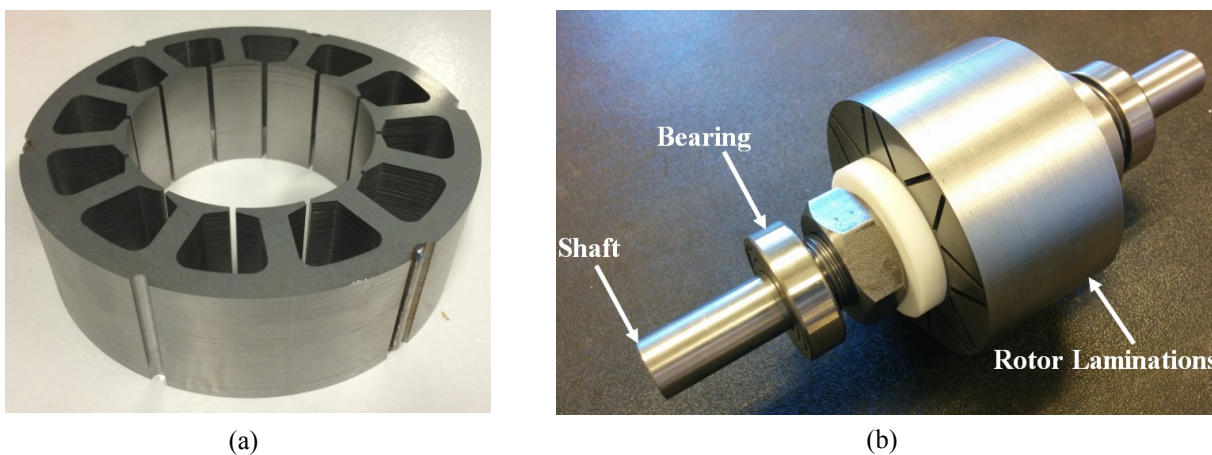


(a)

(b)

Fig 5.3 Actual laminations for a) Rotor, b) Stator

137 stator laminations have been welded and aligned to have the 5 cm stator stack. The rotor laminations have been punched together and fixed by two fibre glass layers and two screws. The welded stator stack and the rotor of machine are shown by Fig 5.4.



(a)

(b)

Fig 5.4 a) Welded stator stack, b) The rotor fixture

The NEOMAX-35EH magnets have been ordered from Allstar Magnetics Company. A sample magnet is shown by Fig 5.5.



Fig 5.5 NEOMAX-35EH used in the built machine structure

The welded stator stack is wound by Bata Electric Company (located in Calgary, Alberta) using the winding requirements utilized in the simulation analysis. Each coil consists of 135 turns of AWG 20 copper wire. Coils in each phase are connected in series.

The winding arrangement for the 12 slot 8 pole IPMSM is shown by Fig 5.6, and the actual wound stator structure is shown by Fig 5.7.

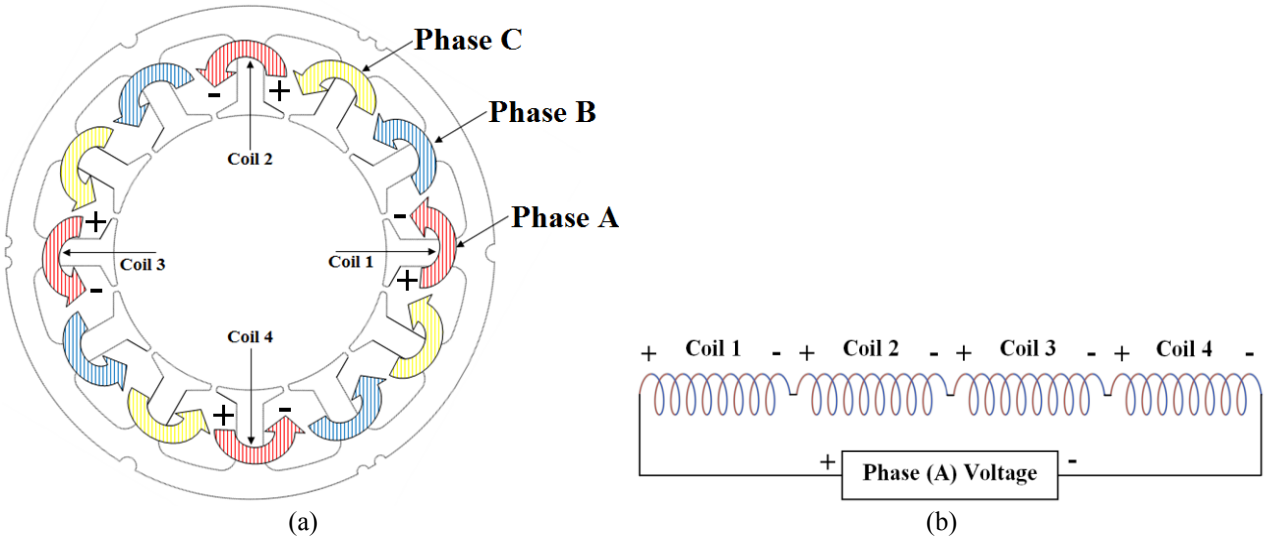


Fig 5.6 a) Winding arrangement for the 12 lost 8 pole IPMSM, b) Coils arrangement for phase (A)



Fig 5.7 The actual wound stator

The internal view of the built machine including all the introduced parts is shown by Fig 5.8.

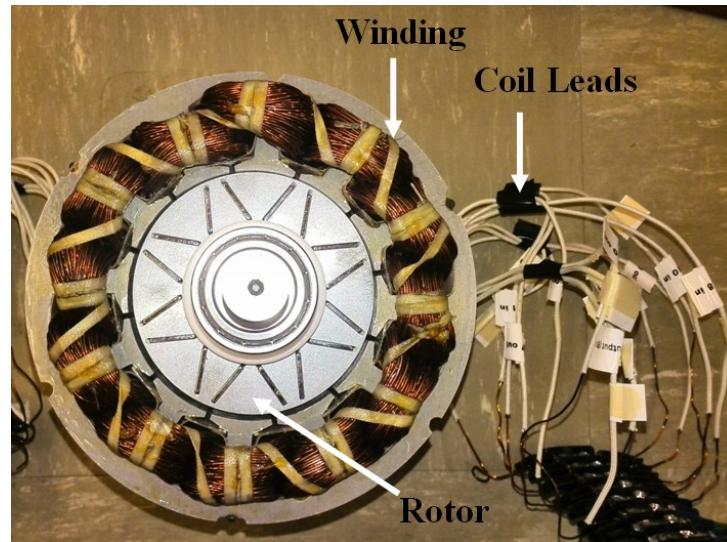
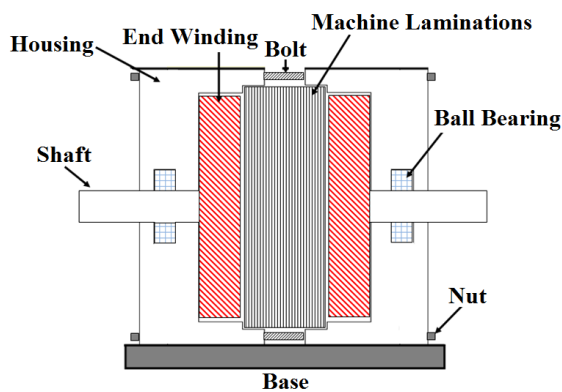
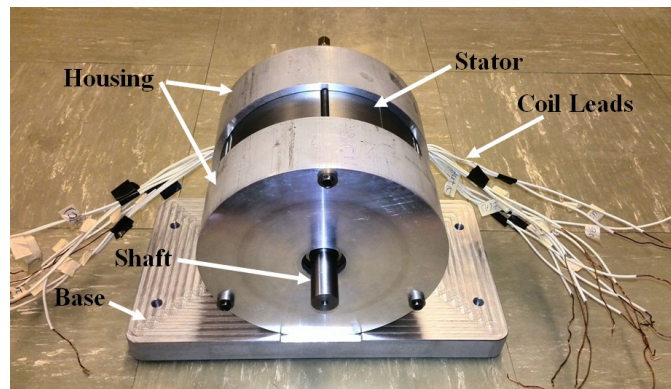


Fig 5.8 The built machine

The schematic depictions of the complete frame on the base plus the actual machine in its frame are shown by Fig 5.9.



(a)



(b)

Fig 5.9 a) Schematic side view of the machine's frame and housing, b) The built machine ready for the tests

5.2 Test Rig

To control and monitor the machine performance, two independent DSC control-based schemes are used for the motor side and load side. Each DSC is a TI28335 and is part of a PowerCon controller which handles all signals conditioning between the hardware and DSC. Control is implemented in C using TI code composer and is monitored in real time via JTAG emulator connection to a PC. The load is a 1kW 12 slot, 10 pole IPMSM, and it is used to tune the load applied to the built V-shaped magnet IPMSM. A Semikron IGBT Inverter is used to control the load side and a Semiteach IGBT Inverter is used for controlling the motor side. The

DC links of the two converters are linked, enabling power circulation at the DC level, with the AC supply providing losses through a rectifier.

The Y-connected IPMSM is controlled and investigated using the single inverter drive structure. The conventional single inverter drive structure scheme including the speed and current controllers plus the feedbacks and different parts of the system are shown by Fig 5.10. The schematic diagram of the test rig used in the single inverter drive experiments is shown by Fig 5.11.

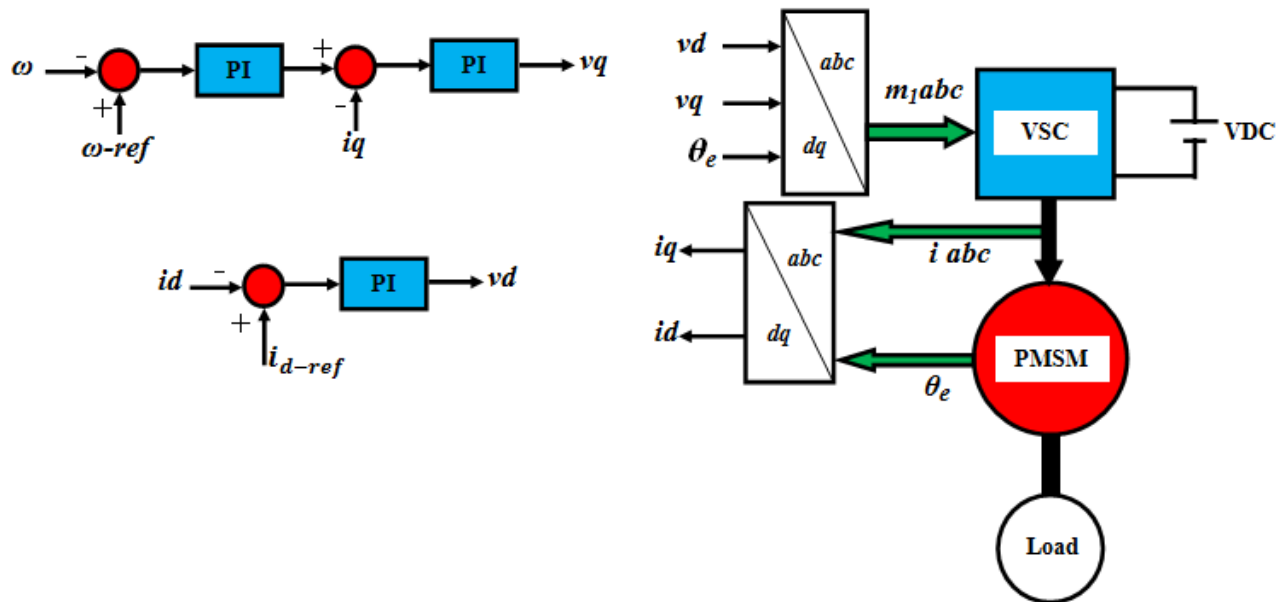


Fig 5.10 The conventional PMSM drive with the control structure

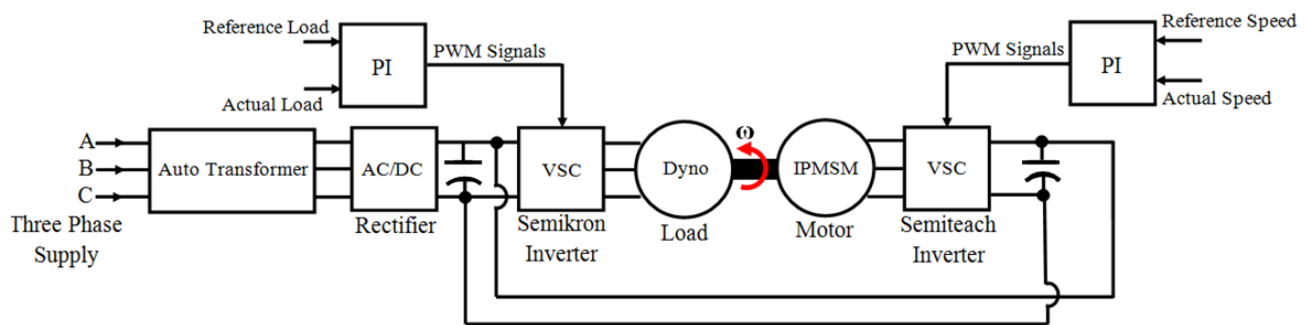


Fig 5.11 The schematic view of the system for the single inverter drive tests

The black Semikron used for the Dyno control, and the Semiteach unit utilized for the motor control are shown in Fig 5.12.

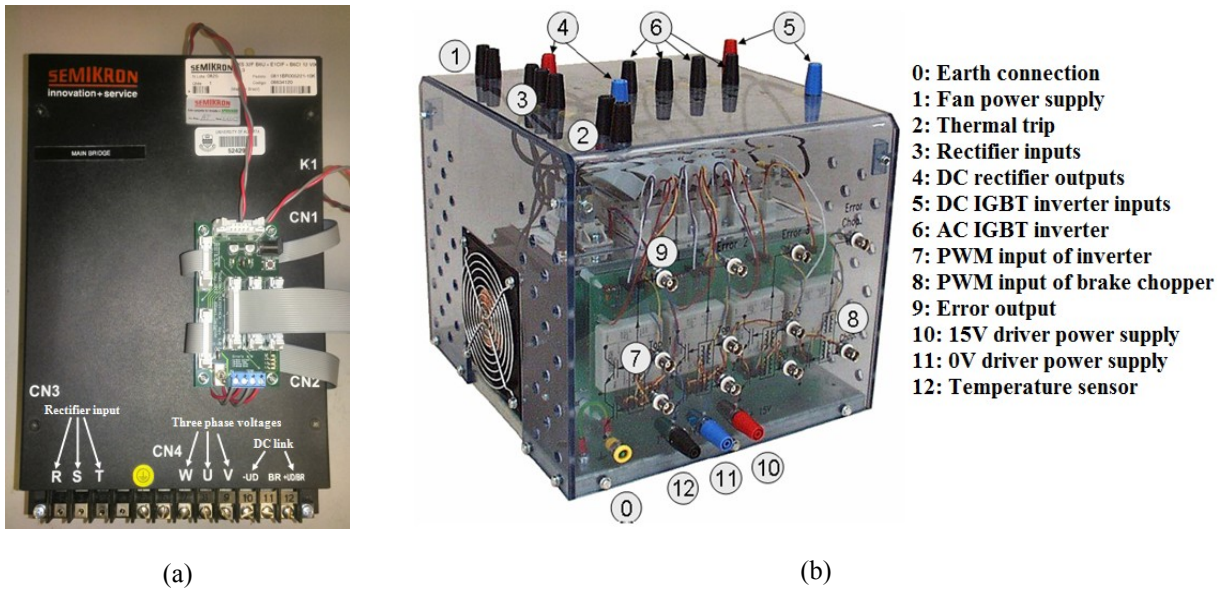


Fig 5.12 a) Semikron inverter for the load side control, b) Semiteach inverter for the motor side control [121]

The test rig and the motor stand with their different parts prepared in the laboratory are shown in Fig 5.13 and Fig 5.14. The torque transducer used for monitoring the load changes is a Futek rotary torque sensor which can be used for loads up to 20 N.m. The bellow type couplers are used for coupling the motor and load's shafts to the torque transducer.

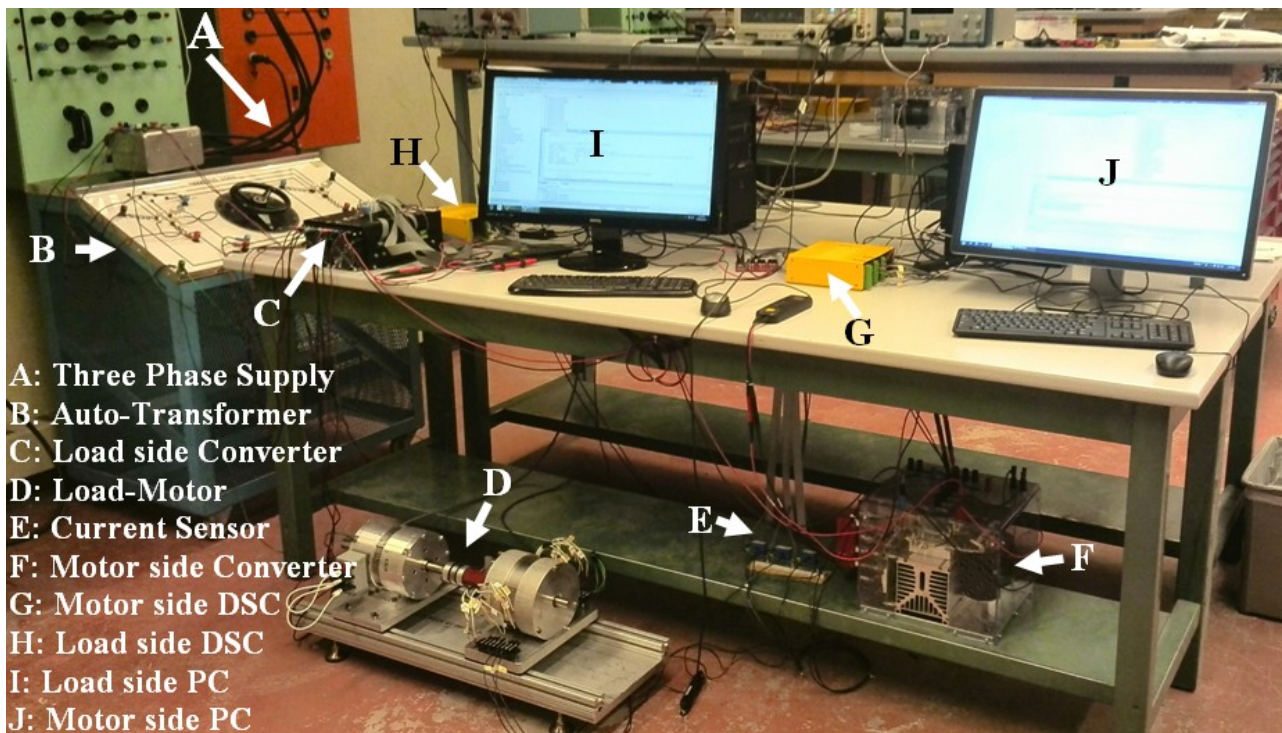


Fig 5.13 Complete test bench in the lab

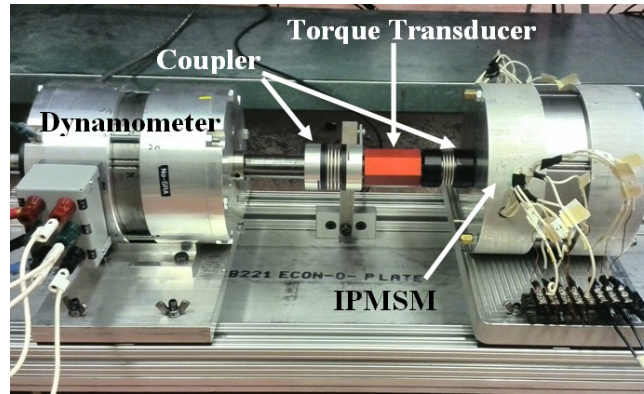


Fig 5.14 Close-up of the motor stand

5.3 Single Inverter Testing

The most important characteristics of the tested machine in the Y-connected configuration using single inverter drive structure are illustrated in this section.

5.3.1 Back-EMF Waveform

To verify the Back-EMF voltage of the built IPMSM, the 12 slot 8 pole IPMSM which is used for load is employed as the prime mover and spins the shaft of the built machine in the speed of 900 rpm. The Back-EMF voltage in the experiments and simulation, taking into account the built machine's specifications and limitations, are shown in Fig 5.15.

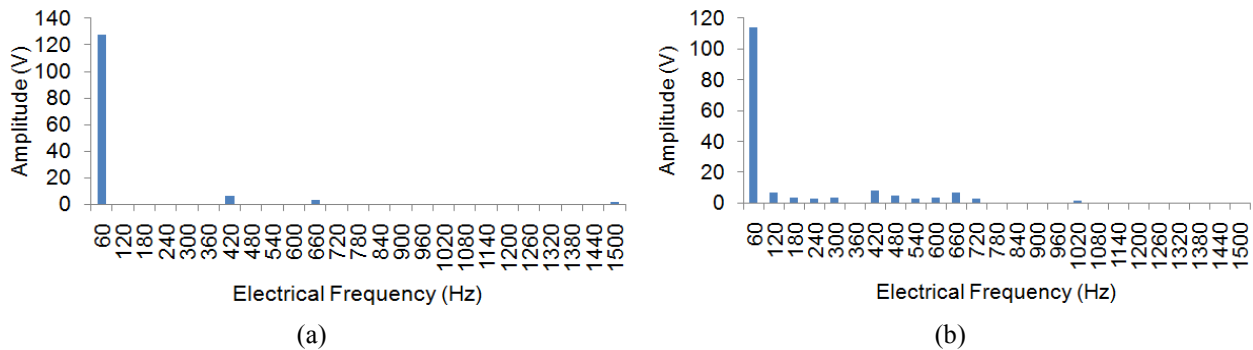


Fig 5.15 Back-EMF voltage verification in open circuit analysis, a) Simulation, b) Experiment in 900 rpm

The THD of the open circuit voltage is 3% in the simulation and 6% in the experiment. In addition, the peak of the fundamental component of voltage is 128 V in the simulation and 114V in the real time tests. The Permanent Magnet (PM) flux linkage is 0.33Wb in the simulation and 0.303 Wb for the actual machine. The PM flux linkage difference causes a 10% reduction in the power density of the built machine compared to the simulated one. In addition, the Back-EMF harmonic analysis indicates that there is a second harmonic component which implies on

unbalanced magnetic field. The combination of the reduced peak flux density and second harmonic are probably due to the manufacturing variation on the introduced magnet as well as 2D analysis approximation.

5.3.2 Inductance Evaluation

The values of the d-axis and q-axis inductances depend on different phenomena such as saturation in the iron or cross-coupling between the two axes. Hence, analytical calculations of the inductances may be inaccurate [122].

The AC standstill method using reactive power measurement investigated in [123] is utilized to measure the machine's d-axis and q-axis inductances. The inductance measurement for the AC standstill approach is carried out using the circuit shown in Fig 5.16.

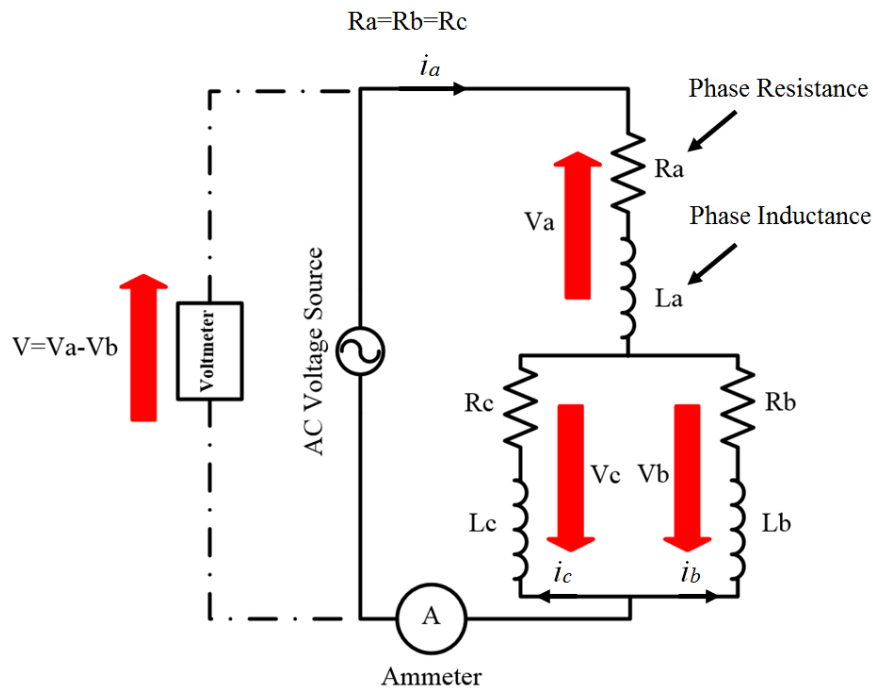


Fig 5.16 Inductance measurement circuit for AC standstill approach

In the AC standstill method, the rotor is locked, and two phases are connected in parallel as in Fig 5.16. The static d-axis and q-axis inductances are calculated from the measurements of the reactive power Q , RMS current I and supply electrical frequency f_e , with a rotor in the d- and q-axes positions respectively [124]. These are illustrated in equations (5.1) and (5.2).

$$L_d = \frac{2}{3} \cdot \frac{Q_{d-axis \ position}}{2\pi f_e \cdot (I_{d-axis \ position})^2} \quad (5.1)$$

$$L_q = \frac{2}{3} \cdot \frac{Q_{q-axis \ position}}{2\pi f_e \cdot (I_{q-axis \ position})^2} \quad (5.2)$$

The value of the RMS current is varied up to the rated current. The static inductances versus the applied RMS current are plotted in Fig 5.17.

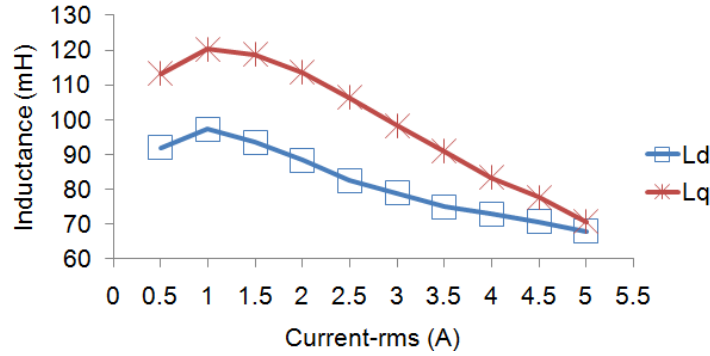


Fig 5.17 d- and q-axes static inductances using AC stand still method (Experiment)

For a better comparison of the inductance of the built machine with what is expected in the simulation (using the built machine specifications), an inductance evaluation versus current magnitude changes and angle is shown by Fig 5.18. The profiles presented by Fig 5.18 are obtained by the FEM simulations.

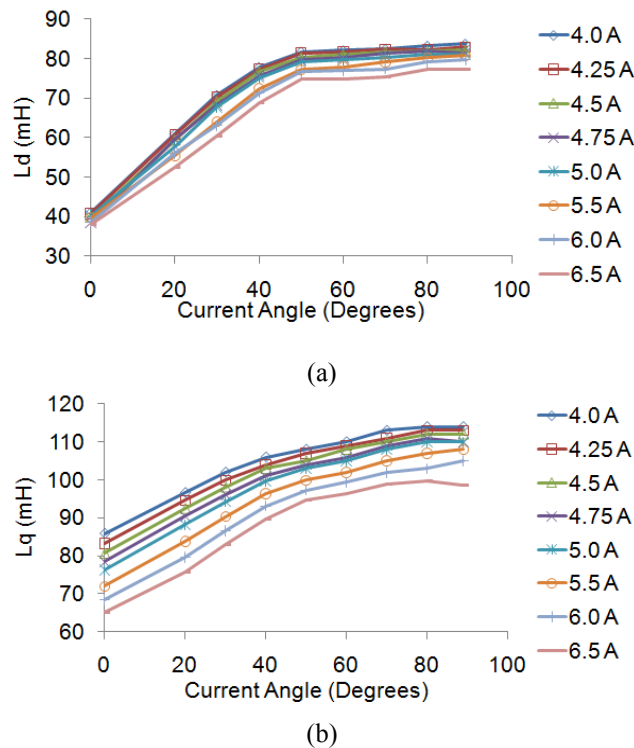


Fig 5.18 a) L_d and b) L_q as the function of current magnitude and angle for the built machine, (Simulation)

According to the inductance profiles, Fig 5.18(a) and Fig 5.18(b), when the current magnitude is increased, both L_d and L_q decrease. This is because the d-axis and q-axis paths are more magnetized which causes the saturation and the smaller inductances. In larger current angles, the larger field weakening current (i_d) is applied to the phases of machine. The larger i_d causes the demagnetization in both d-axis and q-axis and increases the inductances.

The other finding is that the L_q values in the simulation and in the experiment are close while the L_d value in the built machine is much bigger than its value in the simulations. The L_d in the simulation is approximately 40 mH (zero degree current angle), while in the experiment, it varies between 70 mH to 90 mH. The inductance discrepancy is due to the difference between the permeability of the utilized steel in the built machine and that which has been used in the simulation. On the other hand, the iron bridge in the built machine is not highly magnetized like the iron bridge used in the simulation. This accounts for a bigger L_d in the experiment. The end winding, which has been neglected in 2D simulation, is the other reason for a bigger L_d in the built machine. Having a bigger L_d causes more reduction in saliency and power density of the built machine.

5.3.3 Current Profiles for the Tested Machine

The Field Oriented Control (FOC) is used to control the machine. To fulfill this kind of control approach in the field weakening area, d-axis and q-axis current profiles play an important role in the no load and loaded performance of the machine. The three phase currents in no load condition and in 80% load condition are shown by Fig 5.19(a) and Fig 5.19(b). As an example, the d-axis and q-axis currents in an 80% loaded case are shown by Fig 5.19(c).

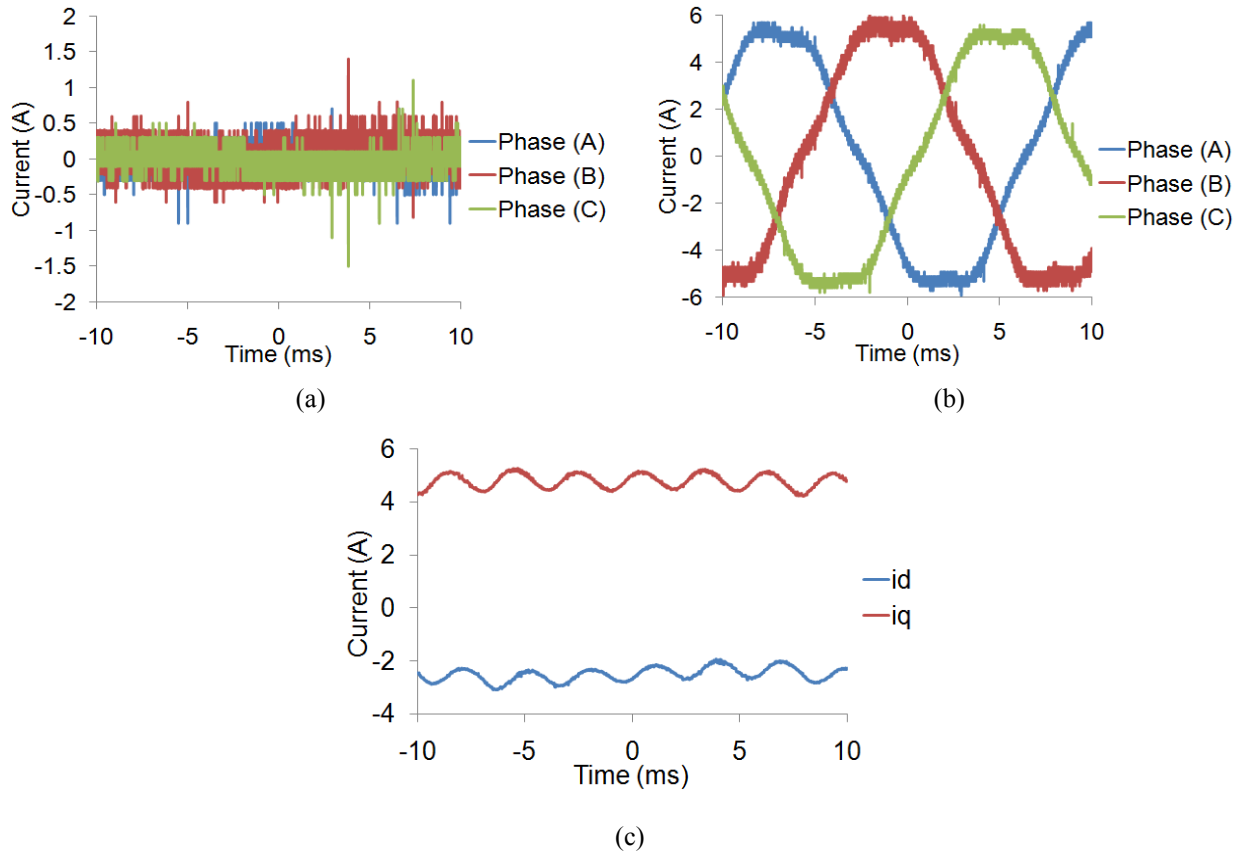


Fig 5.19 a) Three phase currents in no load, b) Three phase currents in 80% load, c) d- and q-axis currents in 80% load (Experiment, 900 rpm)

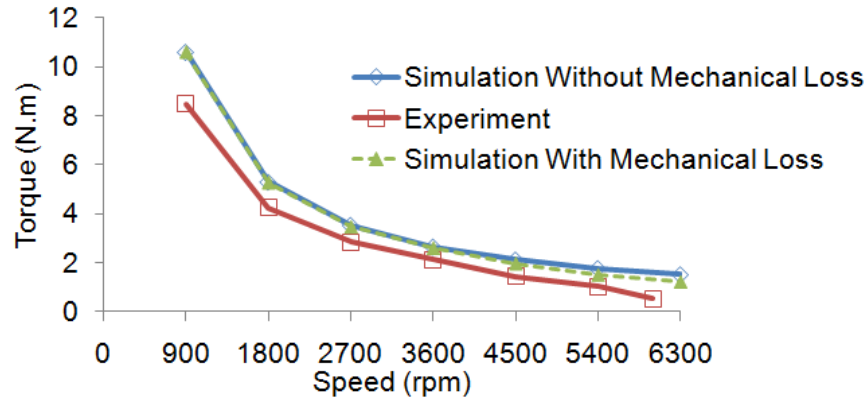
According to the Fig 5.19(a) and Fig 5.19(b), it is shown that in the no load case, the amplitude of the required current is smaller than 0.5 Amps, while in the bigger loads, the amplitude of the required current is approximately 6 Amps. The d-axis and q-axis current values are not fixed DC values, and 0.4 Amps fluctuations are seen on the d- and q-axes profiles.

5.3.4 Field Weakening and Maximum Speed of the Tested Machine

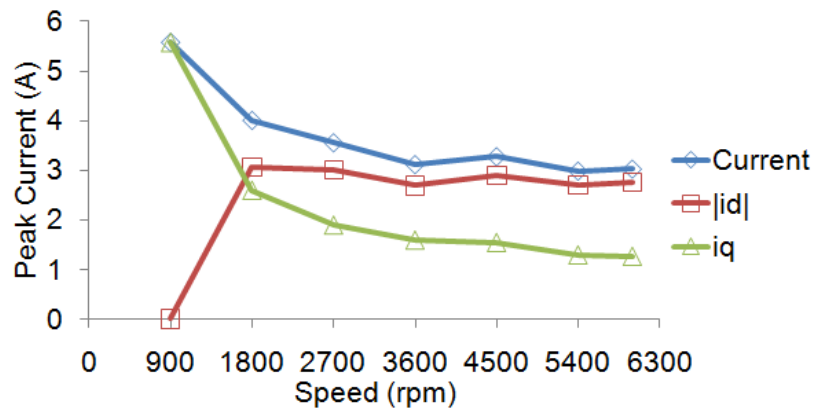
The field weakening control method is used to evaluate the speed range of the built machine.

It is demonstrated by Chapter 3 that the designed IPMSM is able to provide a wide speed range up to seven times base speed in FEM simulations. When the FW control method is employed, the experimental investigations illustrate that the maximum speed range of the built machine is 6000 rpm or 6.66 times base speed.

The torque versus speed capability of the built machine and simulated machine plus the d-axis and q-axis currents during FW control are shown by Fig 5.20.



(a)



(b)

Fig 5.20 a) Torque versus speed capability of the machine in simulation and experiment, b) d- and q-axis current profiles in FW region (Experiment)

As is seen in Fig 5.20(a), the built machine's developed torque is less than what it is expected in the simulation, particularly in higher speeds. A part of the reason is that the mechanical losses in experiment are much more than what has been taken into account in simulations and the PM flux linkage of the built machine is at least 10% less than the simulations which causes the magnetic torque of the built machine to be less in experiments. However, the machine still shows a promising wide speed range operation. In addition, according to Fig 5.20(b), smaller currents are required for the high speed regions, as lower loads are needed in higher speeds.

Although the built machine's performance analysis is not exactly similar to what has been expected, the wide range speed operation up to 6000 rpm or 6.66 times base speed has been fulfilled experimentally. The experimental assessments verify the method for designing a machine with wide speed range operation using the geometry changes method.

5.3.5 Losses and Efficiency

To have more accurate loss analysis comparison between the built machine and the simulated machine, the following physical considerations of the built machine are taken into account:

- In simulations the coil resistance is estimated based on approximate coil length. In the built machine the end windings are larger than the estimate. This issue causes the phase resistance of the built machine to be 3.9Ω , which is larger than the simulation estimate of 3.6Ω .
- In the built machine. The width of the magnet should be a slightly smaller than the tolerances in the rotor structure. Otherwise the magnets cannot fit into the tolerances. So in the final design simulation, there should be an airgap around the magnets for having more accurate model. This issue reduces the effective magnet's flux density and machine's power density.
- In the simulation the stack factor should be set to a number less than 100%, because in manufacturing process that is not possible to have the 100% stack factor. This factor is set to 93% in the simulation to make the final model design more similar to the built machine.

The Back-EMF and inductance evaluations illustrated by Fig 5.15(a) and Fig 5.18 have taken into account the above mentioned physical limitations and considerations. The expected copper loss and iron loss of the final model taking into account the real physical considerations of the built IPMSM is simulated by FEM analysis and is presented by Fig 5.21.

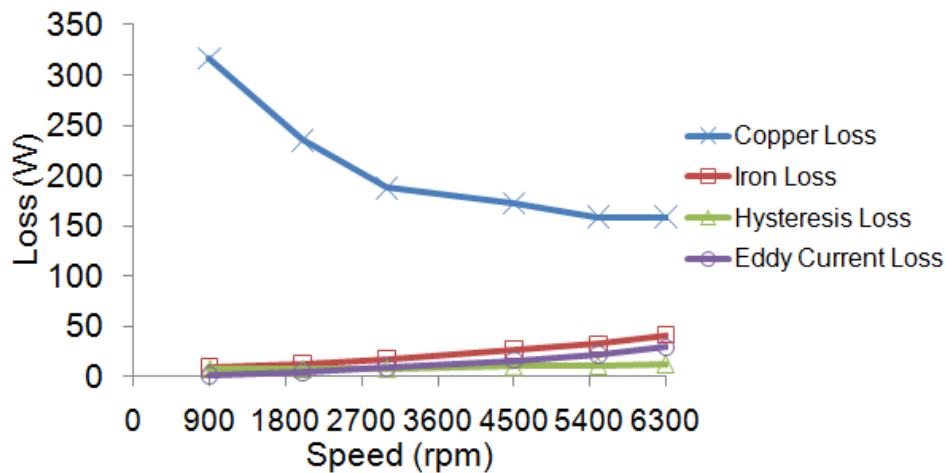


Fig 5.21 Loss evaluation for the final model in 1kW power (FEM Simulation)

In addition to the electrical loss analysis, the JMAG-RT has been used to predict the efficiency scatter of the designed machine taking into account the electrical losses of machine, and the important physical considerations of the built machine. The torque-efficiency profile

versus speed for the final model is shown by Fig 5.22. It is worth noting that the mechanical losses have been neglected in simulation analysis. As is seen, the efficiency of more than 90% is expected for the designed machine using the JMAG-RT simulations.

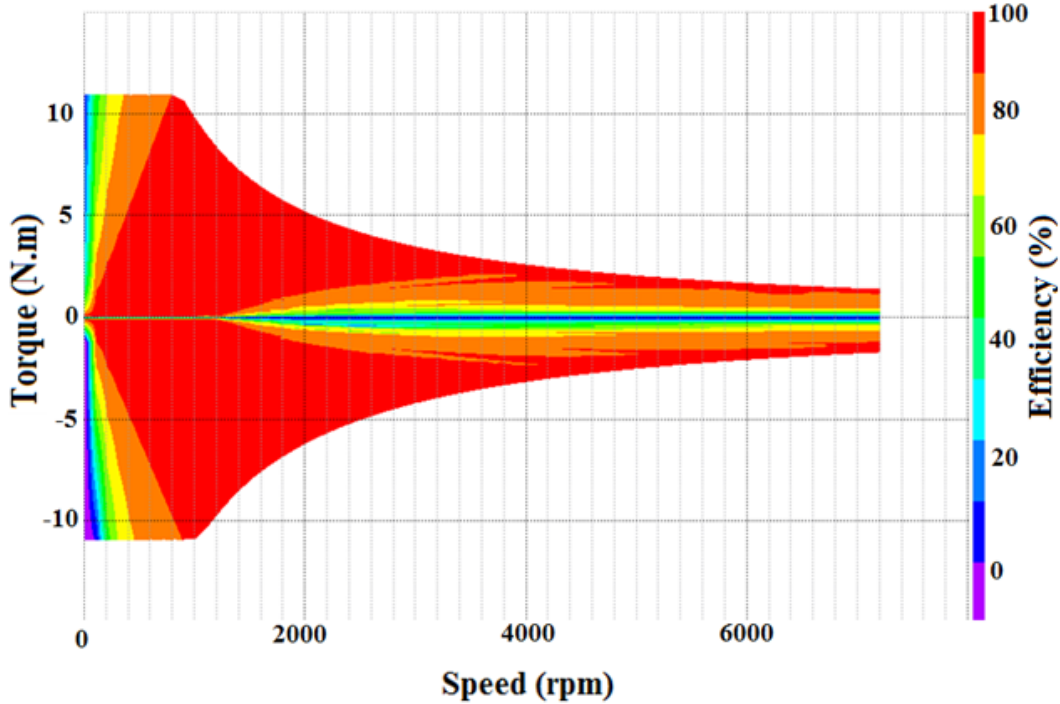


Fig 5.22 Efficiency assessment of the finally designed IPMSM in wide range speeds and loads using JMAG-RT (Simulation)

To measure the friction and windage loss plus iron loss, equation (5.3) is used;

$$P_{F\&W+Iron\ Loss} = P_{in} - P_{out} - P_{Copper} \quad (5.3)$$

P_{out} is the output power of the machine which is the function of the developed torque and speed of the machine. P_{Copper} is calculated as the function of the phase resistance (3.9 Ω) and the measured current flowing through the phases shown in Fig 5.20(b). It is worth noting that the copper loss evaluation associated with frequency changes has been neglected. P_{in} is the average value of the input power calculated by two current meters method, see Fig 5.23 and equation (5.4).

The built machine has been tested up to 6000 rpm and the copper loss, and iron loss plus friction and windage losses of the tested machine from 900 rpm to 6000 rpm are shown in Fig 5.24 and Fig 5.25.

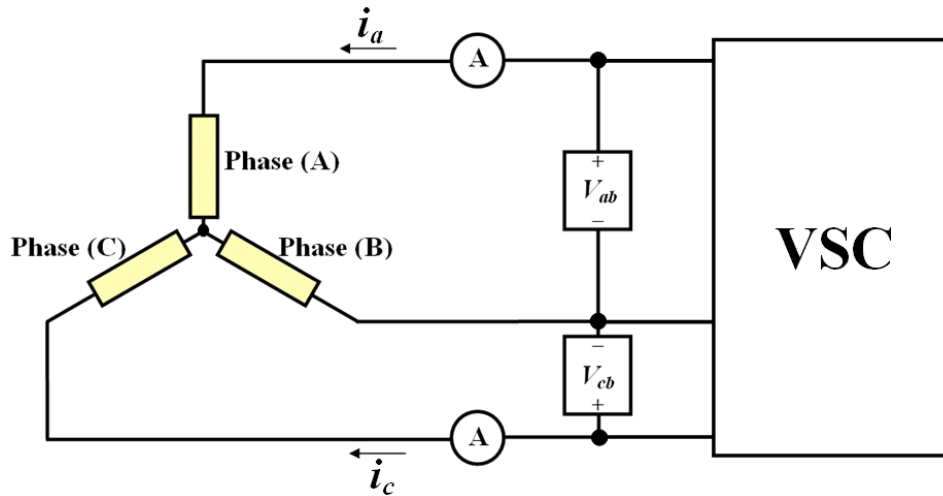


Fig 5.23 Circuit configuration to measure the input power of the machine

In order to measure the input power of machine equation (5.4) is used.

$$P_{in} = (V_{ab} \times i_a) + (V_{cb} \times i_c) \quad (5.4)$$

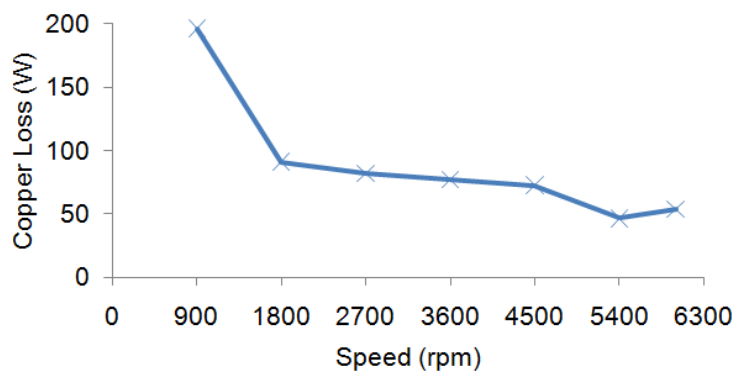


Fig 5.24 Copper loss analysis (Experiment) in the maximum possible power (it is assumed that the resistance is not the function of frequency changes)

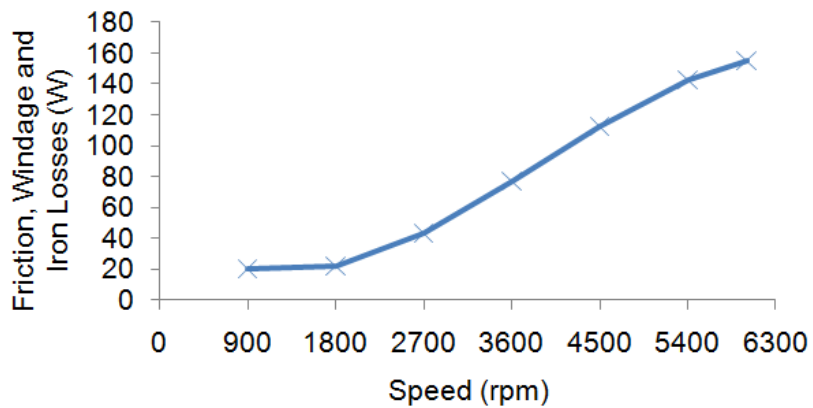


Fig 5.25 Summation of friction, windage and iron losses (Experiment)

According to Fig 5.24, the copper loss versus speed of the built machine is descending, as less torque and current is required in higher speeds. In addition, summation of friction, windage and iron loss is ascending as it is the function of the machine's speed, see Fig 5.25.

According to Fig 5.21, and Fig 5.24, the copper losses in experiments are smaller than their values in the simulation. This is because that the copper loss shown in Fig, 5.21 is for the ideal case that machine is providing 1kw in the simulation, while the built machine cannot support this much power and developed torque in experiments. So less current is drawn by machine in experiment compared to the simulation analysis.

To evaluate the performance of the built machine, it has been tested in various speeds and various load levels. In each test, the average of input power described by equation (5.4) and output power of the machine are measured and the efficiency of the machine is calculated for each operating point. See Fig 5.26.

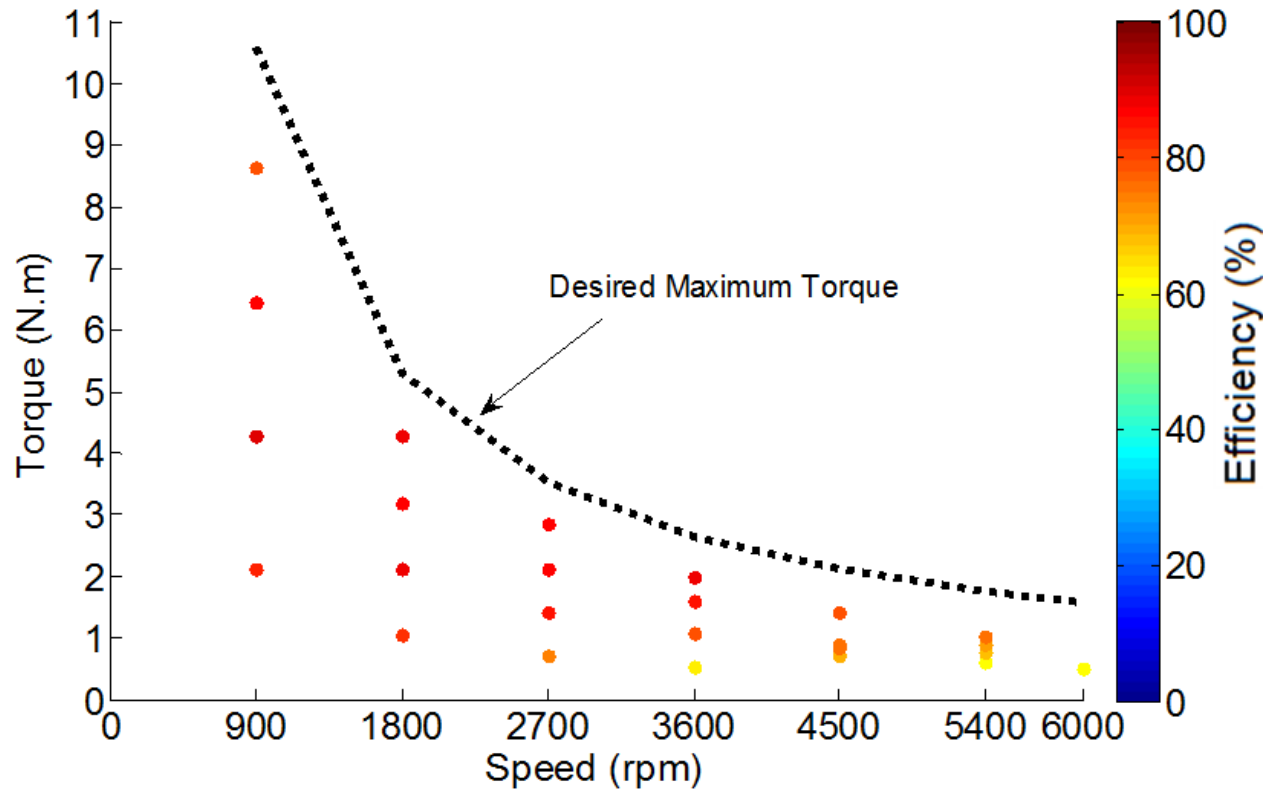


Fig 5.26 Efficiency assessment of the built machine in wide range of speeds and load levels (Experiment)

As is seen in Fig 5.26 the built machine can support the efficiency of more than 88% in wide range of speeds.

5.4 Dual Inverter Test Rig

After experimentally investigating the performance of the built machine in a Y-connected winding and only by one inverter in section 5.3, the phases of the built IPMSM are now arranged in an open winding structure, and a test rig is prepared to do the experimental analysis for this configuration.

There is no neutral point in the open winding IPMSM structure, so the existing machine has six leads comprised of two sets of three phase inputs. In this format, two inverters, called Main Bridge (MB) and Floating Bridge (FB), are used to feed the machine's phases which provides more voltage on the machine's windings and extends the machine's operating region. The dual inverter open winding IPMSM is shown by Fig 5.27.

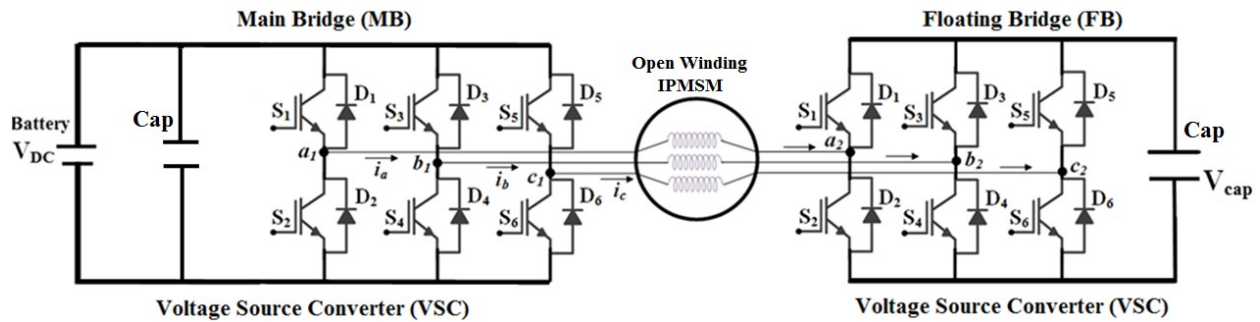


Fig 5.27 Dual inverter open winding IPMSM

The machine's actual structure showing two sets of MB and FB inputs is shown by Fig 5.28.

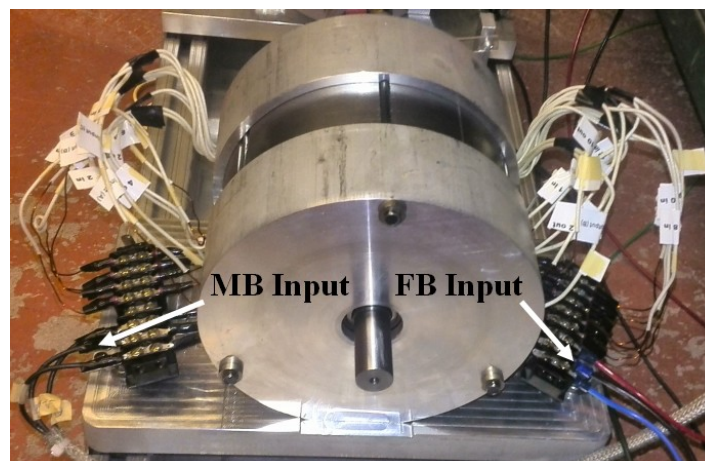


Fig 5.28 The Main Bridge (MB), and Floating Bridge (FB) inputs in the built machine

The schematic of the test rig system for the dual inverter drive tests is very similar to what has been shown for the single inverter system. The only difference is that another Semiteach unit is added to the other end of the open winding machine as the FB. The schematic depiction of the dual inverter system is shown by Fig 5.29.

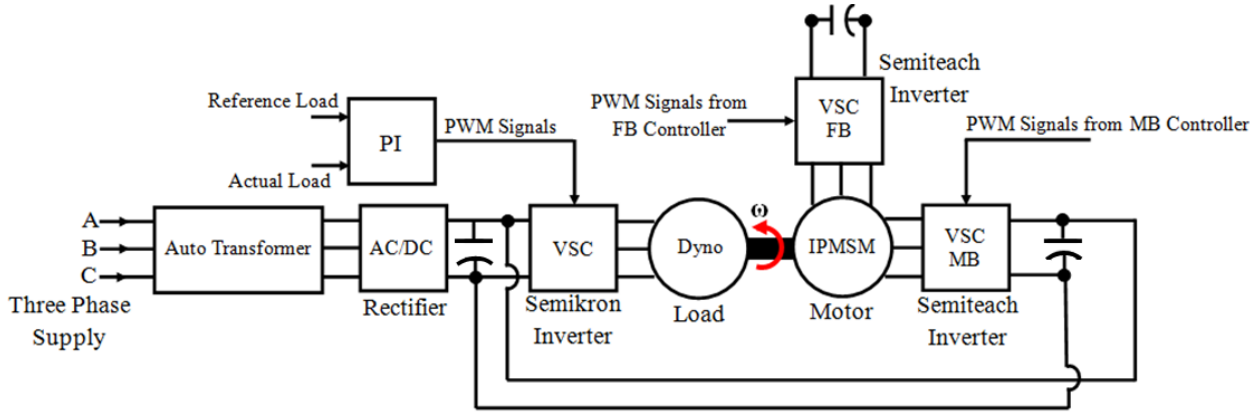


Fig 5.29 The schematic view of the system in dual inverter drive structure

The different parts of the test rig for the dual inverter drive studies are shown by Fig 5.30.

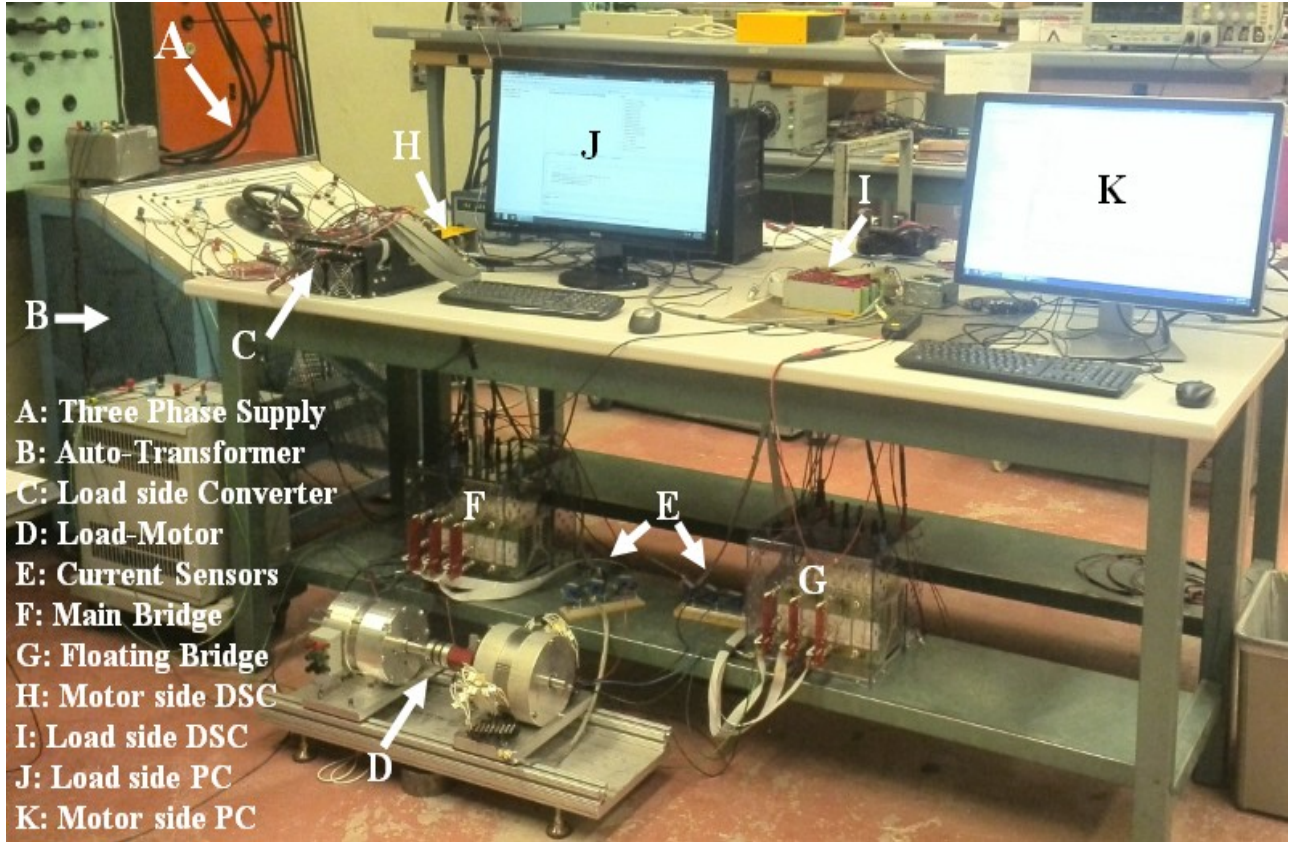


Fig 5.30 Complete test bench in lab for the dual inverter drive experiments

5.5 New Floating Bridge Control Technique

In Chapter 4, an initial controller has been proposed, and its capability is examined by simulation analysis. The introduced control method described in Chapter 4 presents two main disadvantages and weak points.

To begin with, the FB is activated after the maximum possible speed of the single inverter drive. This means that the FB is not employed in low speeds and, after a specific speed, it is added to the controller scheme to provide voltage on the machine's phases. Adding and activating the FB while the machine is working in speed such as 6000 rpm is a risky task and definitely causes the system to sense a disturbance and make the control susceptible to instability. Secondly, in the control approach studied in Chapter 4, FB voltage magnitude and angle are set using the rational function of d-axis and q-axis currents, and the FB vector is forced to be perpendicular to the current. Having any ripples on the current profiles or working in high speeds which require the low amplitude current may cause the rational function of d- and q- axis currents not to be a fixed number and result in an infinite number of combinations for FB voltage magnitude and angle. In simulation analysis, since i_d and i_q currents are DC, the unstable situation is not seen. However, in the experiments, the i_d and i_q currents are no longer DC as there exist some ripples and fluctuations on their profiles (See Fig 5.19(c)).

In order to solve the above mentioned problems, a new control scheme is proposed in the experiment. The different parts of the proposed controller have the following main duties:

Real power requirement of machine supported by the MB side: The MB is the part of the drive responsible for supporting the real power required by the IPMSM and does not contribute to reactive power requirement of the machine. So first the real power requirement of machine is calculated as follows:

$$P_{Demand} = \frac{3}{2}(v_{qm} i_q + v_{dm} i_d) \quad (5.5)$$

The real and reactive components of the MB voltage vector, assuming that only real power is supported by MB, are calculated as follow:

$$v_{q1A} = \frac{2}{3}(P_{Demand}) \times \frac{i_{qF}}{i_{mag}} \quad (5.6)$$

$$v_{d1A} = \frac{2}{3} (P_{Demand}) \times \frac{i_{dF}}{i_{mag}} \quad (5.7)$$

where, i_{qF} and i_{dF} are the q-axis and d-axis currents after being filtered by a low pass filter. i_{mag} is a function calculated as:

$$i_{mag} = i_{qF}^2 + i_{dF}^2 \quad (5.8)$$

Capacitor voltage controller for the FB side: Like the initial control method described in Chapter 4, a PI controller is used for the new control approach to keep the capacitor voltage at the desired value. As the MB and FB are assumed to be equal in rating, the capacitor reference voltage is set at equal to the DC link of MB which is 320VDC. The PI controller for the capacitor voltage control and its inputs and output are shown by Fig 5.31.

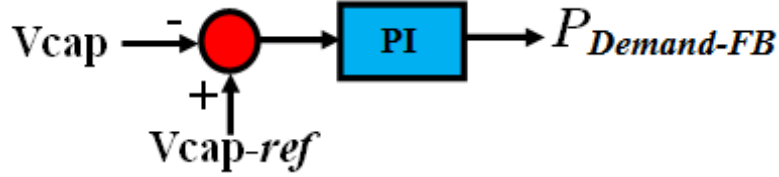


Fig 5.31 Inputs and output of capacitor voltage PI controller

Voltage components to keep the capacitor voltage at a safe and desired value: The output of the capacitor voltage PI controller is called $P_{Demand-FB}$ and is used for tuning the required q-axis and d-axis voltage components for capacitor voltage charging according to equations (5.9) and (5.10). For controlling the capacitor voltage, only real power flowing on the FB side is taken into account, so there is no reactive power flowing on the FB side for charging the capacitor and keeping it at the desired voltage.

$$v_{q-cap} = \frac{2}{3} (P_{Demand-FB}) \times \frac{i_{qF}}{i_{mag}} \quad (5.9)$$

$$v_{d-cap} = \frac{2}{3} (P_{Demand-FB}) \times \frac{i_{dF}}{i_{mag}} \quad (5.10)$$

MB d- and q-axes voltage components: The MB is the bridge that supports the entire real power requirements of the system, including the real power required for the machine and for the capacitor voltage regulation and control. Therefore, the real and reactive components of the MB vector are calculated according to the following equations:

$$v_{q1} = v_{q1A} + v_{q-cap} \quad (5.11)$$

$$v_{d1} = v_{d1A} + v_{d-cap} \quad (5.12)$$

FB d- and q-axes voltage components: The d-axis and q-axis voltage components of the machine can be obtained from the speed controller and the d-axis current controller. On the other hand, the d-axis and q-axis voltage components of MB have already been defined by equations (5.11) and (5.12). So the d-axis and q-axis voltage components of FB can be calculated by equations (5.13) and (5.14) taking into account the required voltage for keeping the capacitor charged.

$$v_{q2} = v_{q1} - v_{qm} + v_{q-cap} \quad (5.13)$$

$$v_{d2} = v_{d1} - v_{dm} + v_{d-cap} \quad (5.14)$$

As is seen, there is no equation or any constraint forcing the FB voltage vector to be perpendicular to the current. In a steady state and when the capacitor voltage is controlled and fixed on the desired value, the voltage of FB automatically becomes perpendicular to the current, and FB only supports the required reactive power of the system. In addition, both MB and FB are activated from zero speed to the high speed, and the required voltage of machine is shared between these two sources from the outset. This characteristic solves the problem of FB activation in high speed which is seen in the introduced controller described by Chapter 4.

The block diagram used in the experiments for the dual inverter drive structure based on the new control technique is shown by Fig 5.32.

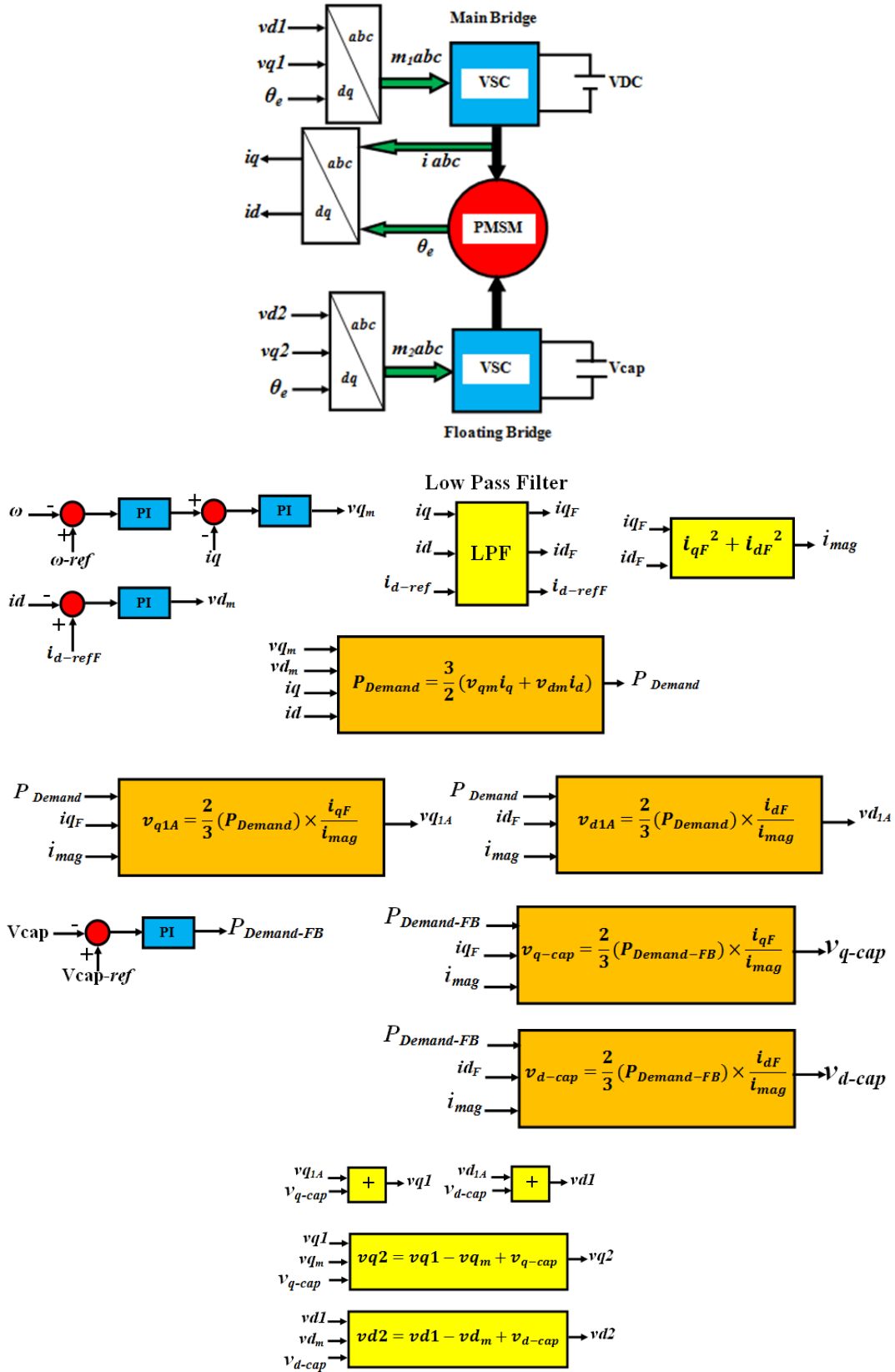
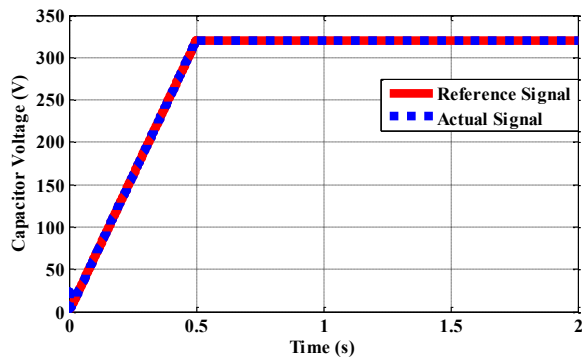


Fig 5.32 Block diagram used in experimental analysis for the dual inverter drive structure

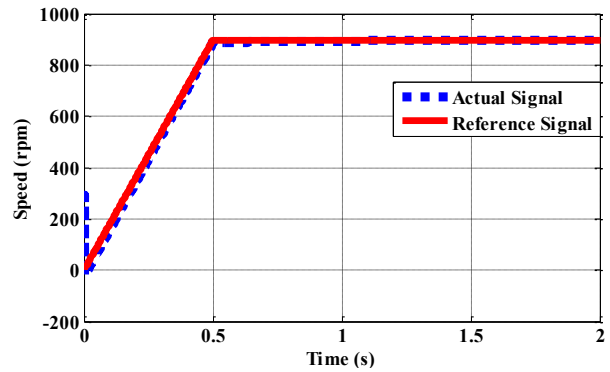
The built open winding IPMSM with the specification described in Table 5.1, is modeled by MATLAB/Simulink. The applicability of the new proposed controller is examined by a series of simulations using the block diagram in Fig 5.32. The simulation results for capacitor voltage control and speed control of the dual inverter open winding IPMSM in speeds of 900 rpm, 6300 rpm, and 8100 rpm are shown in Fig 5.33.

Table 5.1
Machine specifications for SIMULINK modeling and control

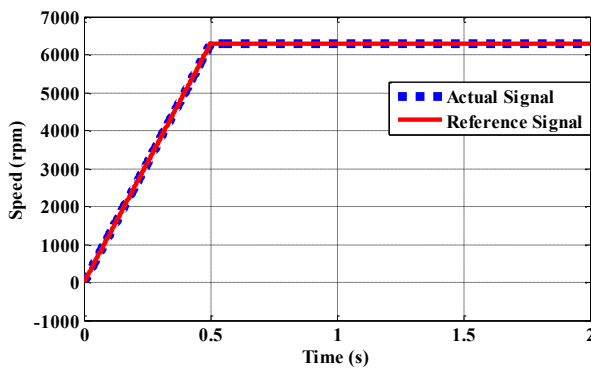
Parameter	Value	Parameter	Value
d-axis inductance (mH)	80	Phase resistance (Ω)	3.9
q-axis inductance (mH)	100	Flux linkage (Wb.N)	0.303
MB DC link (V)	320	FB Capacitor voltage (V)	320



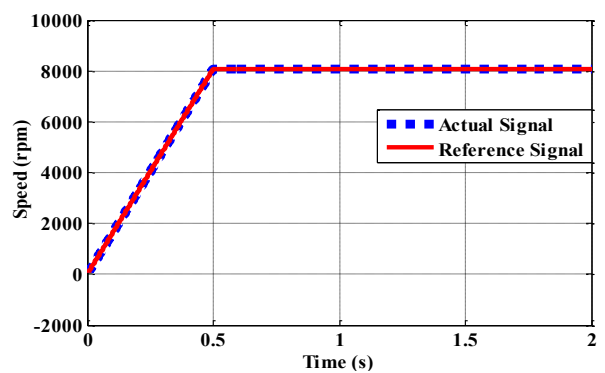
(a)



(b)



(c)



(d)

Fig 5.33 a) Capacitor voltage control, and the speed control in b) 900 rpm, c) 6300 rpm, d) 8100 rpm

The results presented by Fig 5.33 clearly show that the control approach is reliable in capacitor voltage control and speed control in rated power and in a wide range of speeds.

The modulating signals for the MB and FB plus the current flowing through the machine's phase in different speeds are shown by Fig 5.34. Fig 5.34 verifies that the MB and FB voltages are perpendicular and that the current is in phase with the MB voltage and perpendicular to the FB. It is worth noting that the modulation technique used in this thesis is SVM, so the peak of the MB and FB modulating signal can be 1.15 at most.

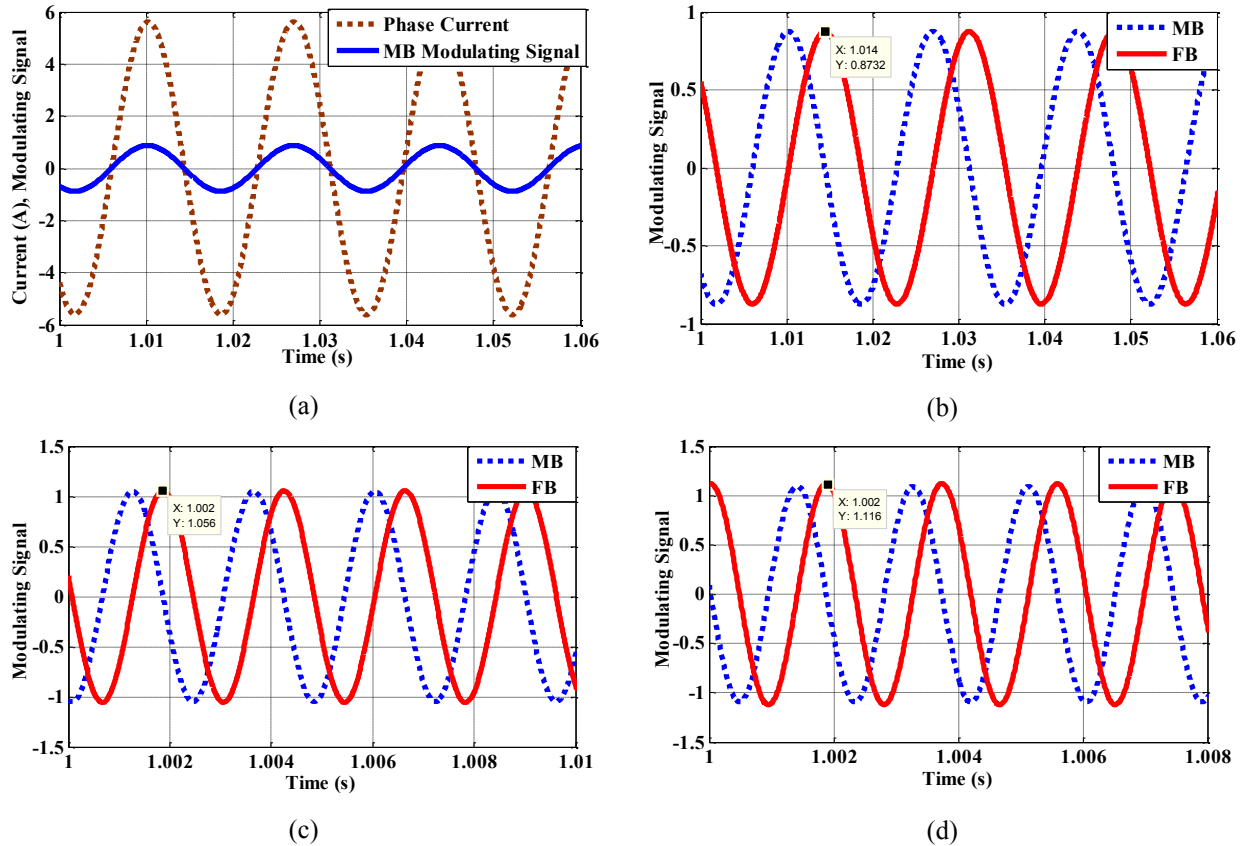


Fig 5.34 Simulated control signals, a) Phase current and the MB modulating signal in the rated power and 900 rpm, the MB and FB modulating signals in the rated power and speeds of b) 900 rpm, c) 6300 rpm, d) 8100 rpm

As is seen by Fig 5.34(a), the phase current and MB voltage are in phase, causing the MB to have unity power factor and only to support the real power of machine. According to Fig 5.34(b) and in 900 rpm and rated power, the i_d current has been tuned in a way that both MB and FB have the same voltages, and the controller automatically sets the FB only to support the reactive power of the machine and be perpendicular to the current and MB voltage. When the speed is increased, as is seen in Fig 5.34(c) and Fig 5.34(d), the MB and FB are still perpendicular, but their peaks increase up to their possible maximum values which are about 1.15. The simulation results show that none of the voltage and current constraints are disturbed and the machine can

support the rated power from base speed to up to 9 times base speed in the dual inverter drive structure.

The mechanical limitation is not taken into account in Simulink simulations that is often revealed in experiments. For instance, on some occasions, the coupling or torque transducer or other mechanical elements of the test rig are incapable of handling high speed performance and consequently prevent the system from working at such speeds. In order to show the controller's contribution without having the machine accelerate to very high speeds, the controller should be capable of supporting more power in the same speed compared to the single inverter drive. To verify this claim, the introduced dual inverter drive controller is used to support 1.3 times rated power (7A phase current) in the base speed while all the voltage and current limitations are taken into account. The phase current and modulating signal of the MB are shown by Fig 5.35(a), and the modulating signals of the MB and FB are presented by Fig 5.35(b).

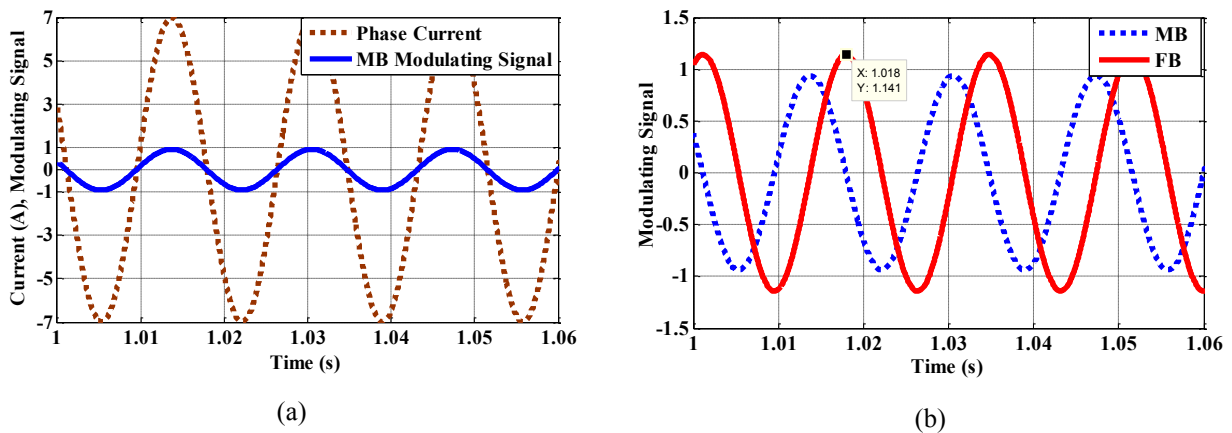


Fig 5.35 Simulated control signals, a) Phase current and modulating signal of the MB, b) Modulating signals for the MB and FB, in base speed and 1.3 times rated power

As is seen, the introduced dual inverter controller can support 1.3 times rated power in base speed without disturbing any current or voltage limitations. Again, MB voltage and phase current are in phase, and MB and FB voltages are perpendicular. i_d has been set in a way to tune the FB voltage magnitude be equal to 1.15.

Generally, the contribution of the introduced controller can be established by two means. First, it can extend the operating region of the machine to include its maximum speed. Second, it can show that the drive can support more power compared to the single inverter drive in the same speeds.

5.5.1 Experimental Investigations

To verify the simulations, experiments have been carried out to show the contribution of the dual inverter drive structure. Under the testing, vibrations were observed when the motor was operated at high speeds, therefore testing was limited to 7000 rpm at most. As a result, this study attempts to show the contribution of the dual inverter drive by extracting more power from the machine.

The most important characteristic of the introduced controller is that it can cause the MB and phase current to be in phase, and the FB to be perpendicular with the phase current. In this situation, the real power of the machine is supported by the MB, and its reactive power is supported by the FB. The MB PWM voltage, FB PWM voltage, phase current, and capacitor voltage in half load and 900 rpm are shown in Fig 5.36. The MB and FB signals are for line to line voltages which lead the phase current and phase voltage by 30 degrees. The MB PWM voltage signal and phase currents in high speeds of 4500 rpm, 5400 rpm and 6000 rpm in their maximum possible powers are shown in Fig 5.37. Experimental results described by Fig 5.37 verify the alignment of the MB voltage and phase current and the reliable performance of the controller in high speeds. The fundamental harmonic of the MB voltage leads the phase current by 30 degrees.

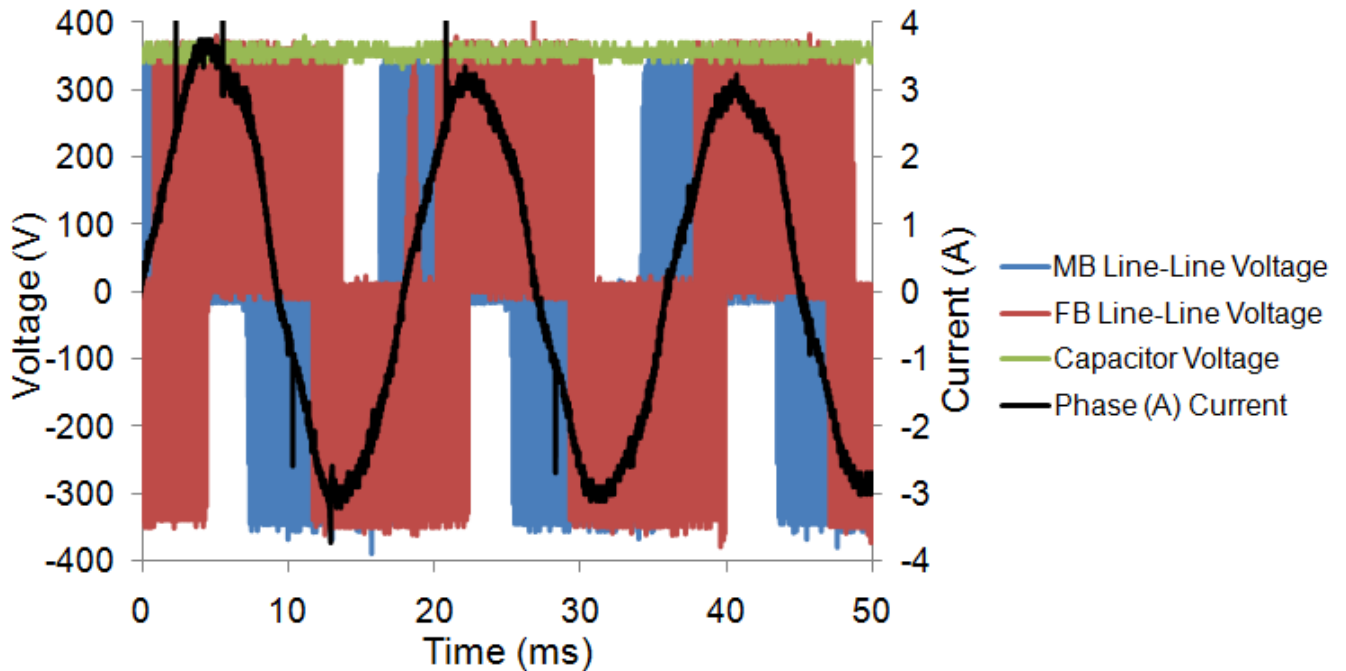
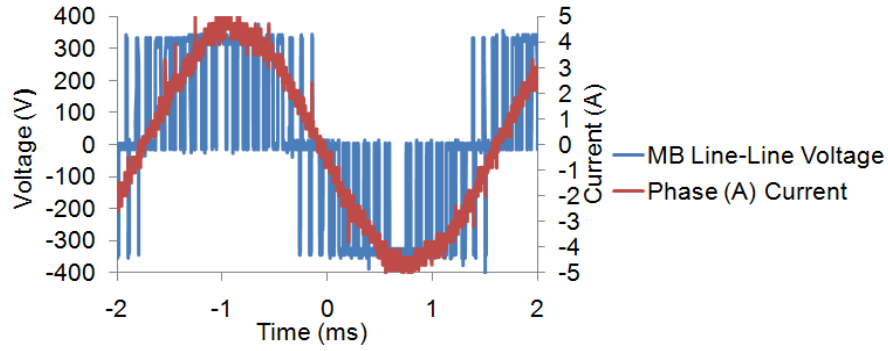
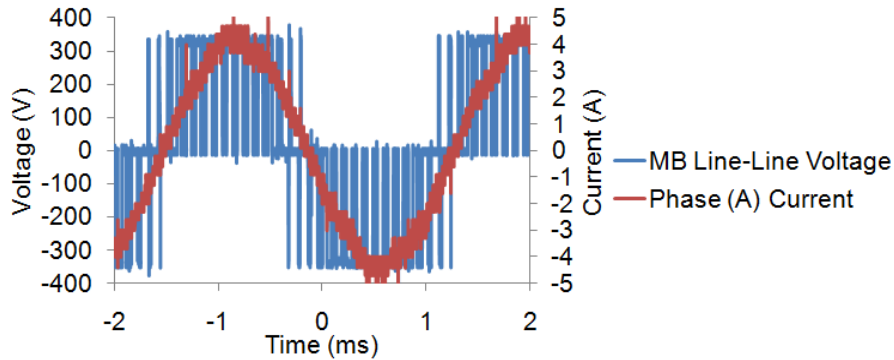


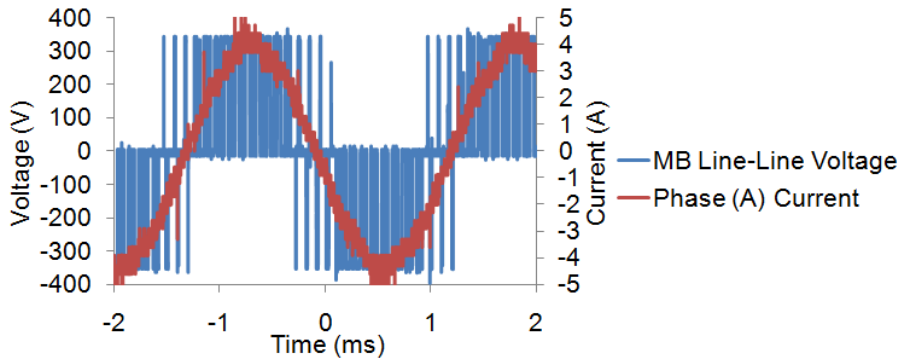
Fig 5.36 The MB voltage, FB voltage, phase current and capacitor voltage in 900 rpm



(a)



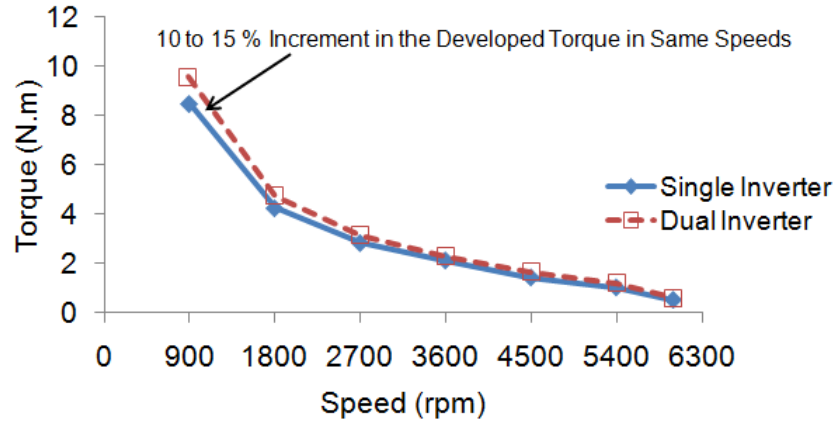
(b)



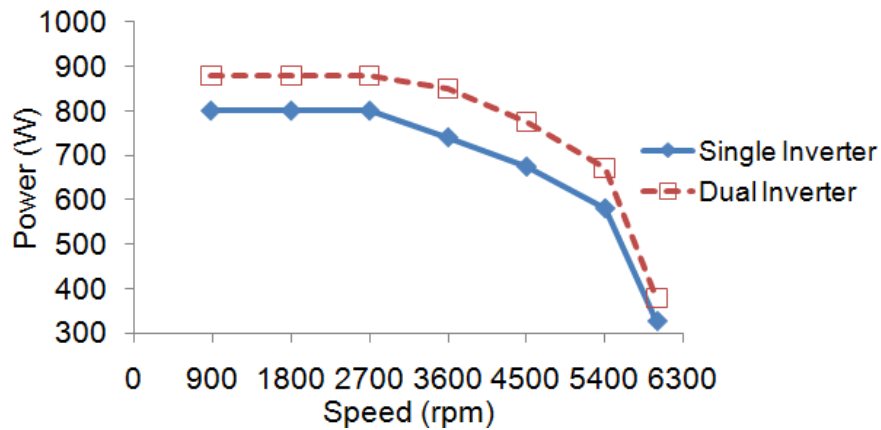
(c)

Fig 5.37 The MB Line to Line voltage (V_{ab}), and phase current in maximum possible power for a) 4500 rpm, b) 5400 rpm, c) 6000 rpm, the fundamental component of MB voltage leads current by 30 degrees

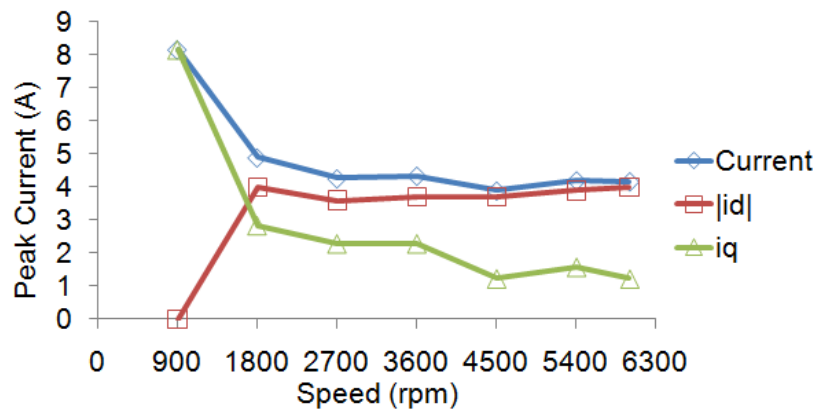
The introduced controller is employed in a wide range of speeds, and the i_d is set to minimum possible value and in a way that voltage and current limitations are not disturbed and more developed torque can be supported. The comparison between the developed torque and power in single inverter drive and in a dual inverter drive in a wide range of speeds is shown in Fig 5.38(a), and Fig 5.38 (b). The d- and q-axis currents in a wide speed range using the dual inverter drive are shown in Fig 5.38(c).



(a)



(b)



(c)

Fig 5.38 a) Developed torque for single and dual inverter drives, b) Output power for single and dual inverter drives
c) d- and q-axis currents for the dual inverter drive

As is seen in Fig 5.38(a) and Fig 5.38(b), when the introduced controller for the dual inverter drive is employed, at least 10 to 15% more developed torque and output power can be supported. The detailed comparison between the developed torques in single and dual inverter drives are presented by Table 5.2. One of the main reasons that more developed torque cannot be

supported is due to the losses in the FB side which consumes some of the injected real power supported by the MB side.

Table 5.2

Detailed comparison for the developed torques using single and dual inverter drives

Speed (rpm)	900	1800	2700	3600	4500	5400	6000
Developed Torque in Single Inverter (N.m)	8.65	4.29	2.85	1.99	1.44	1.04	0.52
Developed Torque in Dual Inverter (N.m)	9.56	4.73	3.15	2.27	1.66	1.2	0.6
Difference (%)	10.5	10.2	10.5	14	15.2	15.3	15.3

The current drawn in the dual inverter drive presented by Fig 5.38(c) is bigger than in the single inverter drive as the developed torque in the dual inverter drive is larger and more losses are associated with the FB. However, more voltage room is available on the machine's phases, supporting more developed torque and output power while taking into account the voltage and current limitations.

To find the efficiency profile, the output power is calculated by multiplying the speed and developed torque of the machine. The input power from the MB side is calculated using equation (5.4) and the circuit depicted in Fig 5.39. The average value of the input power is used for the efficiency assessment.

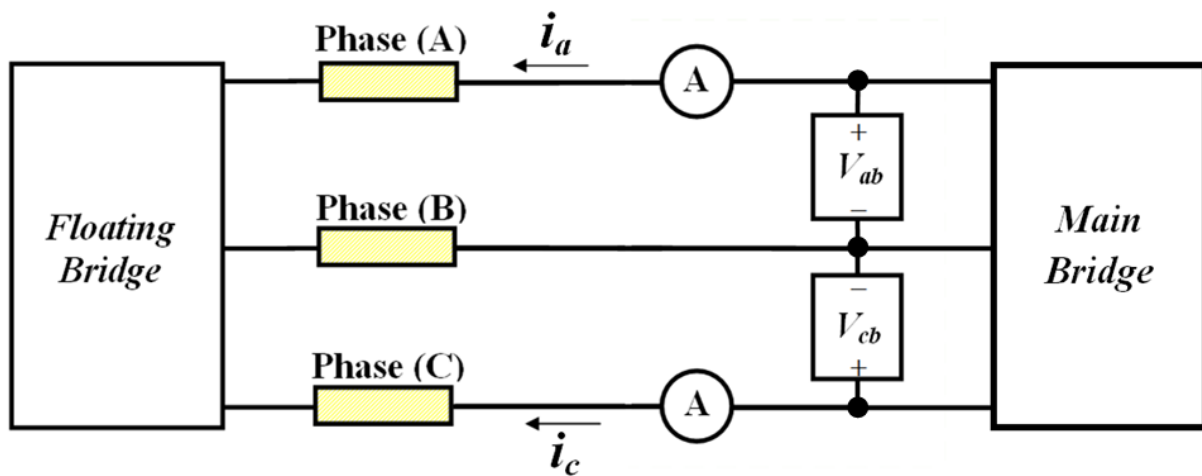


Fig 5.39 The circuit for the input power calculation from the MB side of view

As some examples, the input power measured by Fig 5.39 circuit and its average value (dashed line) for high speeds of 4500 rpm, 5400 rpm and 6000 rpm from the MB side are shown by Fig 5.40.

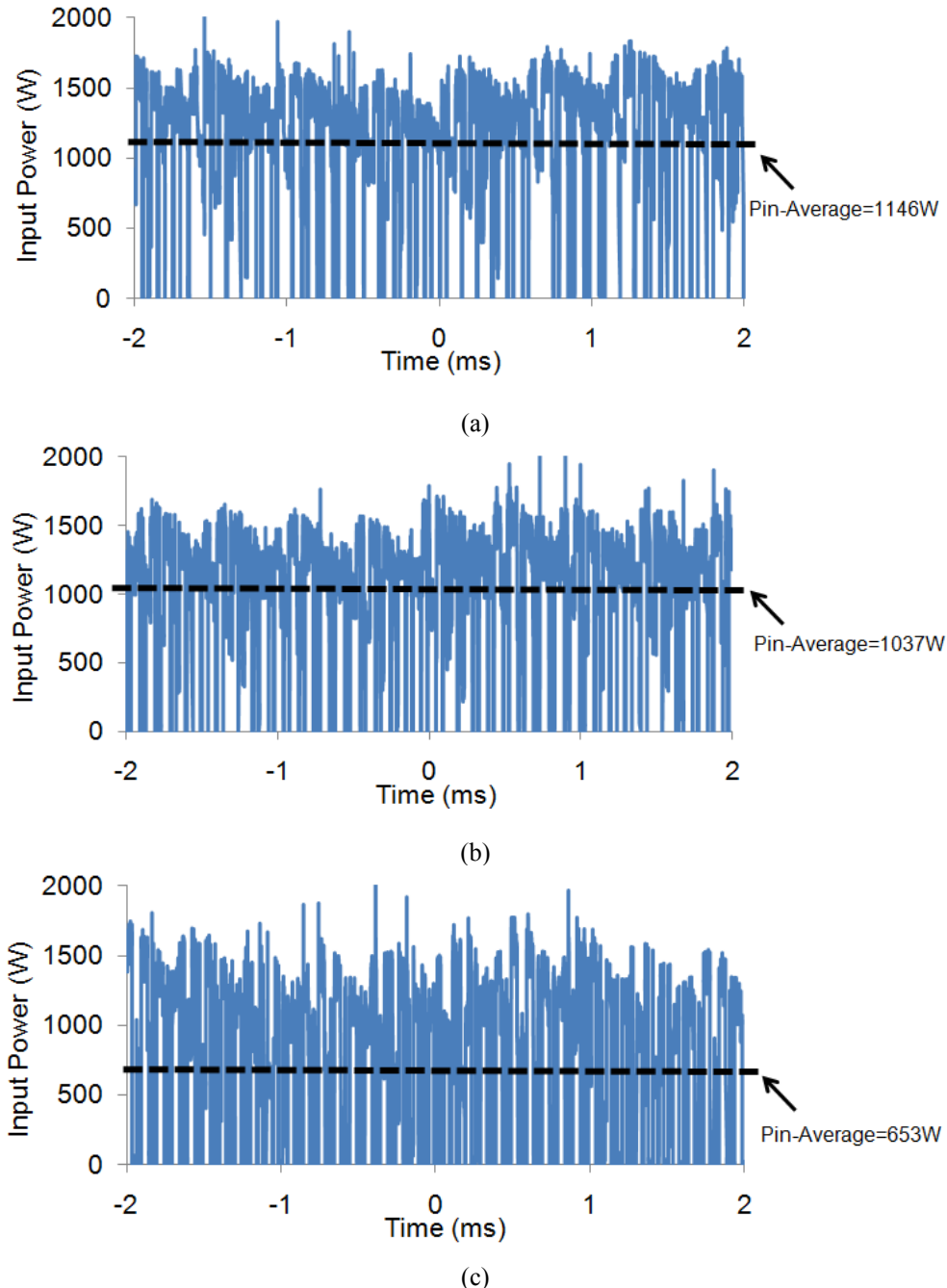


Fig 5.40 The input power signal from the MB side in a) 4500 rpm, b) 5400 rpm, and c) 6000 rpm

For the dual inverter open winding IPMSM, the efficiency analysis in different speeds and power levels using the average value of the input power and the actual value of output power is presented by Fig 5.41.

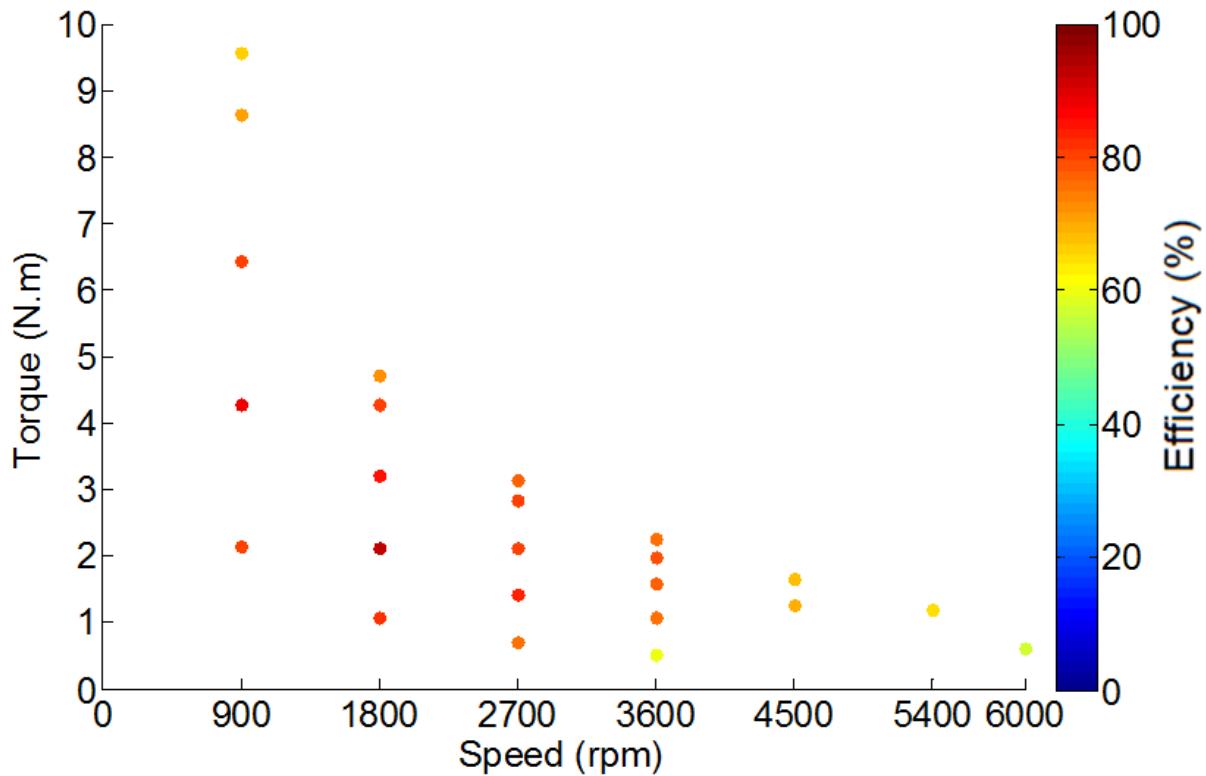


Fig 5.41 Efficiency assessment of the built machine in wide range of speeds and load levels from the MB side of view (Experiment)

According to the efficiency plot presented by Fig 5.41, the dual inverter drive system shows 92% peak efficiency. This peak efficiency is higher than that obtained with a single inverter drive, even though this efficiency measurement includes the additional losses in the floating bridge. In the maximum possible load level, the efficiency of the system is between 70% and 80% up to 6 times base speed. At some operating points, the efficiency of the dual inverter drive is lower than the single inverter drive at the same speed and load levels. This is due to the losses associated with using second converter on the FB side. The improvement in efficiency for the dual inverter drive structure is mainly the function of the specified reference i_d current which should be fulfilled in a careful and efficient way. If the i_d is not effectively tuned for the maximum efficiency extraction, the efficiency profile is not optimized for all speeds and power levels. The i_d values in each operating point have been tuned manually for both single and dual inverter drives, and there is an additional freedom in setting i_d as the winding voltage limit is relaxed. When setting the i_d values, the voltage and current limitations have been given the first priority while attempting to fulfill the highest possible efficiency.

5.6 Summary

The first contribution of this chapter is to describe the construction and test performance of the designed IPMSM in single and dual inverter drive structures. The second contribution is the proposal of a new control approach for the operating region extension of open winding IPMSMs and verifying this new approach by simulations and experiments.

The designed machine's different parts including its rotor, stator and magnets were drawn by the author and components obtained from external suppliers. The rotor and stator laminations were supplied by Proto Laminations Inc, and the magnets from Allstar Magnetics Company (both located in the U.S). Assembly of lamination stacks, welding of stator laminations and machining of the housing and rotor assembly were carried out in the Engineering machine shop at the University of Calgary, stator winding was carried out by a company in Calgary, AB, Canada. Final assembly of the machine, development of the test facility and implementation of the controller scheme in C language using a TI28335 microcontroller based Digital Signal Controller (DSC) was conducted by the author.

Results of a full series of experimental investigations are presented, namely: the Back-EMF voltage, inductance, loss analysis, torque capability, and speed range.

A number of differences between the results of the simulations and the outcome of the experiments are revealed. In terms of the Back-EMF voltage, the experimental verification shows that the permanent magnet flux density of the built machine is 10% smaller than in the simulations. In terms of inductance, the L_d of the built machine is larger than the L_d in the simulated IPMSM. However the L_q of both the built and simulated machines are very close. Although the discrepancies resulted in a smaller saliency for the built machine compared to the simulated one, a wide speed range of up to 6000 rpm or 6.66 times base speed is experimentally verified. The reasons of the differences between the performance and specifications of the designed machine and the built machine are covered in the chapter.

Subsequently, the built machine is prepared by changing its winding arrangement for use in an open winding configuration using a dual inverter drive. A new control technique is proposed and simulated for the dual inverter drive system. The simulation shows that the operating region including the maximum speed of the IPMSM can be extended in a dual inverter drive by a factor of 1.4. Although mechanical limitations prevented the test rig from being used in more than 7000

rpm, the contribution of dual inverter drive is verified by extracting more power in the same speed compared to the single inverter drive. The experiments reveal a 10 to 15% increment in power capability for the dual inverter drive structure. The exact power capability improvement in each operating point and speed is clearly included in the chapter's content. Part of the reason that more power could not be supported is due to the high losses associated with the Semiteach unit in the FB side. Still, the proposed control technique is easy to implement and has not been previously proposed by other research studies.

Chapter 6

CONCLUSIONS

The main concluding remarks, contributions and some suggestions for the future work are described in this chapter.

6.1 Conclusions and Contributions

The main objective of this thesis is to introduce a V-shaped magnet IPMSM to provide wide speed range operation. In order to fulfill this aim, different rotor geometry changes are applied to the structure of the IPMSM to increase the d-axis inductance of the final model while taking into account a promising saliency. Geometry changes affect the d- and q-axis paths magnetization and reluctance as well as the harmonic contents of the air-gap flux density profile for fulfilling the objectives. To extend the operating region and maximum speed of the final model IPMSM, its winding arrangement is changed to an open winding structure, and two VSCs are used to provide more voltages on the machine's phases using a dual inverter drive structure. The significant contributions of each chapter are summarized below.

It is shown by Chapter 2 that the speed range of an IPMSM is the function of the d-axis inductance of machine. The larger d-axis inductance causes the characteristic current of machine to be shifted into the current limitation circle. The geometry change is considered as a suitable approach for tuning the magnetization and inductance in d-axis path for the designed machine. The other alternative method to extend the speed range of the machine is to apply more voltage on the machine's phases. This alternative can be fulfilled using the IPMSM in an open winding structure and dual inverter drive in this thesis work. Briefly, the concentrated open winding PMSM design is introduced as a suitable option for wide range speed applications however a reliable and robust FB control scheme is needed to ensure the safe performance of the system.

The analytical approach is used in Chapter 3 to specify the slot pole combination and the dimensions of an IPMSM. A number of rotor geometry changes are applied to the physical structure of the machine in order to propose an initial IPMSM. These changes include the angle between the two pieces of magnets in a V-shaped magnet IPMSM (γ), the clearance between the two pieces of magnets, and the Magnet Pitch (MP). The geometry changes aim to adjust the d-

and q-axis magnetization and inductance and reducing the harmonics in the air-gap flux density. Widening the clearance and setting the magnet pitch to 85% are recommended to introduce a high d-axis inductance machine with low harmonic content Back-EMF profile. The $90^\circ \gamma$ V-Shaped magnet IPMSM is proposed as the initial model. More physical and material modifications and considerations are applied to the initial design to specify the final model with a wide speed range, low cogging torque, and low Back-EMF harmonic contents. For the final design of the IPMSM, the FEM simulations fulfill in the following: Seven times base speed operation, 3% THD in Back-EMF waveform, and less than 5% peak cogging torque. The final design uses the $75^\circ \gamma$, lower magnet flux density, and more reliable rotor and stator laminations compared to the initially designed IPMSM. Promising efficiency is presented in wide speed range verifying the reliable performance of the designed IPMSM. Thus, the main contribution of Chapter 3 is to prove how the geometry changes can be used to adjust the inductance of an IPMSM and affect its performance in a desired way.

The concept of open winding PMSMs and the vector diagram of this machine are presented in Chapter 4. An initial controller is introduced for the open winding PMSM using a dual inverter drive, and the performance of a PMSM is evaluated by Simulink simulation. Two VSCs are used for the open winding PMSM: one is responsible for real power injection, while the other converter, FB, is for the machine's reactive power compensation. Using two converters at the same time enables more voltage room on the machine's terminal, resulting in the extension of the operating region and maximum speed. A 41% extension in the operating region for the open winding PMSM is presented. The final design of the IPMSM presented in Chapter 3 is used in an open winding structure, and its performance is evaluated using the open winding PMSM vector diagram concepts. It is shown by the FEM simulations that the maximum speed of the IPMSM shifts from 6300 rpm up to 8800 rpm using the dual inverter drive structure. The loss and efficiency analysis are presented in Chapter 4 for a wide range of speeds, including single inverter and dual inverter drive modes of operation. More than 87% efficiency is still expected using the dual inverter drive. Thus, the contribution of Chapter 4 is to demonstrate how the operating region of an IPMSM can be extended by providing more voltage on the machine's phases using a controlled dual inverter drive.

Chapter 5 describes the experimental verifications of the FEM and Simulink simulations. The designed IPMSM is built and tested in normal Y-connected winding configuration using a single inverter drive and in an open winding configuration using a dual inverter drive. A 10% lower permanent magnet flux linkage is seen in the built machine compared to the simulation analysis. The L_d of the built machine is much bigger than the L_d in the simulated IPMSM. These two discrepancies cause lower torque density for the built IPMSM compared to the simulated IPMSM. However, a wide speed range operation up to 6000 rpm or 6.66 times base speed is verified experimentally for the built machine. Loss and efficiency analysis are presented in Chapter 5 taking into account the mechanical losses. The winding of the built machine is rearranged to be used in an open winding structure. A new control technique is proposed and is studied by Simulink simulations. In the proposed controller, the required real power of the machine is supported by the MB, and the required reactive power is supported by the FB. The proposed controller is easy to implement and does not use any rational or triangular functions of d-axis or q-axis currents for FB voltage magnitude and angle regulation. The proposed control technique is utilized in a wide speed range, and the experiment shows that a 10 to 15% output power improvement can be guaranteed by the dual inverter drive structure. Thus, the contribution of Chapter 5 is to verify the simulation expectations by constructing the designed model and testing it in the single and dual inverter drives as well as proposing a new control technique for the dual inverter fed open winding IPMSMs.

6.2 Suggestions

Some important suggestions can be considered for improving the results of this study.

To begin with, due to low LCM of 12 lost 8 pole machine, ripples are always evident on the generated developed torque of machine. Future research can investigate how these ripples can be reduced by implementing more design modifications or using a new control approach.

While this study applied specific rotor geometry changes to find the final model, other geometry changes or systematic methods for finding an optimal model can be studied further to elevate the contribution of this thesis.

Another area for further inquiry is losses. Thinner laminations with lower loss density can help the designed machine to have lower losses and higher efficiency. In addition, having more accurate loss data for the laminations can increase the reliability of the simulation results.

To obtain better and more precise experimental results, higher quality manufacturing of the different machine parts, and the provision of a tool such as a special fan for reducing the temperature of the machine in high load applications can be useful.

A further suggestion for the experimental stage is to have a more reliable load. Using a Mechanical Dynamometer instead of using another IPMSM as the load can be a better option as it does not have the associated problems for controlling. Having another electric machine as the load causes the control scheme of the test rig to be more complicated and sometimes cause unwanted physical interaction with the motor. In addition, the magnetic properties of the load machine may change during long term experiments which cause the loading of the tested motor to occasionally become harder and less efficient.

For the dual inverter drive experiments, having a lower loss converter for the FB side is helpful to elevate the contributions of the research.

With regard to both the single and dual inverter drive structures, the i_d values have been manually set taking into account the voltage limitation. Introducing an accurate method for finding the optimal i_d current trajectory to have maximized efficiency at different operating points of the single and dual inverter drive systems is highly recommended for future research work.

Finally, by applying these suggestions and improvements, the contributions of this thesis can also be employed in wider fields of application, such as in variable speed drive Hybrid Electric Vehicles (HEVs) and wind generation systems.

REFERENCES

- [1]. Di Pan, Feng Liang, Yang Wang, and Thomas A. Lipo, "Extension of The Operating Region of an IPM Motor Utilizing Series Compensation" IEEE Energy Conversion Congress and Exposition (ECCE), Pp: 823-830, 2012
- [2]. P.D. Chandana Perera, "Sensorless Control of Permanent Magnet Synchronous Motor Drives" Ph.D Thesis, Alborg University, 2002
- [3]. Rukmi Dutta, "A Segmented Interior Permanent Magnet Synchronous Machine with Wide Field Weakening Range" PhD Thesis, University of New South Wales, 2007
- [4]. R. Krishnan, "Electric Motor Drives Modeling, Analysis, and Control" Pearson Education, 2001
- [5]. B. K. Bose, "Modern Power Electronics and AC Drives" Prentice Hall, 2002
- [6]. B. K. Bose, "Power Electronics and Variable Frequency Drives" First edition, John Willey& Sons, 1996
- [7]. Ki-Doek Lee; Hyung-Woo Lee; Ju Lee; Won-Ho Kim, "Analysis of Motor Performance According to the Inductance Design of IPMSM" IEEE Trans on Magnetics, Vol: 51, Issue: 3, Article #: 8201204, 2015
- [8]. W. L. Soong and N. Ertugrul, "Field-weakening performance of interior permanent magnet motors," IEEE Transactions on Industry Applications, vol. 38, pp. 1251-1258, 2002.
- [9]. R. Dutta and M. F. Rahman, "Design and Analysis of an Interior Permanent Magnet (IPM) Machine With Very Wide Constant Power Operation Range," IEEE Trans on Energy Conversion, Vol. 23, pp. 25-33, 2008.
- [10]. Toyota, "Toyota hybrid system - THS II," Toyota Motor Corporation, Public Affairs Division, Tokyo, Japan2003.
- [11]. D. P. Kothari, I. J. Nagrath, "Electric Machines" Third edition, The McGraw Hill Publishing Company, 2004
- [12]. A. E. Fitzgerald, "Electric Machinery" McGraw Hill Publishing Company, 1992
- [13]. M. E. El-Hawary, "Electrical Energy Systems" CRC Press 2000
- [14]. Enrique L. Carrillo Arroyo, "Modeling and Simulation of Permanent Magnet Synchronous Motor Drives System" M.Sc Thesis, University of Puerto Rico, 2006
- [15]. Lester Chong, "Design of an Interior Permanent Magnet Machine with Concentrated Windings for Field Weakening Applications" PhD Thesis, University of New South Wales, 2011
- [16]. Calin Capitan, "Torque Control in Field Weakening Mode" M. Sc Thesis, Alborg University 2009
- [17]. Jan Persson, "Innovative Standstill Position Detection Combined with Sensorless Control of Synchronous Motors" Ecole Polytechnique Federale De Lausanne, M. Sc Thesis, 2005

- [18]. Sung-Yoon Jung; Chunting Chris Mi; Kwanghee Nam, “Torque Control of IPMSM in the Field-Weakening Region With Improved DC-Link Voltage Utilization” IEEE Trans on Industrial Electronics, Vol: 62, Issue: 6, Pp: 3380-3387, 2015
- [19]. Luke Dosiak, and Pragasen Pillay, “Cogging Torque Reduction in Permanent Magnet Machines” IEEE Trans on Industry Applications, Vol: 43, No: 6, Pp: 1565-1571, 2007
- [20]. J. Kolehmanien, J. Ikaheimo, “Motors with Buried Magnets for Medium-Speed Applications” IEEE Trans on Energy Conversion, Vol: 23, No: 1, Pp: 86-921, 2008
- [21]. H. Murakami, Y. Honda, H. Kiriya, et al, “The Performance Comparison of SPMSM, IPMSM, SynRM, in use as Air-Conditioning Compressor” IEEE 34th IAS Annual Meeting, Vol: 2, Pp: 840-845, 1999
- [22]. S. Morimoto, M. Sanada, and Y. Takeda, "Wide-speed operation of interior permanent magnet synchronous motors with high-performance current regulator," IEEE Trans on Industry Applications, vol. 30, pp. 920-926, 1994.
- [23]. W. L. Soong, T. J. E Miller, “ Field Weakening Performance of Brushless Synchronous AC Motor Drives” IEE Proc-Electr, Power Appl, Vol: 141, No: 6, 1994
- [24]. M. S. Toulabi, J. Salmon, A. Knight, “Design and Performance Assessment for the V-Shaped Magnet IPM Synchronous Motor” IEEE International Electric Machines and Drives Conference (IEMDC), Pp: 214-219, 2015
- [25]. X. Liu, H. Chen, J. Zhao, A. Belahcen, “Research on the Performance and Parameters of Interior PMSM Used for Electric Vehicles” IEEE Trans on Industrial Electronics, Early Access, 2016
- [26]. L. Yue, P. Yulong, Y. Yanjun, S. Yanwen, C. Feng, “Increasing the Saliency Ratio of Fractional Slot Concentrated Winding Interior Permanent Magnet Synchronous Motors” IET Electric Power Applications, Vol: 9, Issue: 7, Pp: 439-448, 2015
- [27]. Sung-Li Kim, Young Kyoum Kim, Geun Ko Lee, and Jung Pyo Hong, “ A Novel Rotor Configuration and Experimental Verification of Interior PM Synchronous Motor for High-Speed Applications” IEEE Trans on Magnetics, Vol: 48, No: 2, Pp: 843-846, 2012
- [28]. Katteden Kamiev, Juho Montonen, Mahendarkar Prabhakaran Ragavendra, et al, “ Design Principles of Permanent Magnet Synchronous Machines for Parallel Hybrid or Traction Applications” IEEE Trans on Industrial Electronics, Vol: 60, No: 11, Pp: 4881-4890, 2013
- [29]. L. Chong, R. Dutta, M. F. Rahman, “Field Weakening Performance of a Concentrated Wound PM Machine with Rotor and Magnet Geometry Variation” IEEE Power and Energy Society General Meeting, Pp: 1-4, 2010

- [30]. Mi-Jung Kim, Su-Yeon Cho, Ki-Doek Lee, et al, “ Torque Density Elevation in Concentrated Winding Interior PM Synchronous Motor with Minimized Magnet Volume” IEEE Trans on Magnetics, Vol: 49, No: 7, Pp: 3334-3337, 2013
- [31]. P. M. Lindh, P. Immonen, Y. Alexandrova et al, “The Design of Rotor Geometry in a Permanent Magnet Traction Motor for a Hybrid Bus” IEEE International Conference on Electrical Machines (ICEM), Pp: 310-315, 2014
- [32]. Rukmi Dutta, Lester Chong, and M. F. Rahman, “Design and Experimental Verification of an 18 Slot/14 pole Fractional Slot Concentrated Winding Interior Permanent Magnet Machine” IEEE Trans on Energy Conversion, Vol: 28, No: 1, Pp:181-190, 2013
- [33]. Rahman, S. A, Vaseghi, B. Knight, A. M, “Influence of Rotor Magnet Variations in Concentrated Winding IPMSM” IEEE XXth International Conference on Electrical Machines (ICEM), Pp: 315-320, 2012
- [34]. Janne Nerg, Marko Rilla, Vesa Ruuskanen, et al, “Direct Driven Interior Magnet Permanent Magnet Synchronous Motors for a Full Electric Sports Car” IEEE Trans on Industrial Electronics, Vol: 61, No: 8, Pp:4286-4294, 2014
- [35]. Rukmi Dutta, and M. F. Rahman, “Design and Analysis of an Interior Permanent Magnet (IPM) Machine with Very Wide Constant Power Operation Range” IEEE Trans on Energy Conversion, Vol: 23, No: 1, Pp: 25-33, 2008
- [36]. P. Jaatinen, R. P. Jastrzebski, H. Sugimoto et al, “Optimization of the Rotor Geometry of a High Speed Interior Permanent Magnet Bearingless Motor with Segmented Magnets” IEEE International Conference on Electrical Machines and Systems (ICEMS), Pp: 962-967, 2015
- [37]. Massimo Barcaro, Nicola Bianchi, and Freddy Magnussen, “Rotor Flux Barrier Geometry Design to Reduce Stator Iron Losses in Synchronous IPM Motors Under FW Operations” IEEE Trans on Industry Applications, Vol: 46, No: 5, Pp: 1950-1958, 2010
- [38]. Luigi Alberti, Massimo Barcaro, Michele Dai Pre, et al, “IPM Machine Drive Design and Tests for an Integrated Starter-Alternator Application” IEEE Trans on Industry Applications, Pp: 993-1001, 2010
- [39]. Piergiorgio Alotto, Massimo Barcaro, Nicola Bianchi, and Massimo Guarnieri, “Optimization of Interior PM Motors with Machaon Rotor Flux Barriers” IEEE Trans on Magnetics, Vol: 47, No: 5, Pp: 958-961, 2011
- [40]. Huang, Z, Huang, X, Zhang, J, et al, “Design of an Interior Permanent Magnet Synchronous Traction Motor for High Speed Railway Applications” IEEE 6th International Conference on Power Electronics, Machines, and Drives (PEMD), Pp: 1-6, 2012

- [41]. Konstantinos I. Laskaris , and Antonios G. Kladas, “Optimal Power Utilization by Adjusting Torque Boost and Field Weakening Operation in Permanent Magnet Traction Motors” IEEE Trans on Energy Conversion, Vol: 27, No: 3, Pp: 615-623, 2012
- [42]. B. N. Chaudhari, B. G. Fernandes, S. K. Pillai, “A new Hybrid Geometry for Permanent Magnet Synchronous Motor” IEEE Inetrantional Conference on Power Electronic Drives and Energy Systems for Industrial Growth, Pp: 260-263, 1998
- [43]. Pavel Ponomarev, Ilya Petrov, Nicola Bianchi, Juha Pyrhonen, “Selection of Geometric Design Variables for Fine Numerical Optimization of Electrical Machines” IEEE Trans on Magnetics, Vol: 51, Issue: 12, Article#: 8114808, 2015
- [44]. Gurakuq Dajaku, Wei Xie, and Dieter Gerling, “Reduction of Low Space Harmonics for the Fractional Slot Concentrated Windings using a Novel Stator Design” IEEE Trans on Magnetics, Vol: 50, No: 5, Article No:#8201012, 2014
- [45]. Hung Vu Xuan, Domenico Lahaye, Henk Polinder, et al, “Influence of Stator Slotting on the Performance of Permanent Magnet Machines with Concentrated Windings” IEEE Trans on Magnetics, Vol: 49, No: 2, Pp: 929-938, 2013
- [46]. Luigi Alberti, Massimo Barcaro, and Nicola Bianchi, “Design of a Low Torque Ripple Fractional Slot Interior Permanent Magnet Motor” IEEE Trans on Industry Applications, Vol: 50, No: 3, Pp: 1801-1808, 2014
- [47]. Patel. B. Reddy, Ayman. M. EL-Refaie, and Kum-Kang Huh, “Effect of Number of Layers on Performance of Fractional Slot Concentrated Windings Interior Permanent Magnet Machines” IEEE 8th International Conference on Power Electronics, ECCE Asia, Pp: 1921-1928, 2011
- [48]. Luigi Alberti, Emanuele Fornasiero, and Nicola Bianchi, “Impact of the Rotor Yoke Geometry on Rotor Losses in Permanent Magnet Machines” IEEE Trans on Industry Applications, Vol: 48, No: 1, Pp: 98-105, 2012
- [49]. Evangelos M. Tsampouris, Minos E Beniakar, and Antonios G. Kladas, “Geometry Optimization of PMSMs Comparing Full and Fractional Pitch Winding Configurations for Aerospace Actuation Applications” IEEE Trans on Magnetics, Vol: 48, No: 2, Pp: 943-946, 2012
- [50]. Radoslaw Nalepa, and Teresa Orłowska-Kowalska, “Optimum Trajectory Control of the Current Vector of a Nonsalient Pole PMSM in the Field Weakening Region” IEEE Trans on Industrial Electronics, Vol: 59, No: 7, Pp: 2867-2876, 2012
- [51]. David Stojan, Dusan Drevensek, Zeljke Plantic, et al, “Novel Field Weakening Control Scheme for Permanent Magnet Synchronous Machines Based on Voltage Angle Control” IEEE Trans on Industry Applications, Vol: 48, No: 6, Pp: 2390-2401, 2012

- [52]. Yuan Zhang, Longya Xu, Mustafa K. Guven, et al “ Experimental Verification of Deep Field Weakening Operation of a 50-kW IPM Machine by Using Single Current Regulator” IEEE Trans on Industry Applications, Vol: 47, No: 1, Pp: 128-135, 2011
- [53]. Shiyong Duan, Libing Zhou, and Jin Wang, “Flux Weakening Mechanism of Interior Permanent Magnet Synchronous Machines with Segmented Permanent Magnets” IEEE Trans on Applied Superconductivity, Vol: 24, No: 3, Article No: 0500105, 2014
- [54]. Pia Lindh, Juho Montonen, Paula Immonen, et al, “Design of a Traction Motor with Tooth Coil Windings and Embedded Magnets” IEEE Trans on Industrial Electronics, Vol: 61, No: 8, Pp: 4306-4314, 2014
- [55]. Kou Baoquan, Li Chunyan, and Cheng Shukang, “ Flux Weakening Characteristics Analysis of a New Permanent Magnet Synchronous Motor Used for Electric Vehicles” IEEE Trans on Plasma Science, Vol: 39, No: 1, Pp: 511-515, 2011.
- [56]. Tassarolo, A. Mezzarobba, M. and Menis, R, “A Novel Interior Permanent Magnet Motor Design with a Self-Activated Flux Weakening Device for Automotive Applications” IEEE 20th International Conference on Electrical Machines (ICEM), Pp: 2603-2609, 2012
- [57]. Matthias Preindl, and Silverio Bolognani, “Optimal State Reference Computation with Constrained MTPA Criterion for PM Motor Drives” IEEE Trans on Power Electronics, vol: 30, no: 8, Pp: 4524-4535, 2015
- [58]. Hae-Joong Kim, Do-Jin Kim, and Jung-Pyo Hong, “Characteristic Analysis for Concentrated Multiple Layer Winding Machine With Optimum Turn Ratio” IEEE Trans on Magnetics, Vol: 50, No: 2, Article No: #7019504, 2014
- [59]. Aymen M. EL-Refaie, “Fractional Slot Concentrated Windings Synchronous Permanent Magnet Machines: Opportunities and Challenges” IEEE Trans on Industrial Electronics, Pp: 107-121, 2010
- [60]. S. A. Rahman “Performance and Core Loss validation of Concentrated Winding IPMSM with Different Core Treatments” PhD Thesis, University of Alberta, 2014
- [61]. Aymen M. EL-Refaie, and Thomas M. Jahns, “Optimal Flux Weakening in Surface PM Machines Using Fractional Slot Concentrated Windings” IEEE Trans on Industry Applications, Vol: 41, No: 3, Pp:790-800, 2005
- [62]. Magnussen F, and Sadarangani C, “Winding Factors and Joule Losses of Permanent Magnet Machines with Concentrated Windings” IEEE Electric Machines and Drive Conferences (IEMDC), Vol: 1, Pp: 333-339, 2003

- [63]. Sari Maekawa, Kazuaki Yuki, Makoto Matsushita, et al, "Study of the Magnetization Method Suitable for Fractional Slot Concentrated Winding variable Magnetomotive Force Memory Motor" IEEE Trans on Power Electronics, Vol: 29, No: 9, Pp: 4877-4887, 2014
- [64]. L. Chong, and M. F. Rahman, "Saliency Ratio Derivation and Optimization for an Interior Permanent Magnet Machine with Concentrated Windings using Finite Element Analysis" IET Electric Power Applications, Vol: 4, Issue: 4, Pp: 249-258, 2009
- [65]. Barbara Boazzo, Gianmario Pellegrino, and Alfredo Vagati, "Multipolar SPM Machines for Direct Drive Application: A General Design Approach" IEEE Trans on Industry Applications, Vol: 50, No: 1, Pp: 327-337, 2014
- [66]. Magnussen. F, Thellin. P, and Sadarangani. C, "Performance Evaluation of Permanent Magnet Synchronous Machines with Concentrated and Distributed Windings Including the Effect of Filed Weakening" IEEE 2nd International Conference on Power Electronics, Machines and Drives, (PEMD), Pp: 679-685, 2004
- [67]. Rukmi Dutta, M. F. Rahman, and Lester Chong, "Winding Inductances of an Interior Permanent Magnet (IPM) Machine with Fractional Slot Concentrated Winding" IEEE Trans on Magnetics, Vol: 48, No: 12, Pp: 4842-4849, 2012
- [68]. Patel B. Reddy, Kum-Kang Huh, Ayman M. EL-Refaie, "Generalized Approach of Stator Shifting in Interior Permanent Magnet Machines Equipped with Fractional Slot Concentrated Windings" IEEE Trans on Industrial Electronics, Vol: 61, No: 9, Pp: 5035-5046, 2014
- [69]. Shi-Uk Chung, Jong-Moo Kim, Dae-Hyun Koo, et al, "Fractional Slot Concentrated Winding Permanent Magnet Synchronous Machine with Consequent Pole Rotor for Low Speed Direct Drive" IEEE Trans on Magnetics, Vol: 48, No: 11, Pp: 2965-2968, 2012
- [70]. Peter Sergeant, Alex P.M Van den Bossche, "Influence of the Amount of Permanent Magnet Material in Fractional Slot Permanent Magnet Synchronous Machines" IEEE Trans on Industrial Electronics, Vol: 61, No: 9, Pp: 4979-4989, 2014
- [71]. Phi Hung Nguyen, Hoang. E, Gabsi. M, and Kobylanski . L, "Permanent Magnet Synchronous Machines: Performances During Driving Cycles for a Hybrid Electric Vehicle Application" IEEE International Symposium on Industrial Electronics (ISIE), Pp: 1432-1438, 2010
- [72]. Reddy, P. B, EL-Refaie, A. M, and Huh, K. K, "Effect of Number of Layers on Performance of Fractional Slot Concentrated Windings Interior Permanent Magnet Machines" IEEE Trans on Power Electronics, Vol: 30, Issue: 4, Pp: 2205-2218, 2015
- [73]. Pia Salminen, "Fractional Slot Permanent Magnet Synchronous Motors For Low Speed Applications" PhD Thesis, Lappeenranata University of Technology, 2004

- [74]. Jeong Phil Lee, Sang Chul Han, Young Hee Han, and Tae Hyun Sung, "Loss Characteristics of SFES with Amorphous Core for PMSM" IEEE Trans on Applied Superconductivity, Vol: 21, No: 3, Pp:1489-1492, 2011
- [75]. Massimo Barcaro, and Nicola Bianchi, "Air Gap Flux Density Distortion and Iron Losses in Anisotropic Synchronous Motors" IEEE Trans on Magnetics, Vol: 46, No: 1, Pp:121-126, 2010
- [76]. Xinghe Fu, Xiangjun Li, Da Xu, and Mingyao Lin, "Iron Loss in Permanent Magnet Inductor Hybrid Excitation Synchronous Generator" IEEE Trans on Magnetics, Vol: 50, No: 1, Article No: #4002504, 2014
- [77]. Simon Steenjes, Georg von Pfingsten, Marco Hombitzer, and Kay Hameyer, "Iron Loss Model with Consideration of Minor Loops Applied to FE Simulations of Electrical Machines" IEEE Trans on Magnetics, Vol: 49, No: 7, Pp: 3945-3948, 2013
- [78]. Jiabin Wang, Taib Ibrahim, and David Howe, "Prediction and Measurement of Iron Loss in a Short Stroke Single Phase Tubular Permanent Magnet Machine" IEEE Trans on Magnetics, Vol: 46, No: 6, Pp: 1315-1318, 2010
- [79]. Katsumi Yamazaki, and Noriaki Fukushima, "Iron Loss Modeling for Rotating Machines: Comparison Between Bertotti's Three Term Expression and 3D Eddy Current Analysis" IEEE Trans on Magnetics, Vol: 46, No: 8, Pp: 3121-3124, 2010
- [80]. Katsumi Yamazaki, and Yusuke Kato, "Iron Loss Analysis of Interior Permanent Magnet Synchronous Motors by Considering Mechanical Stress and Deformation of Stators and Rotors" IEEE Trans on Magnetics, Vol: 50, No: 2, Article No: #7022504, 2014
- [81]. Lorenz. J, "Electrical Machine Iron Loss Prediction-A Unique Engineering Approach Utilizing Transient Finite Element Methods-Part II: Application and Validation" IEEE Trans on Industry Applications, Vol: 50, Issue: 4, Pp: 2871-2875, 2014
- [82]. Radu Fratila, Abdelkader Benabou, Abdelmounaim Touzi, and Jean Claude Mipo, "Nonlinear Modeling of Magnetization Loss in Permanent Magnets" IEEE Trans on Magnetics, Vol: 48, No: 11, Pp: 2957-2960, 2012
- [83]. Katsumi Yamazaki, and Noriaki Fukushima, "Iron Loss Model for Rotating Machines Using Direct Eddy Current Analysis in Electrical Steel Sheets" IEEE Trans on Energy Conversion, Vol: 25, No: 3, Pp: 633-641, 2010
- [84]. K. Akatsu, K. Narita, Y. Sakashita, and T. Yamada, "Characteristics comparison between SPMSM and IPMSM under high flux density condition by both experimental and analysis results," International Conference on Electrical Machines and Systems (ICEMS), Pp. 2848-2853. 2008

- [85]. "Advanced MotorTech, LLC: Short Course on the Design of Interior Permanent Magnet and Brushless DC Machines- Taking Theory to Practice," May 2010.
- [86]. Juha Pyrhonen, Tapani Jokien, and V. Hrabovcova, Design of Rotating Electrical Machines: John Wiley & Sons, Ltd., 2008.
- [87]. A. Emadi, Energy-Efficient Electric Motors, Third ed. New York: Marcel Dekker, Inc., 2005.
- [88]. Shin Myung Jung, Jin Sil Park, Hag Wone Kim, et al, "An MRAS Based Diagnosis of Open Circuit Fault in PWM Voltage Source Inverters for PM Synchronous Motor Drive Systems" IEEE Trans on Power Electronics, Vol: 28, No: 5, Pp: 2514-2526, 2013
- [89]. H. W. van der Broeck; H. -C. Skudelny; G. V. Stanke, "Analysis and Realization of a Pulse Width Modulator based on Voltage Space Vectors" IEEE Trans on Industry Applications, Vol: 24, Issue: 1, Pp: 142-150, 1988
- [90]. B. A. Welchko "A Double Ended Inverter System for the Combined Propulsion and Energy Management Functions in Hybrid Vehicles with Energy Storage" IEEE 31st Annual Industrial Electronics Society Conference (IECON), Pp: 1401-1406, 2005
- [91]. Brian A. Welchko, and James M. Nagashima, "The Influence of Topology Selection on the Design of EV/HEV Propulsion Systems" IEEE Power Electronics Letters, Vol: 1, No: 2, Pp: 36-40, 2003
- [92]. Shivakumar. E, G, Gopakumar. K, Sinha, S. K, et al, "Space Vector PWM Control of Dual Inverter Fed Open End Winding Induction Motor Drive" IEEE 16th Annual Applied Power Electronics Conference and Exposition (APEC), Vol: 1, Pp: 399-405, 2001
- [93]. K. K. Mohapatra, K. Gopakumar, V. T. Somasekhar, and L. Umanand, "A Novel Modulation Scheme for a Six Phase Induction Motor with Open End Windings" IEEE 28th Annual Conference on Industrial Electronics Society (IECON), Vol: 1, Pp: 810-815, 2002
- [94]. V. T. Somasekhar, K. Gopakumar, M. R. Baiju, "Dual Two Level Inverter Scheme for and Open End Winding Induction Motor Drive with a Single DC Power Supply and Improved DC Bus Utilization" IEE Proceedings on Electric Power Applications, Vol: 151, Issue: 2, Pp: 230-238, 2004
- [95]. Krushna K. Mohapatra, K. Gopakumar, V. T. Somasekhar, and L. Umanand, "A Harmonic Elimination and Superposition Scheme for Open End Winding Induction Motor Drive" IEEE Trans on Industrial Electronics, Vol: 50, No: 6, Pp: 1187-1198, 2003
- [96]. Jaison Mathew, P. P. Rajeevan, K. Mathew, et al "A Multilevel Inverter Scheme with Dodecagonal Voltage Space Vectors Based on Flying Capacitor Topology for Induction Motor Drives" IEEE Trans on Power Electronics, Vol: 28, No: 1, Pp: 516-525, 2013

- [97]. P. P. Rajeevan, K. Sivakumar, Chintan Patel, et al, "A Seven Level Inverter Topology for Induction Motor Drive Using Two Level Inverters and Floating Capacitor for H-Bridges" IEEE Trans on Power Electronics, Vol: 26, No: 6, Pp: 1733-1740, 2011
- [98]. V. T. Somasekhar, K. Gopakumar, M. R. Baiju, et al, "A Multilevel Inverter System for an Induction Motor with Open End Windings" IEEE Trans on Industrial Electronics, Vol: 52, No: 3, Pp: 824-836, 2005
- [99]. S. Lakshminarayanan, K. Gopakumar, G. Mondal, et al, "Eighteen Sided Polygonal Voltage Space Vector Based PWM Control for and Induction Motor Drive" IET, Electric Power Applications, Vol: 2, Issue: 1, Pp: 56-63, 2008
- [100]. Chintan Patel, Rajeeven P. P, Anubrata Dey, et al, "Fast Direct Torque Control of an Open End Induction Motor Drive Using 12-Sided Polygonal Voltage Space Vectors" IEEE Trans on Power Electronics, Vol: 27, No: 1, Pp: 400-410, 2012
- [101]. Yoshitaka Kawabata, Motoshi Nasu, Tkuya Nomoto, et al, "High Efficiency and Low Acoustic Noise Drive System Using Open Winding AC Motor and Two Space Vector Modulated Inverters" IEEE Trans on Industrial Electronics, Vol: 49, No: 4, Pp: 783-790, 2002
- [102]. Bin Lin, Dan Sun, and Yin Chen, "Research on High Speed Operation of Hybrid Inverter Fed Open Winding Permanent Magnet Synchronous Motor" IEEE International Conference on Electrical Machines and Systems, Pp: 1179-1183, 2013
- [103]. Y. Lee, and J. Ha, "Hybrid Modulation of Dual Inverter for Open End Permanent Magnet Synchronous Motor" IEEE Trans on Power Electronics, vol:30, no:6,Pp: 3286-3299, 2015
- [104]. Mu-Shin Kwak, and Seung-Ki Sul, "Control of an Open Winding Machine in a Grid Connected Distributed Generation System" IEEE Trans on Industry Applications, Vol: 44, No: 4, Pp: 1259-1267, 2008
- [105]. F. Meinguet, Nguyen Ngac-Ky, P. Sandulescu, et al, "Fault Tolerant Operation of an Open Winding Five Phase PMSM Drive with Inverter Faults" IEEE 39th Annual Conference on Industrial Electronics Society, Pp: 5191-5196, 2013
- [106]. N. Nguyen, F. Meinguet, E. Semail et all, "Fault Tolerant Operation of an Open End Winding Five Phase PMSM Drive with Short Circuit Inverter Fault" IEEE Trans on Industrial Electronics, Vol: 63, Issue: 1, Pp: 595-605, 2016.
- [107]. Mu-Shin Kwak, and Seung-Ki Sul, "Flux Weakening Control of an Open Winding Machine with Isolated Dual Inverters" IEEE 42nd Annual Meeting on Industry Applications Conference (IAS), Pp: 251-255, 2007

- [108]. Di pan, Feng Liang, Yang Wang, and Thomas A. Lipo, “Extension of The Operating Region of an IPM Motor Utilizing Series Compensation” IEEE Trans on Industry Applications, Vol: 50, No: 1, Pp: 539-548, 2014
- [109]. Bin Lin, Dan Sun, Yin Chen, “Research on High Speed Operation of Hybrid Inverter Fed Open Winding Permanent Magnet Synchronous Motor” IEEE International Conference on Electrical Machines and Systems (ICEMS), Pp: 1179-1183, 2013
- [110]. R. U. Haque, M. S. Toulabi, A. M. Knight, J. Salmon, “Wide Speed Range Operation of PMSM Using an Open Winding and a Dual Inverter Drive with a Floating Bridge” IEEE Energy Conversion Congress and Exposition (ECCE), Pp: 3784-3791, 2013
- [111]. Joon Sung Park, and Kwanghee Nam, “Dual Inverter Strategy for High Speed Operation of HEV Permanent Magnet Synchronous Motor” IEEE 41st Annual Meeting on Industry Applications (IAS), Pp: 488-494, 2006
- [112]. Y. Wang, T. A. Lipo, D.Pan “Half Controlled Converter fed Open Winding Permanent Magnet Synchronous Generator for Wind Generation” IEEE Conference on Power Electronics and Motion Control (EPE/PEMC), Pp:123-126, 2010
- [113]. A. P. Sandulescu, F. Meinguet, X. Kestelyn, et al, “Flux Weakening Operation of Open Winding Drive Integrating a Cost Effective High Power Charger” IET Electrical Systems in Transportation, Vol: 3, Issue: 1, Pp: 10-21, 2013
- [114]. P. Sandulescu, F. Meinguet, X. Kestelyn, et al “Control Strategies for Open End Winding drives Operating Flux Weakening Region” IEEE Trans on Power Electronics, Vol: 29, Issue: 9, Pp: 4829-4842, 2014
- [115]. B Lin, D Sun, “Analysis on Constant Power Range Enhancement in Hybrid Inverter Open Winding PMSM Drive System” IEEE International Conference on Electrical Machines and Systems (ICEMS), Pp: 2923-2929, 2014
- [116]. M. S. Toulabi, J. Salmon, A. M. Knight “Analysis of a Wide Speed Range Open Winding IPM with Floating Bridge” IEEE International Symposium on Industrial Electronics (ISIE), Pp: 1440-1445, 2015
- [117]. J. Wang, Z. P. Xia, S. A. Long, and D. Howe, “Radial Force Density and Vibration Characteristics of Modular Permanent Magnet Brushless AC Machine” IEE Proceedings – Electric Power Applications, Vol: 153, Issue: 6, Pp: 793-801, 2006
- [118]. Nicola Bianchi, Silverio Bolognani, and Paolo Frare, “Design Criteria for High Efficiency SPM Synchronous Motors” IEEE Trans on Energy Conversion, Vol: 21, No: 2, Pp: 396-404, 2006

- [119]. P. Campbell, "System Cost Analysis for an Interior Permanent Magnet Motor" Ames Laboratory, Iowa State University, United States Department of Energy, 2008
- [120]. D. W. Novotny and T. A. Lipo, Vector Control and Dynamics of AC Drives. Oxford, U.K.: Clarendon, 1998
- [121]. <https://www.semikron.com/>
- [122]. E. Lovelace, T. Jahns, T. K. Jackson Wai, J. Lang, D. D. Wentzloff, F. Leonardi, and J. Miller, "Design and Experimental Verification of A Direct-Drive Interior PM Synchronous Machine Using a Saturable Lumped-Parameter Model," IEEE Industry Applications Society Conference., Vol. 4, Pp. 2486-2492, 2002.
- [123]. F. Magnussen, "On Design and Analysis of Synchronous Permanent Magnet Machines For Field-Weakening Operation In Hybrid Electric Vehicles." PhD Thesis, Royal Institute of Technology, Stockholm, Sweden, 2004.
- [124]. Florence Meier, "Permanent Magnet Synchronous Machine with Non-Overlapping Concentrated Windings for Low Speed Direct Drive Applications" PhD Thesis, Royal Institute of Technology, 2008